Porous graphitic carbon-based metabolomics and development of an alternative biomass-derived carbon stationary phase

Andrew Stewart Marriott

PhD

University of York

Department of Chemistry

September 2013

Abstract

In contrast to standard reversed-phase liquid chromatography (RP-LC) columns, porous graphitic carbon (PGC) stationary phase offers one solution to the separation of polar compounds. The unique retention mechanism of PGC, owing to its planar graphite-like sheet functionality, enables the separation of isomeric compounds. The use of RP-LC solvent systems allows direct coupling with electrospray mass spectrometry (ESI-MS) which enhances the types of analyses that can be performed with this stationary phase type still further.

This thesis describes the use of on-line PGC-LC-ESI-MS^n methods for the analysis of metabolites extracted from leaf blade samples from plant systems subjected to water deficit. The quantitative analysis of targeted carbohydrates in the resurrection plant *Haberlea rhodopensis* along with the untargeted analysis of water soluble metabolites in the model plant species *Arabidopsis thaliana* and *Thellungiella salsuginea* was performed.

In addition, this thesis describes the optimisation of an alternative biomass-derived mesoporous carbon stationary phase, termed Starbon®, utilising the naturally porous material formed by expansion of the algal polysaccharide alginic acid in water.

The effect of pyrolysis rate on the textural properties of Starbon® is investigated and shows that increased rates of pyrolysis reduce the inherent mesoporosity of the final carbon material. Several strategies are investigated in order to improve the particle size and morphology properties of Starbon®. These investigations have led to the development of a novel method of producing alginic acid-derived mesoporous carbon microspheres (AMCS). Commercial PGC, Starbon®, and AMCS-packed columns are compared in the separation of several carbohydrate standards. The column efficiency of the AMCS-packed column compares well to commercial PGC at low mobile phase flow rates. A study of the chemical microstructure of commercial PGC, Starbon®, and AMCS using microscopy and spectroscopy techniques is described. Starbon® and AMCS show abnormally high amounts of fullerene character compared to model non-graphitising carbons.

List of contents Page

List of tables

Chapter 2

Chapter 3

Chapter 4

Chapter 5

Chapter 6

List of figures

Chapter 1

Chapter 2

replicates. Paired t-tests were performed on w/w % values between two time-points at the $p < 0.05$ significance limit. The ★ symbol shows differences which were found to be statistically significant.

Chapter 3

Figure 3.1: A schematic summary of the statistical methods and correctional treatments performed on the LC-MS datasets from *A. thaliana* and *T. salsuginea* in order to determine key discriminating features corresponding to metabolite changes during drought stress

Figure 3.2: Principal components analysis scores plots of a) *A. thaliana* full scan data and b) *T. salsuginea* full scan data. These plots show the separation of late-stress (day 12 and 13, represented by blue (day 12) and yellow (day 13) circles respectively) samples from the rest. QC samples are shown as red circles

Figure 3.3: PCA scores plot for the first two principal components for *T. salsuginea* samples, coded according to batch

Figure 3.4: PCA scores plots for a) *T. salsuginea* and b) *A. thaliana* early-stress samples considering only Group A markers. The coloured diamonds represent: day 0 (red); day 1 (green); day 3 (blue) and day 5 (yellow) samples. Arrows represent the direction of stress state progression

Figure 3.5: Examples of relative intensities for variables in Group A (identified as late-stress markers in the first stage of the analysis) shown for control and early-stress samples (Day 0, red; Day 1, green; Day 3, blue; Day 5, yellow). In (a) the intensity for *m/z* 707.1 at 10.5 minutes for *T. salsuginea* can be seen to increase with increasing stress, whereas in (b) the intensity for *m/z* 405 at 13.5 minutes for *A. thaliana* decreases with increasing stress. The horizontal lines represent the mean of each group

Figure 3.6: PCA scores plots for a) *T. salsuginea* and b) *A. thaliana* of early-stress samples obtained from Group B variables, after denoising. The coloured diamonds represent: day 0 (red); day 1 (green); day 3 (blue) and day 5 (yellow) samples. The arrow represents the direction of stress state progression in *T. salsuginea*

Chapter 4

Figure 4.1: (a) Adsorption pore size distribution and (b) N_2 sorption isotherm plots. The plots are arranged in ascending order of pyrolysis rate, represented by the following colours: 1 K min^{-1} = Black; 2 K min^{-1} = Red; 3 K min^{-1} = Blue; 5 K min^{-1} = Light Green; 6 K min^{-1} = Brown; 7 K min^{-1} = Cyan; 10 K min^{-1} = Dark Green; 20 K min^{-1} = Purple

Figure 4.2: (a) Representative thermal gravimetry (TG-black line) and differential TG (DTG-red line) plots showing effect of pyrolysis at 1 K min^{-1}; (b) DTG plots for all samples with table showing K_{max}, the maximum rate of mass loss per sample

Chapter 5

Chapter 6

Chapter 7

Acknowledgements

First and foremost, I would like to thank my supervisors Jane Thomas-Oates, James Clark, Andy Hunt and Ed Bergström for the giving me the opportunity to pursue a PhD at York. Your ongoing support and guidance has been invaluable to me throughout my PhD. In particular, I would also like to thank Jane for putting up with my awful grammar throughout the TAP report and thesis chapter revisions and Ed for all the help and sound advice over the years. Special thanks also to Julie for all your help with the world of stats, especially during the thesis write-up!

I would like to thank the members of the JETO group, both past and present, who helped me to settle in to postgraduate life and providing me with a great working atmosphere. Thanks to Kriang, Siân, Salina, Jimmy Mack, "Curly" Carl, Karl, Jo, Rachel, Helen and Kirsty. I would similarly like to thank the Green Chemistry group and in particular Cinthia, Gareth, Gronnow, Helen, Jimbo, Mario, Pete H, Pete S, Rob, Tom A, Tom F and Vitaliy for the advice and good banter over the years.

Big thanks to all the people who have provided me with timely distractions when times were tough. Thanks to the Cavs rugby team for two enjoyable seasons, the Team Green football team for putting up with me as captain for four fruitless years, the Casually Inept football posse and Team Toadsworth quiz crew. Special thanks the lunchtime gang for providing me with great memories over the last four years, in particular; Dan R, Danielle, Dave, Linda, Lizzie, Lucy, Natalie, Richard and Tom S. Also thanks to the 3 Robs, Bea, Chiara, Dan S, Karin, Kim, Kirsty H, Lee, Matt and Molly, Will and Kat and all the guys back in Sheffield!

I would like to thank my family, above all; Mum, Dad, Lawrence, Jill, my 'little' brother Michael and Liz, Sam, Neal (and Gabriella!), whose love, support, and continuous encouragement throughout my PhD has helped me to persevere through the challenging times. Anche, grazie mille a la famiglia Ciano per loro gentilezza e accoglienza!

And finally, very special thanks go to "il mio gattino" Luisa for her friendship, love and support over the last three-and-a-half years. Non avrei potuto finito questa tesi senza di te.

Author's Declaration

I hereby declare that the work presented in this thesis is my own, except where otherwise acknowledged, and has not been submitted previously for a degree at this or any other university.

In addition, several articles have been published using research found in Chapters 2, 5 and 6. The full references are given below:

Tsanko S. Gechev, Maria Benina, Toshihiro Obata, Takayuki Tohge, Neerakkal Sujeeth, Ivan Minkov, Jacques Hille, Mohamed-Ramzi Temanni, **Andrew S. Marriott**, Ed Bergström, Jane Thomas-Oates, Carla Antonio, Bernd Mueller-Roeber, Jos H. M. Schippers, Alisdair R. Fernie, Valentina Toneva, "Molecular mechanisms of desiccation tolerance in the resurrection glacial relic *Haberlea rhodopensis*", ***Cellular and Molecular Life Sciences*, 70 (2013) 689-709**

Andrew S. Marriott, Ed Bergström, Andrew J. Hunt, Jane Thomas-Oates, James H. Clark, "A natural template approach to mesoporous carbon spheres for use as green chromatographic stationary phases", ***RSC Advances*, 4 (2014) 222-228**

Andrew S. Marriott, Andrew J. Hunt, Ed Bergström, Karen Wilson, Vitaliy L. Budarin, Jane Thomas-Oates, James H. Clark, Rik Brydson, "Investigating the structure of biomass-derived non-graphitizing mesoporous carbons by electron energy loss spectroscopy in the transmission electron microscope and X-ray photoelectron spectroscopy", ***Carbon*, 67 (2014) 514-524**

Andrew Stewart Marriott

Chapter 1

Introduction

1.1 Carbons

Carbon is a non-metallic, tetravalent element and is one of the most abundant elements on Earth (Yaroshevsky, 2006). There are several allotropes known, with the most common forms being amorphous carbon e.g. coal and soot, graphite and diamond, whilst fullerenes have also come to prominence since the discovery of the C_{60} Buckminsterfullerene in 1985 by Kroto *et al*. (Kroto *et al*., 1985). Amorphous carbon is composed of a mix of sp^2- and sp^3-hybridised carbon, graphite is made up of sp^2-hybridised carbon sheets bound together by weak π-bonding interactions (see Figure 1.1(A)), and diamond is a cubic sp^3-hybridised carbon structure (Figure 1.1(B)); the differing hybridisation state of the carbon in these materials confers different properties on these allotropes (Falcao and Wudl, 2007). Amorphous carbon and graphite are soft, brittle and black materials. On the other hand, diamond is a white, translucent material and the hardest known mineral on the planet (Mohs hardness scale = 10).

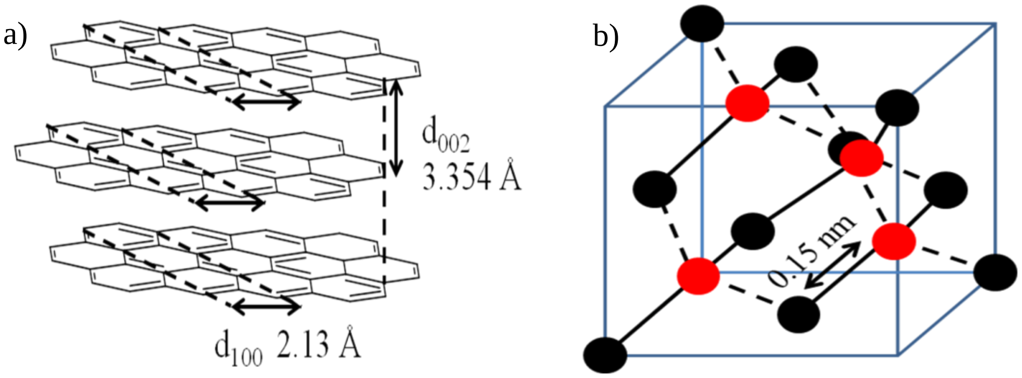

Figure 1.1: Structural representations of a) graphite and b) diamond. Red circles represent the four tetrahedral carbon centres which make up the unit cell of diamond. Straight lines represent bonds which occur “in front of” the position of the each carbon centre and dotted lines represent bonds which occur “behind” the position of the carbon centre.

1.1.1 The main carbon allotropes and their applications

The diverse properties associated with its different allotropes mean that carbon materials are used in an equally diverse range of applications (Figure 1.2).

1.1.1.1 Diamond

Diamond has long been used in jewellery and decoration and as a symbol of wealth and prestige. The properties of diamond include corrosion and wear resistance, high thermal conductivity and optical transparency, which covers a broad range from deep ultraviolet to far infrared (May, 2000). However, due to its rarity and the generally small size of natural diamonds, the scope of applications it could be successfully used in is limited. The development of the high-pressure high-temperature growth technique (employing pressures up to 5.5 GPa and temperatures above 2000 ^{o}C) in the late 1950s (Bovenkerk *et al.*, 1959) led to the production of the first commercial gem-quality synthetic diamonds (known as “industrial diamonds”) by General Electric in the early 1970s (May, 2000). This technique remains the cheapest method to form diamonds which were initially, and continue to be, used as wear-resistant cutting and machining parts.

Figure 1.2: Applications of carbon allotropes include jewellery, pencil lead, energy storage and delivery vehicles for MRI contrast agents.

Further to this, research pioneered by William G. Eversole in the 1950s looked to prepare synthetic diamonds using chemical vapour deposition (CVD) (Eversole, 1962). This technique involves the exposure of a substrate to volatile precursors which react/decompose onto the surface of the substrate, forming the desired deposit product. Eversole’s early work used diamond as the substrate with a “carbon containing gas” such as methane as the precursor (Eversole, 1962). Further developments in the 1980s using hot filament reactors with non-diamond substrates and microwave plasma reactors, helped to significantly speed up diamond synthesis (Matsumoto *et al.*, 1982; Kamo *et al.*, 1983; Saito *et al.*, 1986). Diamonds synthesised by CVD could be prepared in thin films and there was greater control of diamond shape, allowing the development of protective diamond coatings and windows for optics (Costello *et al.*, 1994) and conductive fillers for use in electronics (Lee and Yu, 2005).

1.1.1.2 Graphite

Graphite has long been used as pencil “lead”, due to its ability to mark paper and other objects. Graphite is also a highly conductive material, owing to the extensive aromaticity of the carbon planes, and is used for anode construction in lithium ion batteries (Flandrois and Simon, 1999). Graphite is considered to be anisotropic (i.e. directionally dependent) due to the difference in binding within the layers (strong covalent bonds) and between layers (weaker π-bonding interactions). This difference, which ensures that thermal and electrical conductivity only occurs within the graphitic plane, is the basis of the employment of graphite as a lubricant. The graphite layers move across each other in what is known as incommensurate contact i.e. the mismatching lattice structure prevents the collective stick-slip motion caused by the direct overlap of the atoms, reducing the kinetic friction force (Dienwiebel *et al*. 2004). This is a property known as “superlubricity” (Hirano and Shinjo, 1990). One of the most recent advances in materials science is the discovery of graphene, consisting of a single graphite layer, which displays high conductivity and mechanical strength (Novoselov *et al*, 2004). There is ever growing interest in graphene for use in very many applications, with particular attention being paid to its use in electronics (Geim, 2009).

1.1.1.3 Amorphous carbon

Amorphous carbons, most commonly prepared by the thermal combustion of organic precursors, are a mixture of predominantly sp^2 and sp^3-hybridised carbon with a smaller percentage of heteroatoms which derive from the parent carbonising material. Amorphous carbons can be split into two classes; graphitizing and non-graphitizing carbons depending on whether or not the organic carbon precursor is able to form polycrystalline graphite under high temperatures of pyrolysis (Franklin, 1951; Daniels *et al*., 2007). In general, graphitizing carbons are prepared from aromatic hydrocarbon systems such as pitches and tars, and using processes such as CVD. In contrast, non-graphitizing carbons are prepared from more amorphous carbon precursors, for example polymeric resins and biomass, tending to form more porous carbons (i.e. ordered mesoporous carbons (OMC), carbon blacks, activated carbons and soots) (Harris and Tsang, 1997; Harris, 2005; Zhang *et al*., 2011). Other superstructures that have been discovered/developed from non-graphitizing carbons include fullerenes (Kroto *et al*., 1985; Alekseyev and Dyuzhev, 2003; Harris, 2005) and carbon nanotubes (Iijima, 1991; Ebbeson and Ajayan, 1992; Liu *et al*., 2007; Jha *et al*., 2011).

The properties of fullerenes, hexagonal rings interspersed with pentagons to create bent/spherical structures, include being a strong absorbent in the UV and weaker absorbent in the visible spectral regions respectively, and the ability to be reversibly reduced by up to six electrons (Jensen *et al*., 1996; Prato, 1997). These properties have led to the use of functionalised fullerenes in photovoltaic cells and polymers/thin films which retain the properties of the parent fullerene (Prato, 1997; Zheng, 2003). Binding fullerenes with biological macromolecules e.g. cyclodextrins allows these materials to be solubilised for biomedical applications including as antioxidant and neuroprotective agents, and for DNA photocleavage, while the fullerene cage structure is ideal to act as a delivery vehicle for MRI contrast agents (Jensen *et al*., 1996; Bosi *et al*., 2003; Fatouros *et al*., 2006).

Graphitic carbon nanotubes (CNT) were first reported by Iijima in 1991 (Iijima, 1991) and since then have been used in a number of applications, owing to their electrical and mechanical properties which can be altered by the changing the diameter and number of walls in the CNT structure. CNT have inherently high strength which makes them ideal for use as structural composites (Coleman *et al*., 2006), and high thermal and electrical conductivity (greater than that of a copper wire) which means they can be used in electronics and wiring (Falcao and Wudl, 2007). Although there have been investigations into the use of CNT as adsorbents, porous carbons offer much greater capacities at lower costs.

Porous carbons are open-pore materials with high surface areas and are used in many areas of modern carbon technology. Pore diameter is used to define these materials as either microporous (pore size < 2 nm), mesoporous (2nm < pore size < 50 nm) or macroporous (pore size > 50 nm) (Everett, 1972) or combinations of these three classes (i.e micro/meso or meso/macro). Activated carbons (AC) and carbon molecular sieves are micro/meso porous carbons with broad pore size distributions prepared by pyrolysis or activation of an organic precursor, e.g biomass or polymers

(Liang *et al*., 2008). AC and molecular sieves are the most widely used forms of carbon owing to their relatively low cost. Large quantities of these carbon types are used in adsorption (Gaffney, 1996; Dąbrowski *et al*., 2005), separation (Sircar *et al*., 1996; Freitas and Figueiredo, 2001) and catalysis (Mackenzie *et al*., 2005; Suganuma *et al*., 2011) applications. AC and molecular sieves have several limitations including slow mass transport through narrow pores, low conductivity from surface defects, and collapse of the pore structures at high temperatures (Liang *et al*., 2008). These limitations have led to investigations into other methods of preparation including physical or chemical activation, catalyst-assisted activation with metal oxides or organometallic compounds, and carbonization of aerogels/cryogels (Tamon *et al*., 1999; Kyotani, 2000; Liang *et al*., 2008). However the materials prepared by these methods continue to have broad pore size distributions and significant microporosity (Ryoo *et al*., 2001). OMC are increasingly used for the applications listed due to their preferential mesopore networks, greater inherent strength, and improved conductance due to the low incidence of surface defects. The combination of high mesoporosity and improved conductance has led to interest in using OMC as capacitors (Lee *et al*., 2000; Ryoo *et al*., 2001). OMC have been prepared in numerous ways, but these start from one of two branches, incorporating either hard-templating or soft-templating methods.

Hard-templating methods involve using a pre-synthesised organic/inorganic template into which an organic carbonising resin is impregnated and pyrolysed. The hard-template is then dissolved to leave the mesoporous material, after which further pyrolysis or functionalisation can be performed. This method originated in the late 1980s when Knox and co-workers developed porous graphitic carbon (PGC), synthesised using a phenolic resin impregnated in a porous silica template (Gilbert *et al*., 1982; Knox *et al*., 1986). The development of PGC has since spawned numerous variations based on different silica scaffolds. The first, an OMC derived from the aluminosilicate MCM-48 template, termed CMK-1, was first reported by Ryoo *et al*. in 1999 (Ryoo *et al*., 1999). The use of different scaffolds allows the tuning of the pore shape, pore structure and pore diameter of the corresponding OMC whereby the pore wall thickness of the template affects the final pore size of the carbon product (Zhao *et al*., 1998).

Soft-templating methods employ amphiphilic molecules, i.e. surfactants and block copolymers, in the synthesis of mesoporous carbons. Synthesis by soft-templating has four requirements; precursors having the ability to self-assemble into nanostructures; presence of one pore-forming and one carbon-yielding component; stability of the pore-forming component during curing but decomposition on carbonization with the least carbon yield; and the carbon-yielding component to cross-link and retain nanostructure during the decomposition of the pore-forming component (Liang *et al.*, 2008). The first successful attempt to prepare a mesoporous carbon by the soft-templating route, reported in 2004, used a polystyrene-*block*-poly(4-vinylpyridine) (PS-P4VP)/ resorcinol-formaldehyde system (Liang *et al.*, 2004). However, the limited supply of this polymer led to the discovery of the similarly successful poly (ethylene oxide)-b-poly (propylene oxide)-b-poly (ethylene oxide) (PEO-PPO-PEO) systems (Meng *et al.*, 2006).

Since its development in the 1980s, PGC has been developed for liquid chromatography applications and interest in the use of this stationary phase type, commercialised by Thermo Scientific as Hypercarb™, has grown rapidly owing to its unique separation properties (Gilbert *et al.*, 1982; Knox *et al.*, 1986; West *et al.*, 2010). The work in this thesis is geared towards the development/optimisation of a sustainable biomass-derived mimic of PGC for liquid chromatography applications.

1.2 High performance liquid chromatography

High performance liquid chromatography (HPLC) is a separation technique whereby analytes are separated based on their relative affinities for a liquid carrier flow (the mobile phase - $A_{(\text{mobile phase})}$) which is pumped through a column containing a solid medium (the stationary phase - $A_{(\text{stationary phase})}$). The affinity of a given analyte for either the mobile phase of stationary phase can be represented as an equilibrium (Equation 1.1), from which a partition coefficient (***k***$\boldsymbol{k_D}$) can be defined (Equation 1.2).

$$A_{\text{(mobile phase)}} \rightleftharpoons A_{\text{(stationary phase)}}$$ **Equation 1.1**

$$k_D = [A_{\text{(stationary phase)}}] / [A_{\text{(mobile phase)}}]$$ **Equation 1.2**

In general, a mixture of analytes is injected onto the column, packed with a solid or immobilised stationary phase medium, in a thin, concentrated band. The analytes are carried through the column by a flow of mobile phase whilst interacting with the stationary phase and, dependent on their k_D value, are separated from each other. A high k_D value indicates that the analyte is strongly retained by the stationary phase and thus elutes later from the column than an analyte with a low k_D value. The time it takes for the mobile phase to pass through the column is known as the ‘void time’ ($\boldsymbol{t_M}$) and the time it takes for an analyte to elute is known as the ‘retention time’ ($\boldsymbol{t_R}$) of that analyte. From these values, the migration rate of an analyte through a column can be determined, which is expressed in terms of the retention factor or capacity factor ($\boldsymbol{k'}$) (Equation 1.3)

$$k' = (t_R - t_M) / t_M \qquad \textbf{Equation 1.3}$$

The ratio of the capacity factors of two different analytes (A and B) can be used to determine the selectivity factor ($\boldsymbol{\alpha}$) between the two eluting peaks (Equation 1.4).

$$\alpha = k' (\mathrm{B}) / k' (\mathrm{A}) \qquad \textbf{Equation 1.4}$$

This parameter only determines the selectivity factor from the centre of an eluting peak and does not take into account how broad a peak is. Peak broadening affects the efficiency of separation and therefore needs to be taken into account.

Plate theory is commonly used to determine column efficiency and is based on the concept of a plate, defined as a point of interaction between an analyte and the stationary phase. The greater the number of plates ($\boldsymbol{N}$) in a column, the more efficient the separation provided by that column. When the retention time and full peak width at half maximum height ($\boldsymbol{w_{1/2}}$) is known, N can be calculated using equation 1.5:

$$N = 8 \ln(2) \,.\, (t_R/w_{1/2})^2 \qquad \textbf{Equation 1.5}$$

Peak efficiency can be measured by determining the plate height (***H***), defined as the distance between two plates within a column. The smaller the plate height value, the greater the number of plates (points of interaction) there are in the column, and therefore the more efficient the separation that is realised. By knowing the column length (**L**), plate height can be calculated using Equation 1.6:

$$H = \mathrm{L} / N$$ **Equation 1.6**

Plate height is affected by the linear velocity ($\boldsymbol{\mu}$) of the mobile phase and in 1956 J. J. van Deemter *et al*. described an equation taking into account three constants, A, B and C, which impact plate height (Equation 1.7 - van Deemter *et al*., 1956).

$$H = \mathrm{A} + \mathrm{B}/\mu + \mathrm{C}\mu$$ **Equation 1.7**

Where '**A**' relates to eddy diffusion, '**B**' describes longitudinal diffusion and '**C**' relates to mass transfer:

Eddy diffusion (A) – affected by the size and shape of stationary phase particles packed into the column, eddy diffusion refers to the differing paths of the same analyte molecules flowing through a column. Variations in these path lengths mean some molecules can take longer to pass through the column than others, leading to band broadening. This effect is independent of mobile phase velocity and can be minimised by reducing particle size, which improves packing efficiency, whilst reducing the interstital spaces between particles.

Longitudinal diffusion (B) – injection of a sample mixture onto a column ideally involves applying the analytes in a thin, concentrated band. Over time, the natural process of diffusion (occurring from an area of high concentration to an area of low concentration until equilibrium is established) takes place during the passage of the analyte band through the column, thus leading to band broadening. Longitudinal diffusion is dependent on mobile phase velocity, whereby a faster flow flushes the analyte band through in a shorter time, minimising this effect.

Liquid-solid mass transfer (C) – there are two types of liquid-solid mass transfer which affect column efficiency, trans-particle mass transfer and surface diffusion (Gritti and Guiochon, 2012). Trans-particle mass transfer refers to the diffusion of an analyte through the mesoporous network of a stationary phase particle. Band broadening is affected by the time required for an analyte to diffuse through the particle, therefore column efficiency can be improved by decreasing particle size, or by using solid core silica beads. Surface diffusion refers to the interaction between the analyte with the stationary phase functional groups and the time required for an equilibrium to be established between the stationary phase and mobile phase. In this case column efficiency is dependent on mobile phase flow rate, where the equilibrium required for an analyte to be adsorbed back into the bulk flow takes longer to be established at higher flow rates, increasing band broadening. Therefore in order to reduce band broadening by this effect, slower flow rates need to be used.

Plotting plate height against mobile phase velocity for each of the three constants, a cumulative plot, referred to as the ‘van Deemter curve’, can be generated; the minimum of this curve provides the flow rate which gives the lowest plate height and therefore the optimum peak efficiency (Figure 1.3).

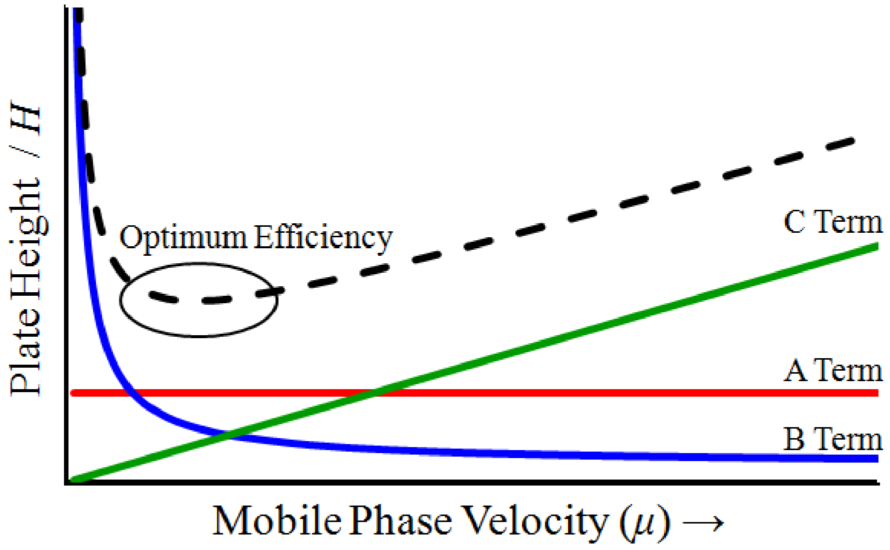

Figure 1.3: Plot of plate height *H* against mobile phase velocity for the A(red), B (blue), and C (green) terms of the van Deemter equation, and cumulative van Deemter curve (dashed line).

By increasing peak efficiency, the separation of different analyte molecules from one another is improved, as with narrow peak widths even a limited separation in terms of retention time may be enough to allow baseline resolution of the two analytes. Resolution can be calculated when both the retention time and baseline widths (w) of the two separated analyte peaks are known, (Equation 1.8):

$$R_s = 2[(t_R)B - (t_R)A] / wA + wB \qquad \textbf{Equation 1.8}$$

A resolution of 1.5 or greater gives baseline separation of analytes.

The retention mechanism of reversed-phase liquid chromatography (RP-LC), the most commonly used separation mode, is based on the hydrophobicity of an analyte, and uses a non-polar stationary phase and a polar mobile phase system. The greater the hydrophobic character of a compound, the greater its retention on an RP-LC system.

RP-LC stationary phase particles generally consist of silica particles to which hydrophobic alkyl chains are covalently linked. These can carry various functionalities which introduce different selectivities allowing the separation of a wide range of hydrophobic compounds. Octadecylsilyl (C_{18})-bonded silicas are the most common reversed phase stationary phase.

RP-LC systems use a polar mobile phase which is often a mix of water with either methanol or acetonitrile. In many cases however, buffers and modifiers are required to enhance the separation of a group of compounds, by either reducing the variation in the level of analyte ionisation which can affect retention properties, or by increasing the eluotropic strength of the mobile phase to ensure that even strongly retained species are eluted from the column. Examples of buffers include ammonium acetate, sodium dihydrogen orthophosphate and ammonium formate, whilst examples of modifiers include formic acid, trifluoroacetic acid and acetic acid. One key advantage of RP-LC mobile phase systems is that they are generally compatible for use with a mass spectrometer, allowing online coupling which can further the amount of information gathered for a dataset whilst aiding the analysis of unknown analytes in a sample mixture.

1.3 Mass spectrometry

Mass spectrometry (MS) is a powerful tool which can deliver fast, sensitive results at low limits of detection in order to analyse a diverse range of compound classes, from small metabolite compounds to large polymers and biomolecules. MS enables the identification of unknown compounds, quantitation of known compounds, and structure elucidation of both organic and inorganic compounds. The basic premise of mass spectrometry initially sees analyte molecules converted to gas phase ions in the ionisation source. The ions generated in the source pass into a mass analyser where they are separated based on their mass-to-charge ratio (*m/z*) and subsequently guided to a detector. A computer, which is also used to control the mass spectrometer, converts the detector signal into a mass spectrum as well as enabling further data processing (Figure 1.4).

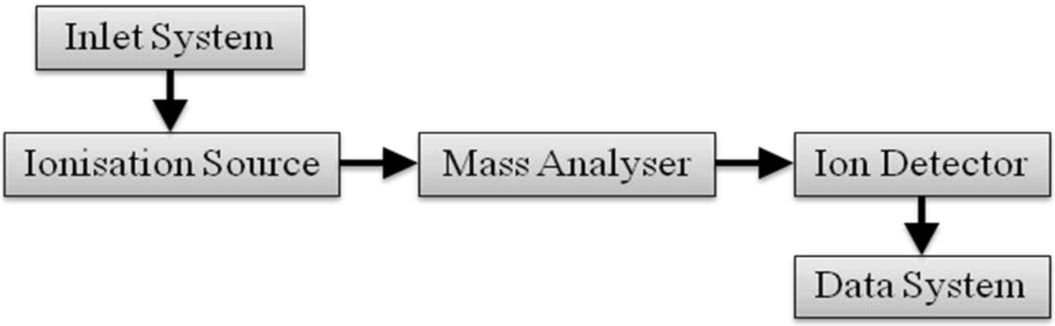

Figure 1.4: Basic components of a mass spectrometer

The following sections describe the main ionisation source and mass analysers used in the work described in this thesis.

1.3.1 Ionisation source - electrospray ionisation

The development of electrospray ionisation (ESI) was initiated by Malcolm Dole (Dole *et al.*, 1968) who used this technique in order to generate intact gaseous polystyrene macroions. Other ionisation sources at that time were not very efficient and could cause fragmentation of fragile species. ESI, termed a 'soft ionisation' technique, produces ions of low internal energy which keeps analyte fragmentation to a minimum. However, it was not until the pioneering work of Fenn and coworkers in the 1980s that ESI became popular as an ionisation source. His studies reported the analysis by ESI of a wide range of analytes, from early works regarding solvent clusters to small alkanes and alkyl ammonium halides to biomolecules. The latter analyte type had previously been difficult to analyse using alternative ionisation methods due to their size, thermally lability, involatility and fragility to fragmentation (Yamashita and Fenn, 1984; Fenn *et al*., 1989; Fenn, 1993).

ESI involves the pumping of an analyte solution (either through direct infusion from a syringe pump, or from an HPLC) through a capillary (Figure 1.5). The capillary tip is highly charged by application of a voltage to produce positive or negative analyte ions depending on the required mode. A spray, generated by a nebulising gas applied coaxial to the sample capillary, is released as an aerosol of droplets from the Taylor cone formed at the capillary tip (the tip must be set at a particular minimum voltage to create the cone (Figure 1.6)) into an ionisation chamber where a drying gas streams over the aerosol, acting as a drying agent; to aid droplet desolvation which ultimately produces gas phase ions. These ions are then attracted to a cone or plate, which has the opposite potential to the capillary to prevent charge imbalance, effectively completing an electrolytic circuit within the chamber. The analyte ions then enter a nitrogen counter flow gas chamber which removes remaining solvent vapour from the ion stream. The ions are then accelerated by skimmers of increasing potential into the mass analyser.

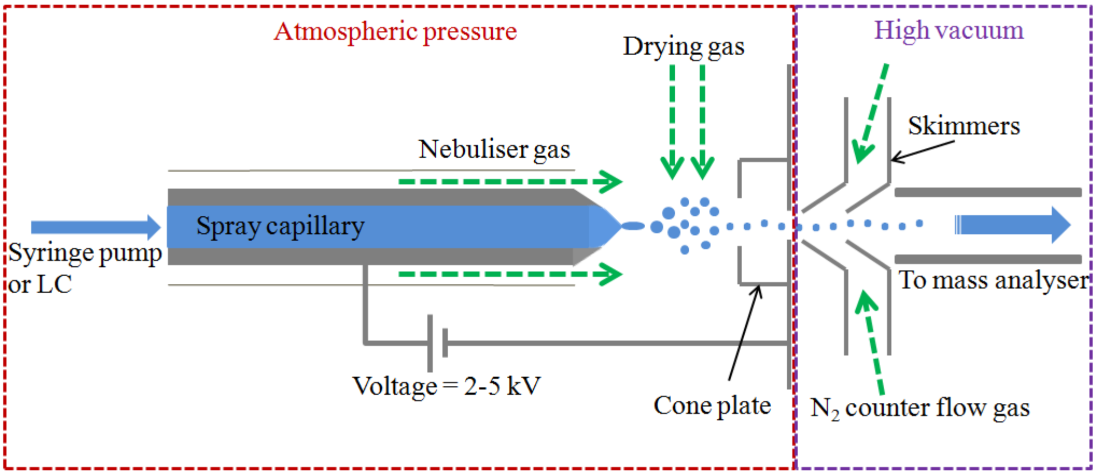

Figure 1.5: ESI source schematic

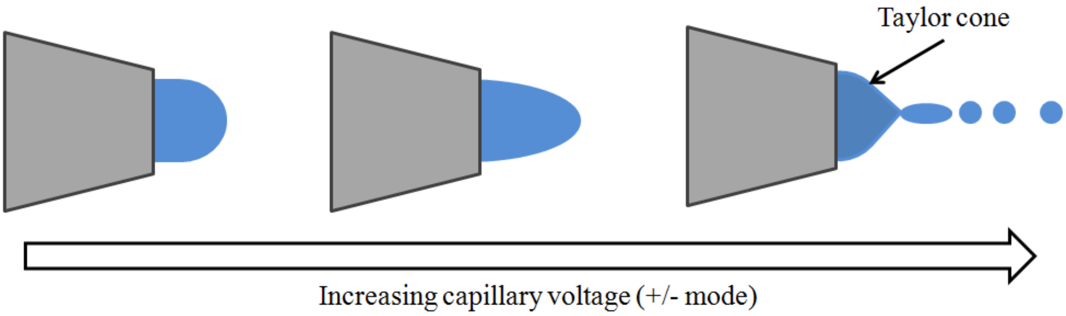

Figure 1.6: The production of a Taylor cone

There are two main theories as to how gas phase ions are generated from solvent droplets in the ionisation chamber, the charged residue model (CRM) and the ion evaporation model (IEM).

The CRM model, proposed by Dole and coworkers (Dole *et al.*, 1968), describes the charged droplets being evaporated in the drying gas whilst the ion charges within the droplet remain the same. At a critical point (known as the 'Rayleigh limit'), where the cohesive force of the droplet's surface tension matches the coulombic force of ion repulsion, fission of the droplet occurs breaking it into smaller droplets. This process continues until the solvent has completely evaporated and the analyte ions remain unsolvated in the gas phase (Figure 1.7).

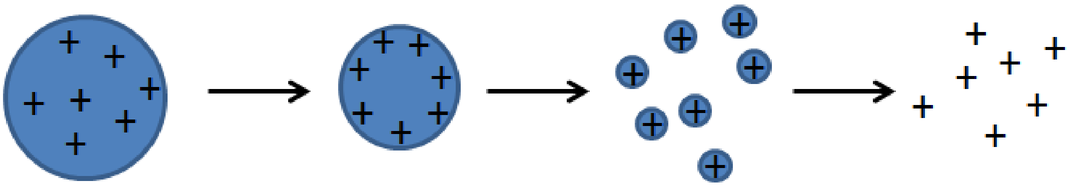

Figure 1.7: Charged residue model

The IEM model was proposed by Iribarne and Thomson and follows the CRM mechanism until the point of the critical limit. Here the electric field strength at the surface of the droplet has risen to a limit where a solvated ion is 'assisted' from the droplet and transferred into the gas phase (Iribarne and Thomson, 1976). The surface field strength is significantly reduced and the process is repeated when further solvent evaporation returns the situation at the surface of the droplet to the Rayleigh limit (Figure 1.8).

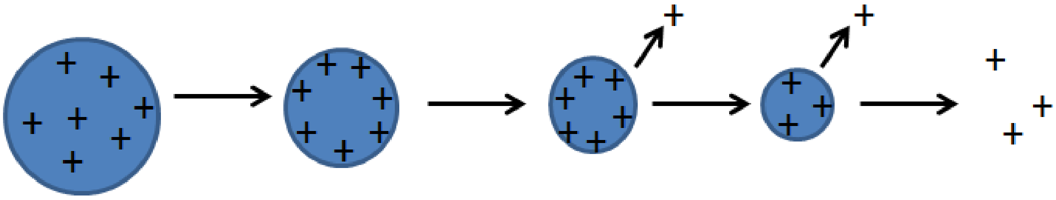

Figure 1.8: Ion evaporation model

Both mechanisms generate either protonated $[M+H]^+$ or deprotonated $[M-H]^-$ molecules, depending on whether the voltage applied to the capillary is positive or negative respectively. In addition however, the generation of molecular species in ESI can arise from cationic (e.g. Na^+, K^+, NH_4^+) or anionic (e.g. Cl^-, CH_3COO^-) components present in the sample, or in the solvent or buffers/modifiers from an HPLC mobile phase system.

1.3.2 Mass analysers

The mass analyser is used to separate the ions generated in the ionisation source based on their mass-to-charge ratio (*m/z*). In this thesis, mass separation was achieved using quadrupole mass analysers, ion trap mass analysers and time-of-flight (TOF) mass analysers. The resolution and mass accuracy of a mass spectrometer are key attributes which need to be considered when analysing complex samples (e.g. plant metabolites - Breitling *et al*., 2006).

Resolution (***R***) is the ability of a mass analyser to differentiate signals for two ions with a small difference in *m/z* value. Resolution is related to the mass (***m***) and peak width ($\boldsymbol{w_{1/2}}$ - designated as full width half maximum (FWHM)) by Equation 1.9

$$R = m / w_{1/2}$$ **Equation 1.9**

Mass accuracy is the difference between the calculated *m/z* value ($\boldsymbol{m_{calc.}}$) and measured *m/z* value ($\boldsymbol{m_{meas.}}$) of an ion relative to the calculated value (Balogh, 2004). Mass accuracy is commonly expressed as a relative error in parts per million (ppm - Equation 1.10):

$$\text{error (ppm)} = (m_{meas.} - m_{calc.}) / m_{calc.} \times 10^6$$ **Equation 1.10**

1.3.2.1 Quadrupole mass analyser

First described by Paul and Steinwedel in 1953 (Paul and Steinwedel, 1953), the quadrupole mass analyser has become a widely adopted mass analyser, due to its small size and relatively low cost compared to other mass analysers, such as those used in magnetic sector instruments. In addition, quadrupoles have a wide range of uses both as stand alone mass analysers, as components of a triple-stage quadrupole mass analyser (QQQ), or coupled to other mass analyser types, for example a time-of-flight mass analyser (Q-TOF). Quadrupoles (as well as hexapoles and octapoles) can work at atmospheric conditions as well as under high vacuum and so are also commonly used as ion guides and collision cells.

Quadrupole mass analysers consist of four circular or hyperbolic electrically conducting rods, separated parallel and equidistant to each other along the instrument's z-axis. Opposite rod pairs are connected by the same electrostatic potential comprising a fixed direct current (dc) and an alternating radio frequency (rf) potential. One rod pair has a potential of +(*U*-*V*cosωt) and the other pair a potential of -(*U*-*V*cosωt), where *U* is the applied fixed dc voltage and *V*cosωt is the applied rf voltage of amplitude '*V*' and frequency 'ω' (Figure 1.9).

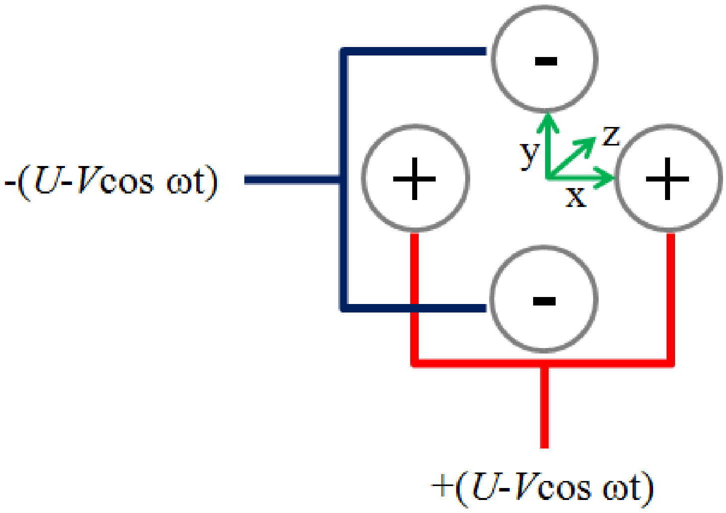

Figure 1.9: Schematic diagram of the opposite pair connections of a linear quadrupole mass analyser

As ions pass along the z-axis of the quadrupole, the applied voltages generate a two dimensional (x-y) quadrupolar electric field; the force induced by this electric field affects the trajectory of the ions. The alternating rf potential causes the ions to oscillate between the rods; however, for given voltages of *U* and *V*, only ions of a particular *m/z* ratio have stable trajectories and therefore are focussed through the quadrupole. Ions of all other *m/z* vlaues are destabilised by the electric field forces, increasing the oscillation amplitude in the x- or y-direction such that the ions hit the rods and are lost. This selectivity method for linear quadrupoles is called 'mass-selective stability mode'.

The stable trajectory for an ion of particular *m/z* through a quadrupolar electric field can be described mathematically by the Mathieu equations, first described in 1868 as solutions regarding regions of stability and instability in vibrating stretched skins (Equations 1.11 and 1.12)(March, 2000).

$$a_u = 8zeU / m\omega^2 r_o^2$$ **Equation 1.11**

$$q_u = 4zeV / m\omega^2 r_o^2$$ **Equation 1.12**

where $\boldsymbol{z}$ is the charge on the ion, $\boldsymbol{e}$ is the charge on an electron, $\boldsymbol{m}$ is the mass of the ion, $\boldsymbol{\omega}$ is the angular frequency, $\mathbf{r_o}$ is the radius of the quadrupolar field, $\boldsymbol{U}$ is the fixed dc voltage and $\boldsymbol{V}$ is the amplitude of the rf voltage.

The solutions to these equations, given the dimensionless nomenclature $\mathbf{a_u}$ and $\mathbf{q_u}$ and plotted for all values of *U* and *V*, produce a stability diagram which defines the operating potential values that ensure the stable trajectory of an ion of given *m/z* through the quadrupolar electric field (Figure 1.10a). In the overlapping region (circled green) the ion has a stable trajectory in both x- and y- directions simultaneously. Although other areas of overlap are visible, the region circled is generally used in MS due to the low potentials required.

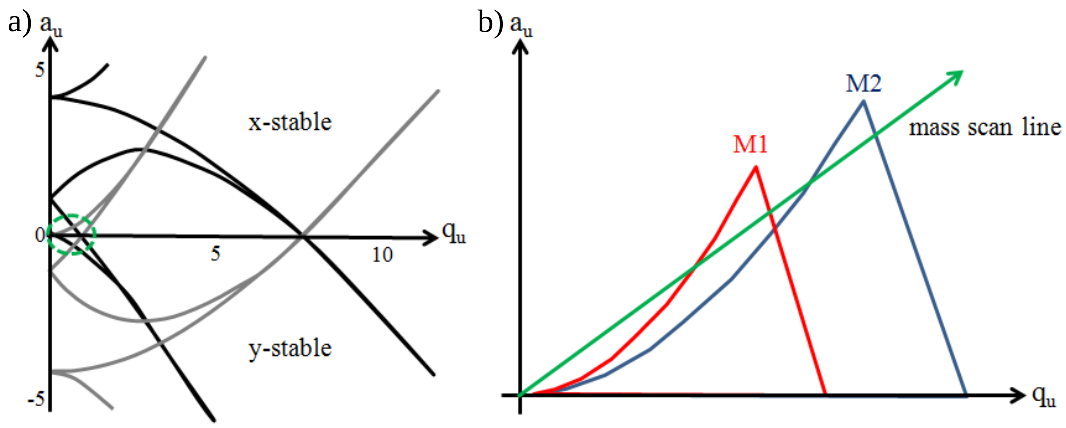

Figure 1.10: a) Linear quadrupole mass analyser stability diagram, in dimensionless a_u-q_u space, where overlap signifies the regions of stable ion trajectories for an ion of particular *m/z* in the x- and y- dimensions; b) Stability regions for two ions with differing *m/z* (M1 and M2); by scanning along the mass scan line whilst maintaining the *U*/*V* ratio, the ions of different *m/z* can be focussed through the quadrupole

By changing the applied voltages *U* and *V*, the selective focussing of ions of differing *m/z* values can be achieved. The simultaneous ramping of *U* and *V*, whilst ensuring the *U*/*V* ratio remains constant, generates a mass scan line along which ions of differing *m/z* are sequentially brought into the stability region and focussed through the quadrupole mass analyser (Figure 1.10b). By raising the slope of the mass scan line, so it passes closer to the apex of the ion stability regions, the resolution of the quadrupole is increased.

1.3.2.2 Ion trap mass analyser

The quadrupole ion trap was developed in parallel with the linear quadrupole by Paul and co-workers in the 1950s. The ion trap is comprised of three electrodes: a ring electrode and two end-cap electrodes which form a hyperboloidal structure (Figure 1.11).

The early mode of operation was the mass-selective stability mode where a dc trapping voltage (*U*) is applied to the end cap and ring electrodes whilst an additonal rf trapping voltage (*V*, known as the “fundamental rf”) is applied to the ring electrode. In this mode, both dc and rf voltages are applied to complement each other, allowing the storage of ions of a single *m/z* value (Jonscher and Yates, 1997). By applying a voltage pulse across the end cap electrodes, the ions are ejected and exit the trap through the opposite end cap electrode to which they entered the trap, to an electron multiplier.

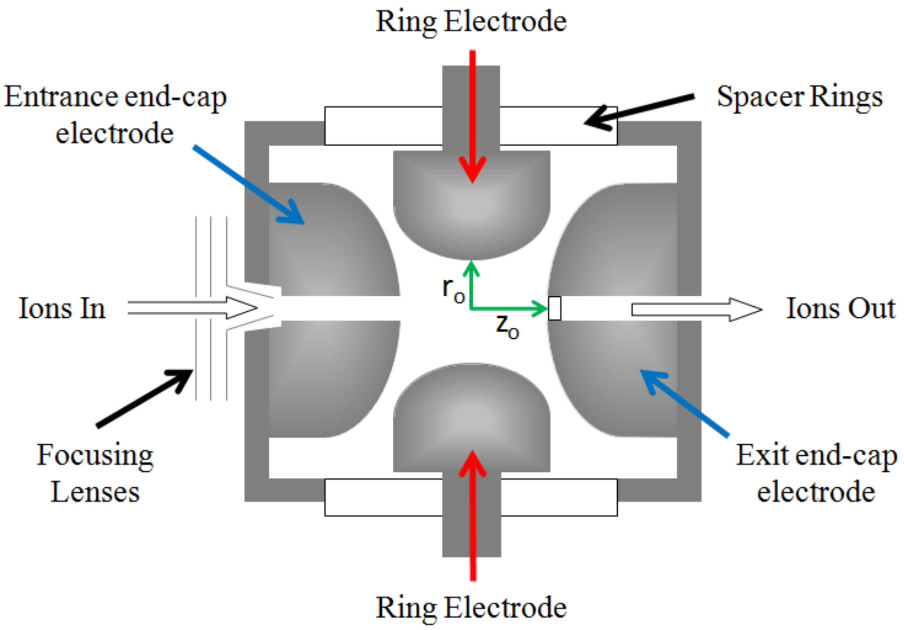

Figure 1.11: Schematic of an ion trap mass analyser

In 1983, George Stafford and co-workers at Finnigan MAT developed the mass-selective instability mode of operation which allowed the trapping of ions with a range of *m/z* values instead of a single value (Stafford *et al*., 1984). As well as this, they discovered that helium gas fed into the trap at a pressure of 1 mtorr improved the resolution of the system by concentrating the ions into a packet at the centre of the trap and reducing their overall kinetic energy through collisional cooling.

In this mode, a dc trapping voltage at the ring electrode is not used and the end cap electrodes are grounded, relying solely on the rf potential to trap the ions. The fundamental rf oscillates in a sinusoidal manner which focuses the ions both axially and radially. Where focussing in the radial direction occurs, the ion becomes defocussed in the axial plane, and vice versa. When the oscillation frequency of the rf is high enough, the two counter motions are balanced, “trapping” the ions and restricting their motion to a plane at the center of the trap.

The trajectory and stability of ions within the trap are determined by the equations which describe the Mathieu working points (co-ordinates on the stability diagram) of an ion in relation to the end-cap electrode (**a_z** - Equation 1.13) and the ring electrode (**q_z** - Equation 1.14)(March *et al.*, 1992).

$$a_z = -16eU / m(r_o^2 + 2z_o^2)\omega^2 \qquad \textbf{Equation 1.13}$$

$$q_z = 8eV / m(r_o^2 + 2z_o^2)\omega^2 \qquad \textbf{Equation 1.14}$$

where ***e*** = electronic charge, ***U*** = d.c. potential, ***V*** = amplitude of the rf potential, ***m*** = mass of the ion, **r_o** = radius of the ring electrode, **$2z_o$** = separation of the endcap electrodes along the ion trap axis and ***ω*** = radial frequency of the rf potential (March, 1997). Since, in the mass-selective instability mode, a dc potential is not applied at the end cap electrodes $U = 0$, therefore $a_z = 0$. The stability of an ion of given *m/z* value at a particular rf potential can thus be calculated by simply solving for q_z (Figure 1.12).

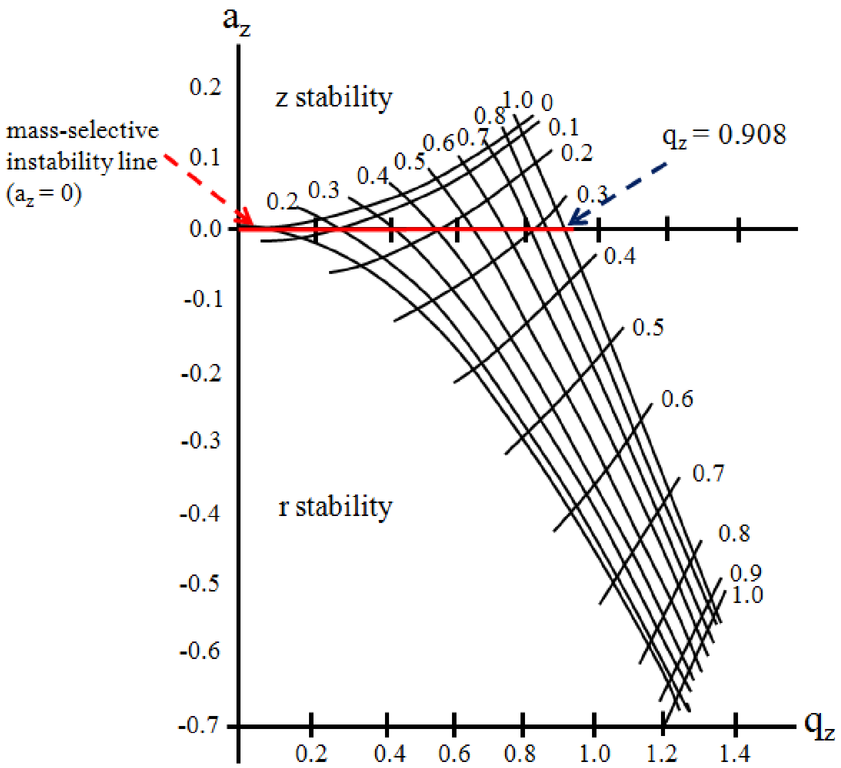

Figure 1.12: Stability diagram in (a_z, q_z) for the regions of stability in both the axial (z) and radial (r) directions near the ion trap centre. The mass-selective instability line at $a_z = 0$ indicates operational area of an ion trap in rf-only mode. Ion trajectory instability occurs where $q_z = 0.908$

By increasing the amplitude of the fundamental rf potential the ion oscillates at higher amplitude in the axial direction. As the amplitude reaches the critical limit (where $q_z = 0.908$), the ion's motion exceeds the trap dimensions and it is ejected from the ion trap to the detector at one end of the ion trap (Figure 1.13, top and middle) (Jonscher and Yates, 1997).

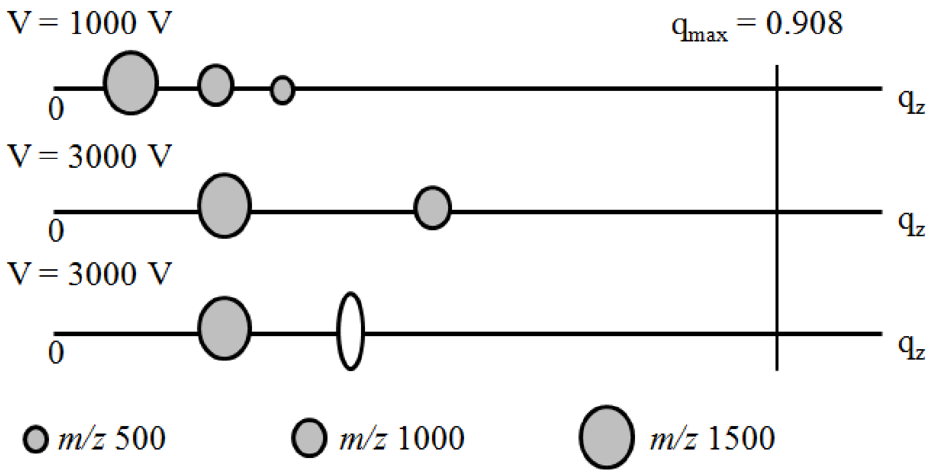

Figure 1.13: Relative positions of three *m/z* ions; top) rf at 1000 V, middle) rf increased to 3000 V, bottom) rf at 3000 V with a resonance point (white elipse) to increase the effective mass range of the mass spectrometer

The greater the *m/z* of the ion, the larger the rf potential required to eject the ion from the trap. There is a maximum to the rf potential that can be applied which is dependent on the power of the particular trap, therefore there is a limit to the range of *m/z* ions that can be ejected and so detected. By creating regions of instability in the axial direction through the application of resonance voltages across the end-cap electrode, known as resonance points or "tickle voltages", these larger ions can be ejected at lower voltages than would otherwise be required (Figure 1.13 bottom).

It is with these resonance points that, when used in parallel with combined reverse and forward scanning, isolation of particular *m/z* ions can occur, leading to the possibility of tandem mass spectrometry (MS/MS) and MS^n analysis. MS/MS and MS^n are performed by sweeping in reverse from high rf amplitudes to remove high mass ions at the resonance point, followed by a forward scan at low rf amplitudes to remove low mass ions; the ions which remain in the trap are then able to undergo fragmentation and their fragments can undergo further isolation and fragmentation to yield structural information.

1.3.2.3 Time-of-flight mass analyser

The concept of time-of-flight (TOF) mass analysers, described by Stephens in 1946, was not realised commercially until the development of the linear TOF by Wiley and McLaren in the mid 1950s (Stephens, 1946; Wiley and McLaren, 1955). In linear TOF mass analysers, ions generated in the source are accelerated by an electric field (V) into a field-free region or flight tube (Figure 1.14)

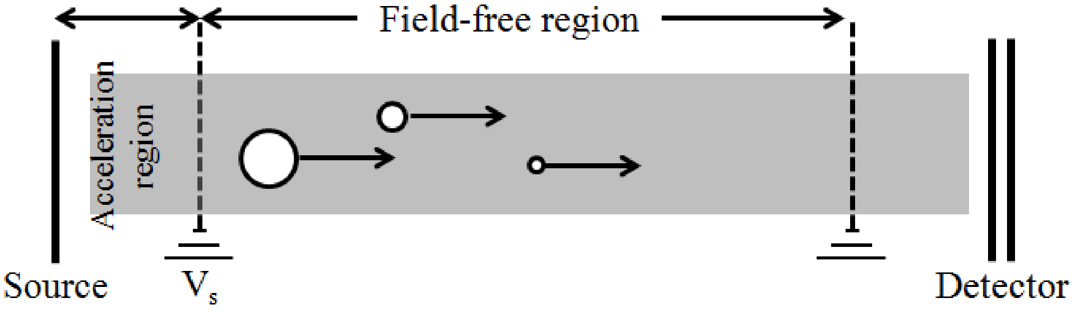

Figure 1.14: Schematic of a linear time-of-flight (TOF) mass analyser

Ions are separated based on their relative velocities (**υ**) in the field-free region which are proportional to their *m/z* ratios; higher mass ions take longer to reach the detector than lower mass ions with the same charge. The kinetic energy (***E**_k*) of an accelerated ion depends on its mass (***m***) and charge (***z***) and the potential difference applied at the source (**V_s**) (Equation 1.15)

$$E_k = zeV_s = 1/2\, m\upsilon^2 \qquad \textbf{Equation 1.15}$$

where ***e*** is the charge of an electron. The time (***t***) required to pass through the length of the field-free region (***L***) is given by Equation 1.16.

$$t = L / \upsilon \qquad \textbf{Equation 1.16}$$

Rearrangement of Equation 1.15 to make υ the subject yields Equation 1.17.

$$\upsilon = (2zeV_s/m)^{1/2} \qquad \textbf{Equation 1.17}$$

Substitution of Equation 1.17 into Equation 1.16, and rearrangement gives the time required for an ion of particular *m/z* to pass through the field-free region (Equation 1.18).

$$t^2 = L^2m / 2ze\mathrm{V}_s$$ **Equation 1.18**

A major drawback with linear TOF mass analysers is poor mass resolution caused by slight differences in flight times for ions of the same *m/z* ratio. Such differences can arise due to differences in time of ion formation, distance of the generated ion from the accelerator, direction of travel of the species at the time of ionisation and small kinetic energy differences of ions of the same *m/z*. One approach that helps overcome the issue of kinetic energy spread is the development and incorporation of a reflectron into the TOF mass analyser.

The reflectron, proposed by Mamyrin and coworkers in the 1970s, is a series of equally spaced ring electrodes which create an energy retarding field to deflect ions back through the flight tube (Mamyrin *et al*., 1973 - Figure 1.15). When ions of the same *m/z* ratio but differing kinetic energies exit the source, those ions with higher kinetic energy penetrate deeper into the reflectron's electric field (**E**) than those with lower kinetic energy. E is related to the potential on the reflectron ($\mathbf{V_r}$) and the length of the reflectron (**D**) by Equation 1.19.

$$\mathrm{E} = \mathrm{V_r} / \mathrm{D}$$ **Equation 1.19**

Ions with higher kinetic energy therefore spend longer in the reflectron before subsequently being reflected back into the flight tube with the same kinetic energy as they entered. Ultimately, as long as the reflectron Vs are chosen appropriately, all ions of the same *m/z* ratio regardless of their kinetic energy will reach the detector at the same time, so increasing the mass resolution of the TOF.

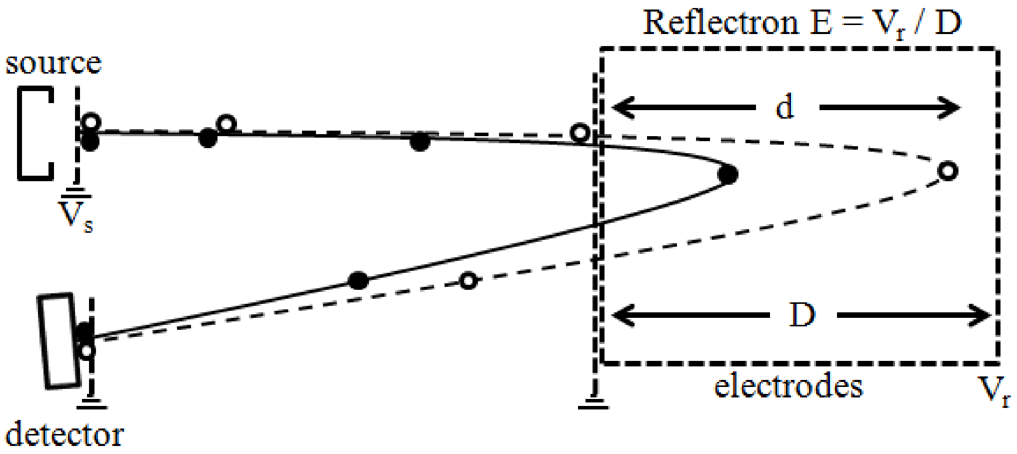

Figure 1.15: Schematic of a TOF mass analyser with reflectron where ○ represents an ion with high kinetic energy and ● represents an ion with low kinetic energy.

1.3.2.4 Orthogonal acceleration

Developed by Guilhaus and coworkers in order to couple TOFs with continuous ion beam sources, such as ESI, orthogonal acceleration TOF (oaTOF) differed from other coupling attempts by positioning the flight tube orthogonal to the continuous ion beam generated in the ion source (Coles and Guilhaus, 1993; Guilhaus *et al.*, 2000). A short electrostatic pulse (10-100 ns), generated at a 'pusher', imparts a force on the passing ion beam, accelerating a packet of ions on this orthogonal trajectory into the field-free region of the TOF.

The Bruker maXis hybrid quadrupole oaTOF system was used in the work reported in this thesis – it is fitted with an ESI ionisation source. A simple schematic of the maXis is shown in Figure 1.16. Ions are funnelled into a hexapole ion guide (Q_0) which focuses the ions into a quadrupole mass filter (Q_1). Depending on the mode of operation required, Q_1 can act as an ion guide to focus ions into the collision cell (Q_2) or can be used to select particular *m/z* ratios for fragmentation. After passing through the collision cell, the ion beam is 'chopped' at the pusher and the ‘slice’ of ions is accelerated into the flight tube. The flight tube of the Bruker maXis system, which includes a reflectron, is 5 m long enabling high mass resolution. Ions are separated based on their *m/z* ratios before reaching the detector.

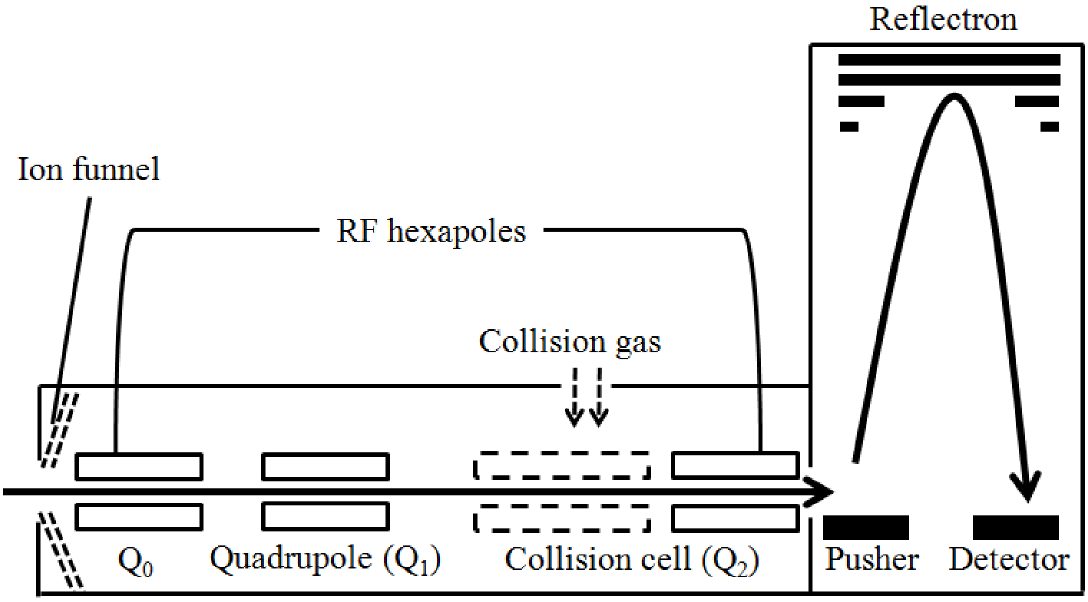

Figure 1.16: Simple schematic of a hybrid quadrupole oaTOF mass analyser

1.4 Porous graphitic carbon chromatography

Since its development in the late 1980s, porous graphitic carbon (PGC) has been used as a separations medium in HPLC. The use of PGC in chromatography has grown over the last 20 years, owing to its ability to retain and separate polar analytes using classical RP-LC mobile phase systems (West *et al*., 2010). PGC overcomes the disadvantages of the traditional approaches to polar analyte separation of normal phase liquid chromatography (NP-LC) and high performance anion exchange chromatography (HPAEC). NP-LC uses low boiling point solvents in the mobile phase (e.g. hexane) which, along with having poor ionisation capabilities in a hyphenated mass spectrometer, can result in retention time variation from evaporation and/or bubble formation, limiting the robustness of this technique (Hemström and Irgum, 2006). For HPAEC, the high salt-based mobile phase media required for separation makes this technique incompatible with on-line mass spectrometric detection.

1.4.1 Development of porous graphitic carbon

In the 1970s, carbon-based packing materials were seen as alternatives to the traditional silica-based materials. The instability of silica-bound functional groups, combined with the difficulty of capping residual silanol groups on the silica particle, limited the useable pH range. This, in turn, restricted the chromatographic mobile phase systems which could be employed (West *et al*., 2010). Carbon-clad silica particles, developed by Colin and Guiochon (Colin and Guiochon, 1976; Colin and Guiochon, 1977)), as well as graphitized thermal carbon black (GTCB), investigated by Ciccioli and coworkers (Ciccioli *et al*., 1981), were early notable efforts. However, carbon-clad silica delivered poor column efficiency and broad chromatographic peaks, whilst GTCB was considered too fragile for HPLC applications (although chromatographic performance was good). Developed by Knox and coworkers (Knox and Gilbert, 1979; Gilbert *et al*., 1982) in the late 1970s, porous glassy carbon was an alternative carbon-based packing material which offered decent chromatographic performance (albeit requiring an additive (*m*-terphenyl) to be introduced into the mobile phase to ensure peak symmetry (Gilbert *et al*., 1982)). However, porous glassy carbon was mechanically fragile so further optimisation of the synthetic route (which in addition aimed to remove additive dependence for peak symmetry and prevent strong retention of analytes) by Knox and coworkers led to the introduction of PGC (Knox *et al*., 1986). PGC was eventually commercialised by Thermo Electron Corporation in 1988 under the tradename Hypercarb™ (West *et al*., 2010).

1.4.2 Synthesis of porous graphitic carbon

The synthesis of Hypercarb™ material requires the use of a silica template filled with a phenol/hexamine carbonising mixture which is subsequently heated to 150 ^{o}C to promote polymerisation. A “carbon black” intermediate is produced under inert atmosphere pyrolysis at 900 ^{o}C. The silica template is then removed using a hot aqueous potash solution and the structure is graphitised by thermal treatment at 2500 ^{o}C under an argon atmosphere to close micropores and remove residual surface functional groups (Knox *et al*., 1986).

Later, an additional final step was added, whereby the temperature is lowered to 1000 ^{o}C, and argon is replaced by hydrogen. Hydrogen interacts with free radicals arising from the carbon surface, deactivating the radical species, leaving a uniform surface and the final PGC material (West *et al*., 2010).

1.4.3 Structure of porous graphitic carbon

The unique structure of PGC consists of flat, hexagonally arranged carbon atom sheets which carry a satisfied valence similar to graphite. However, unlike three-dimensional graphite, the sheet layers are not ordered in a regular fashion and so the material is said to resemble “two-dimensional” or “turbostratic” graphite known as a Warren structure (Warren, 1941) (Figure 1.17).

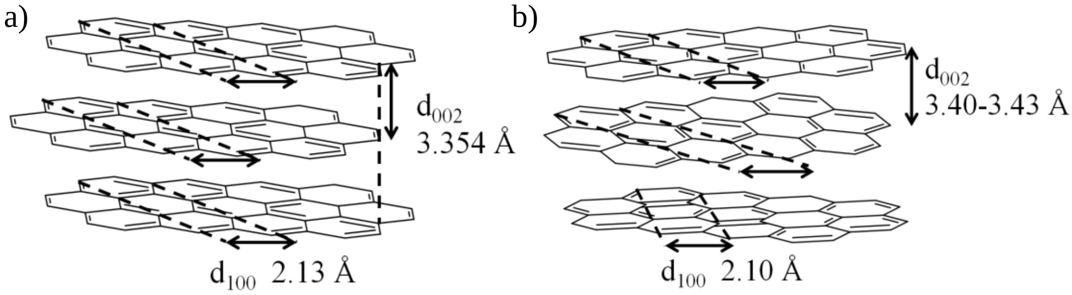

Figure 1.17: Structures of a) three-dimensional graphite and b) two-dimensional ‘turbostratic’ graphite as has been identified for PGC.

As a stationary phase material, PGC differs from silica in both its retentive and physical properties. The retention mechanism of PGC is based on the polar retention effect on graphite (PREG) effect, affected by an analyte’s polarity and planarity, and is determined by two factors: i) hydrophobic eluent-analyte repulsions, which occur between a hydrophilic eluent and non-polar segments of the analyte, ii) the interaction of polarizable or polarized functional groups in the analyte with the delocalised π-electrons of the graphitic plane (Knox and Ross, 1997). This second interaction type occurs in the form of charge-induced dipole-dipole interactions, with the energy of the dipole increasing with respect to surface polarisability and the charge distribution of the analyte, and decreasing at increasing distance from the graphitic plane (Figure 1.18).

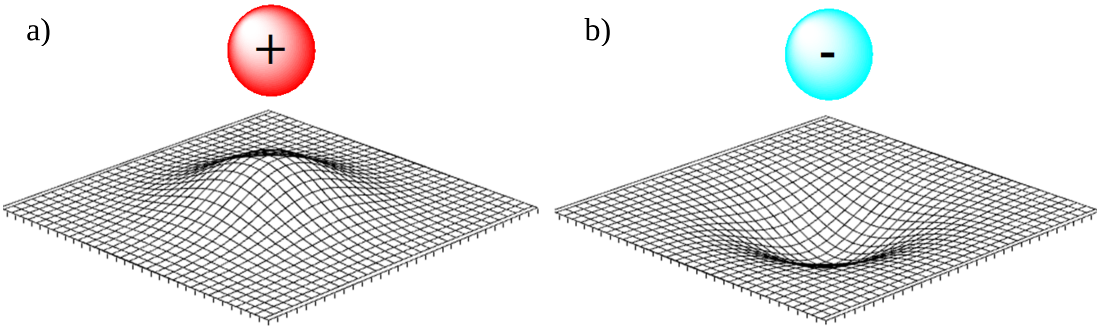

Figure 1.18: Charged-induced dipole-dipole interactions between PGC's graphite surface and (a) a positive or (b) a negative charge.

This second interaction type has also led to the opinion that the orientation of the analyte molecule at the surface has an impact on its retention, whereby the greater the molecular surface area in contact with the graphitic surface, the greater the retention of that analyte. This explains how isomers can be readily separated on a PGC column, as more planar molecules, or ones which orientate their polar functional groups close to the graphitic surface are more readily retained by the stationary phase.

1.4.4 Application as a separations medium

PGC columns have been used to separate a broad range of polar compound classes, owing to the unique chemical properties of the stationary phase. The benefit of the PREG effect has been used in the isomeric separation of several compound classes, including: alkylbenzenes (Kříž *et al*., 1994), nonylphenols (Gundersen, 2001), and oligosaccharides (Robinson *et al*., 2007). The strong retention of nitro groups at the PGC surface has led to the successful separation of explosive compounds (Holmgren *et al*., 2005; Buszewski *et al*., 2009). The ability to retain small polar compounds has found use in the analysis of food and environmental samples, for example, in the quantitation of the potential human carcinogen acrylamide (Rosen and Hellenäs, 2002; Becalski *et al*., 2003) and in the separation and quantitation of herbicides (e.g. atrazine) in ground and drinking water (Pichon et al., 1995; Dupas et al., 1996).

In addition, several modifications of the chemical properties of the PGC surface have been reported in order to separate particular compound classes; for example adsorption of chiral selectors has been used to improve the separation of chiral compounds using aryl anchors to ensure an even coating of the selector (Wan *et al*., 1997); adsorption of ionic compounds or polymers enhances ion exchange properties (Chambers and Lucy, 2007); electro-reduction of arene-diazonium salts onto the surface provides better protection against extreme changes in experimental conditions (Harnisch and Porter, 2001; Harnisch *et al*., 2001).

1.4.5 Hydrophilic interaction chromatography

Hydrophilic interaction chromatography (HILIC), otherwise known as aqueous normal phase chromatography, is another suitable technique developed after PGC for the separation of very polar compounds (Alpert, 1990; Alpert *et al*., 1994). Unlike standard NP-LC, HILIC differs by replacing the non-aqueous solvent used in NP-LC (e.g. hexane or chloroform) with a polar, mostly organic solvent (generally 5-40 % water in acetonitrile).

There is a broad range of HILIC stationary phase types, from classical bare silica beads and aminopropyl-bonded silica, to silica gels modified with polar functional groups. Examples of bound functionalities include amides, diols, cyclodextrin and the zwitterionic group sulfoalkylbetaine, with columns of this type (manufactured by Merck SeQuant®) termed ZIC-HILIC columns (Ikegami *et al*., 2008).

ZIC-HILIC columns are the most commonly used type of HILIC column. The zwitterion functionality is able to strongly retain water at its surface, creating a static layer. The partitioning effect caused by an analyte’s affinity for the water-enriched layer of the hydrophilic stationary phase and the hydrophobic bulk eluent is considered the basis for separation with HILIC (Hemström and Irgum, 2006). In addition, weak electrostatic interactions between the polar functional groups of the analyte and the stationary phase are also considered to be a part of the ZIC-HILIC retention mechanism (Alpert, 1990; Alpert *et al*., 1994).

The mobile phase system for HILIC can be readily used for on-line coupling of this method with mass spectrometry (MS). The high organic mobile phase gives enhanced MS sensitivity over wholly non-aqueous NP-LC. HILIC is not stable over the entire pH range like PGC, but it can offer a simpler solution to polar analyte separations since elution of highly polar compounds from PGC generally involves the inclusion of large amounts of modifier (e.g. formic acid or acetic acid), requiring extensive method development (Antonio *et al*., 2008a). However studies, such as that by Mauko *et al*. have shown how data provided by each technique can be mutually exclusive but can together be used to gain a better understanding of the system under study (Mauko *et al*., 2012).

1.5 Starbon®

The main disadvantages of PGC are the potential for permanent retention, the price of columns, its high environmental footprint and energy-intensive manufacture (section 1.4.2). Although there has been growing interest in using PGC over the past 20 years, there have been few reports of efforts made to drive development in this area likely owing to the fact that there is limited commercial competition.

In the mid 1990s, pioneering independent work by Glenn *et al.* and Te Wierik *et al*. described how porous aerogels could be produced from the gelatinisation and subsequent dehydration of starch (Glenn and Irving, 1995; Glenn and Stern, 1999; Te Wierik *et al*., 1996). Both reports described how different drying methods had diverse effects on the surface area and porosity characteristics of the aerogel product. In particular, Glenn *et al*. noted that the gel had to be washed in progressively lower surface tension solvents to prevent gel compression (Glenn *et al*., 1995). At the University of York, an expansion of the work by Glenn *et al.* led to the development of high surface area (ca. 120 $m^2 g^{-1}$), mesoporous corn starch-based materials, which were reported to be effective in heterogeneous base catalysis and in the normal-phase chromatographic separation of ferrocene compounds (Doi *et al*., 2002; Budarin *et al*., 2005).

The majority of early mesoporous carbons were prepared using a templating method in order to control surface and pore characteristics (Knox *et al*., 1986; Che *et al*., 1998; Lu *et al*., 2005). In addition, the inert hydrophobic surfaces generated by this method meant that functionalization of this surface, to open up further chemical applications, required additional difficult modification steps which reduced mesopore content (Li and Dai, 2005). Building on the potential of the corn starch-based mesoporous materials led to the development of a novel starch-derived mesoporous carbon material, termed Starbon®. Starbon® retains the naturally-templated pore structure of expanded starch, whilst the surface chemistry can be tuned depending on the final pyrolysis temperature, by exploiting the change in physical properties when converting the hydrophilic hydroxyl units of the glucose monomers into hydrophobic extended aromatic structures at high temperatures (Figure 1.19)(Budarin *et al*., 2006). Further functionalization by the simple addition of sulfuric acid led to the development of Starbon®-acids which have shown good potential in catalysis applications (Clark *et al*., 2009; Luque *et al*., 2011).

White *et al*. described how the textural and ordering properties of the expanded starch could be tuned depending on the relative amounts of amylose and amylopectin in the starch precursor (White *et al*., 2008). The higher the level of the linear glucose polmer amylose, the more stable the resulting dried material. On this basis, other linear polysaccharides were subjected to the Starbon® preparation process in order to extend the range of porous polysaccharide-derived carbon materials. Particular success was met with alginic acid and pectin, with the resulting porous carbon materials exhibiting greater mesopore content than the corn starch-based materials (White *et al*., 2009; White *et al*., 2010). Alginic acid-based Starbon® materials were studied as an alternative to activated carbons, commonly used in wastewater treatment, for dye adsorption. Parker *et al*. reported that Starbon® outperformed activated carbons in terms of both amount of dye adsorbed and percentage dye coverage per unit weight, as a direct result of the extended mesopore structure in the Starbon® materials (Parker *et al*., 2012).

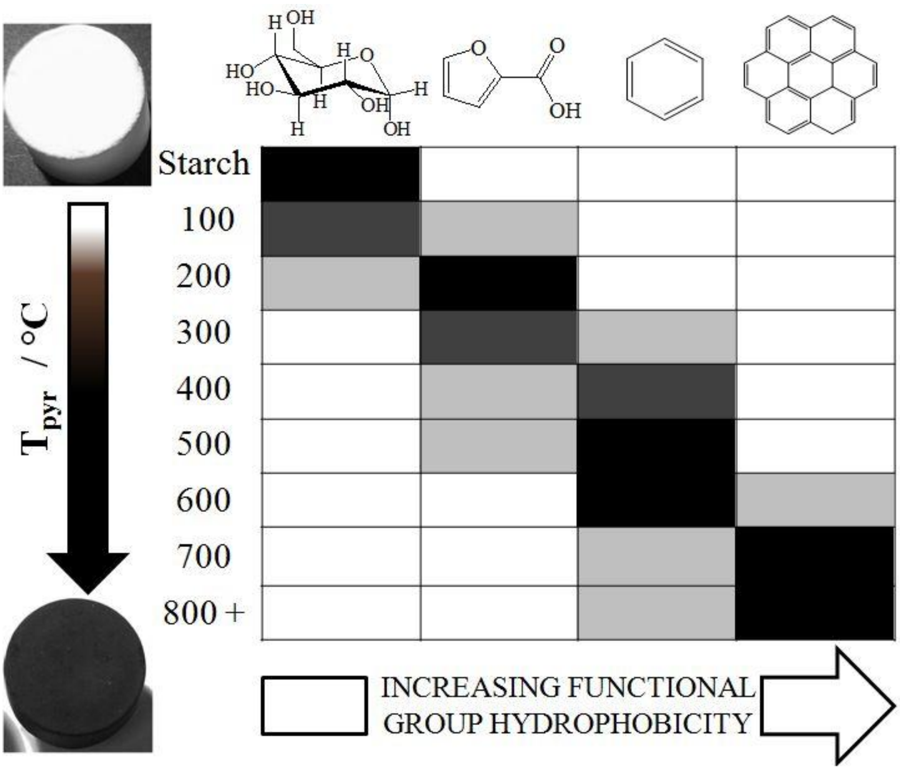

Figure 1.19: Starbon® functional group types as a function of pyrolysis temperature (T_{pyr}). As pyrolysis temperature increases, Starbon® passes from polysaccharide-derived funtionality through olefinic group functionality to extended aromatic structures. Relative amounts given by a colour scale where black represents the highest amounts.

The separation potential of alginic acid-based Starbon® was demonstrated by White *et al.*, with the liquid chromatographic separation of a mixture of carbohydrates using alginic acid-based Starbon® and a commercial PGC column (White *et al.*, 2010). The chromatographic performance of Starbon® was comparable to that of PGC in terms of analyte retention and isomer separation. This Starbon® material therefore, prepared from a biomass precursor using natural solvents (e.g. water, ethanol and $scCO_2$) and pyrolysed to just 1000 °C, offer a relatively simple and cost-effective alternative to the energy- and resource-intensive synthesis of PGC (White *et al.*, 2010). This initial demonstration formed the basis for the current research project, which aimed to build on the potential to develop alginic acid-based Starbon® materials for use in high performance liquid chromatography applications.

1.6 Biomass source - alginic acid

Alginic acid is a polysaccharide derived from various species of brown algae and certain bacteria. It is a linear copolymer consisting of β-1,4-linked D-mannuronic acid (M) and α-1,4-linked L-guluronic acid (G) (Figure 1.20). These monomers are generally arranged in homopolymeric blocks (i.e. –MMM- and –GGG-) which are separated by regions of an approximately alternating sequence of the two monomers (-MGMGM-). However, the length and order of these block units does not follow a regular repeating pattern. Bacterial alginic acid differs from the plant structure with the incorporation of an O-acetyl group at the C2 and/or C3 carbons (Draget et al., 2005).

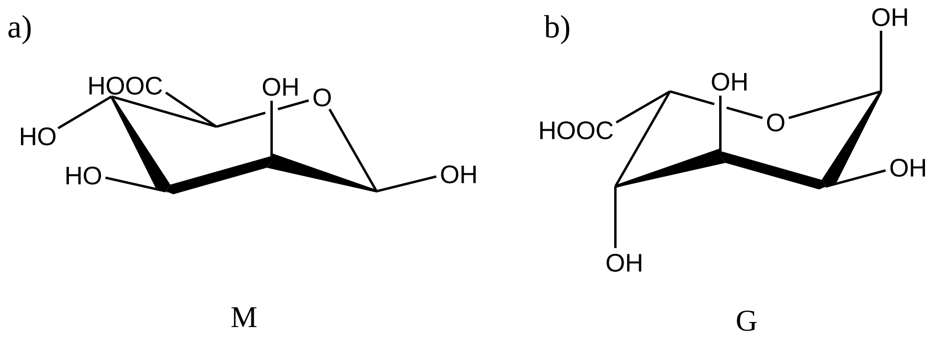

Figure 1.20: Structures of the alginic acid monomers (a) D-mannuronic acid and (b) L-guluronic acid.

Alginic acid is found in the cell walls of brown algae, and gives the organism both flexibility and strength, with the levels of mannuronic and guluronic acids varying between species. Alginic acid structures with a higher ratio of guluronic acid residues have a greater strength. Although the molecular weight range of alginic acid is polydisperse like most polysaccharides it can make up up to 40% of the dry matter of brown algae (Draget *et al*., 2005). The extraction of alginic acid from brown algae involves the initial separation of the polysaccharide from other structural residues by the addition of sodium ions to create sodium alginate. Sodium alginate is water soluble and so is extracted along with other carbohydrates present in the algae. By addition of a solution of calcium ions, displacement of the sodium from poly-G regions of the sodium alginate structure leads to the precipitation of an insoluble calcium alginate gel. This cross-linking gives rise to the structure described by the so-called “egg-box” model (Figure 1.21), involving two or more poly-G chains binding to the same metal ion (Grant *et al*., 1973). An FT-IR study by S. K. Papageorgiou *et al*. theorises that the calcium ion binds to the carboxylate group by a ‘pseudo-bridged’ unidentate interaction (Papageorgiou *et al.*, 2010). The calcium alginate is then filtered to remove the carbohydrates still in solution.

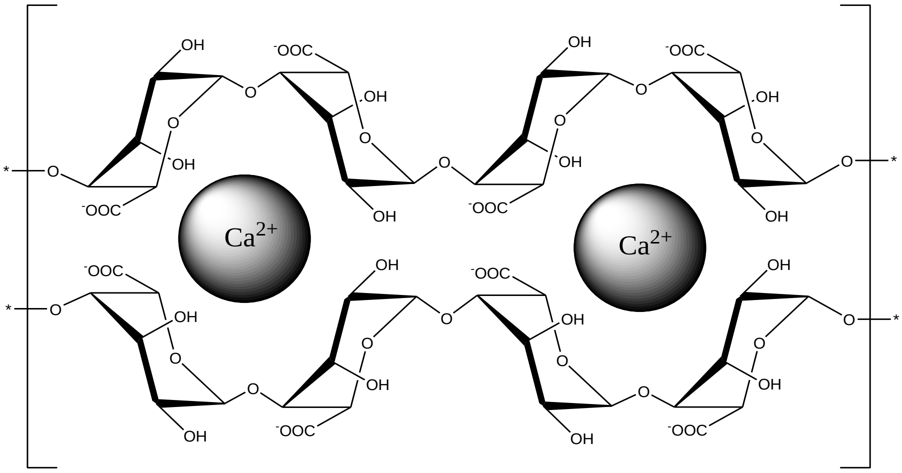

Figure 1.21: “Egg-box” model binding of Ca^{2+} metal ions to guluronic acid blocks

1.6.1 Applications of alginates

Alginic acid is used in a number of applications in its various alginate forms, due to the interesting gelling properties developed from the sol-gel transition which occurs in the presence of multi-valent cations (uniquely, a temperature independent process), and which makes these materials useful as immobilisation matrices.

Food industry: Propylene glycol alginate (PGA), a synthetic derivative of alginic acid, is used as a stabiliser by enhancing the viscosity of foodstuffs through interaction with the positively-charged amino acid residues of denatured proteins. PGA is prepared by partial esterification of the alginate carboxylic acid with propylene oxide and is most stable in acidic conditions as these reduce the hydrolysis rate of both the alginic acid and the propylene oxide (Steiner and McNeely, 1950). Alginates have also been used in food re-structuring as binders for milled food (for example, sodium alginate acts as a binder for the olive filling ‘pimiento’) (Draget *et al.*, 2005). The use of alginates in the food industry is considered safe so that all of these applications are EC approved.

Medicine and pharmaceutical industry: Alginate gels have been used as scaffolds in tissue engineering in order to hold structural loads whilst new cells are developing, due to its advantages of being both biocompatible and non-immunogenic, whilst also having the ability to encapsulate drugs or cells with minimal trauma (Tønnesen and Karlsen, 2002; Augst *et al*., 2006; Bulut and Sanli, 2013). When enough cells have accumulated in the gel, degradation of the alginate material is required to allow the integration of the new cells into the surrounding tissue, as well as give room for further cell growth. However, a disadvantage to using alginate materials in medicine is that they are not naturally degraded by the body and so other methods are needed. Common procedures include the use of gamma irradiation to break M-G bonds and hydrolysis using sodium periodate (Augst *et al*., 2006).

The attachment of cells to alginates is difficult owing to alginate's relative inertness due to a lack of mammalian receptors. A fibronectin-derived arginine-glycine-aspartic acid (RGD) sequence is commonly used for adhesion as it is readily linked to the alginate through the use of carbodiimide chemistry (Augst *et al*., 2006). For example, Grimmer *et al.* created chrondocyte-seeded RGD-alginate embedded in PGA meshes for use in tracheal reconstruction (Grimmer *et al*., 2004).

Other industries: Alginate gels are also used in the textiles industry as shear-thinning viscosifiers, due to the high colour yield, print levelness and brightness they deliver (Draget *et al*., 2005). Ammonium alginate is used as a sealant (Draget *et al*., 2005) whilst other alginates have been used as biological detergents (Liu *et al*., 2005) as well as in industrial fermentation (Casson and Emery, 1987).

1.6.2 Sustainable harvesting of brown algae

Brown algae, otherwise known as kelps, are generally subtidal species (i.e. submerged at high and low tides) and are the raw material required for alginate manufacture. Brown algae can be found in large quantities off the west coasts of Scotland and Ireland. Extrapolation of the results of kelp surveys by Kain in the Outer Hebrides and Isle of Man (1977) and Jupp and Drew in Western Scotland (1974) provides an estimate of 30-50 million tonnes on the British and Irish coastlines, of which *Laminaria hyperborea* is the most dominant kelp species (Jupp and Drew, 1974; Kain, 1977). Until recently, alginate was produced in Scotland by FMC BioPolymer, formally ISP Alginates Ltd.. However, this production was later moved to Haugesund, Norway.

In 2009, 26500 tonnes of alginate were produced, with the largest commercial producers being China which has algae farms able to produce 5-7 million tonnes of the brown alga *Laminaria japonica*; however, the alginates produced are of poor gelling quality due to the low poly-G content of this species (Draget *et al*., 2005). The other major alginate producers are the USA and Norway, with Norway accounting for two-thirds of the annual production of alginate in Europe and specialising in ultra-pure alginates (derived from the high poly-G-yielding species *Laminaria hyperborea*) for food and pharmaceutical applications (Bixler and Porse, 2011).

China uses a "hanging rope" method in order to cultivate the kelp species *Laminaria japonica*, involving the seeding of algal spores onto ropes which then grow into kelp fronds. The development of seedlings which spore in the summer, along with improved sea-fertilizing methods have enhanced this mariculture technique for large-scale production (Tseng, 2001).

Norway has an estimated 10 million tonnes of *Laminaria hyperborea* on its coastlines. The Norwegian harvest is collected from four geographical regions, each of which is split into five sub-areas. A five-year cycle is in operation whereby one sub-area is harvested in a year and is then not re-harvested for at least five years, allowing the area time to recover. Due to the density and mixed age of sub-storey algae (below the main canopy of kelp), *Laminaria hyperborea* is resistant to intensive farming, making it ideal as a sustainable material source (Kelly and Dworjanyn, 2008). With such a large quantity of this algae around British and Irish coastlines and by following the harvesting techniques of Norway, the sustainable production of alginates could be possible again.

By utilising the natural gelation of alginic acid in water to develop porosity within the materials, Starbon$^{®}$ could offer a sustainable biomass-derived alternative to PGC so long as the pore networks generated are predominantly mesoporous. Nitrogen porosimetry is commonly used to characterise material pore structure in the micropore/mesopore and low macropore range.

1.7 Characterisation of pore structure - nitrogen porosimetry

Nitrogen adsorption porosimetry is considered to be the standard method for the characterisation of porous solids, measuring the adsorption of a gas (known as the adsorptive) to the accessible interfacial layer of the solid, from which the total surface area and pore size distribution can be calculated using gas law theory (Sing *et al.*, 1985).

The measurements are collected in a closed vessel of known volume in which the solid is exposed to a gas at a defined pressure. Under these conditions, the solid adsorbs the gas molecules at its surface through physisorption, whereby the pressure within the vessel decreases until adsorption ceases, at which point the pressure remains constant and a monolayer of the gas is formed. This process is repeated with successive injections of gas into the vessel, creating multilayers of the gas and the pressure change is measured until no further adsorption occurs. This phenomenon of monolayer-multilayer formation is known as the Kelvin model for pore filling. DeBoer and Zwikker explained that the formation of the monolayer arose from a dipole-dipole interaction induced by the ionic surface of the solid in the non-polar gas molecules (DeBoer and Zwikker, 1929). Further layers are formed as the dipolar monolayer further induces dipole interactions in other non-polar gas molecules which are forced into the solid at higher pressures. Capillary condensation occurs when the pore is saturated (Figure 1.22).

Plotting the amount of gas adsorbed against the associated relative pressure (P/P_o, where P_o is the saturation pressure of the gas) gives the adsorption isotherm of the material (Gregg and Sing, 1982). For accurate analyses, the measurements must be taken at constant temperature. In the case of nitrogen porosimetry analyses are conducted at 77 K, the temperature of liquid nitrogen. Physisorption behaviour varies according to the type of pore network analysed. However, it was discovered that the overall shapes of the adsorption isotherms obtained could be classified into six main types (Sing *et al.*, 1985), summarised in Figure 1.23.

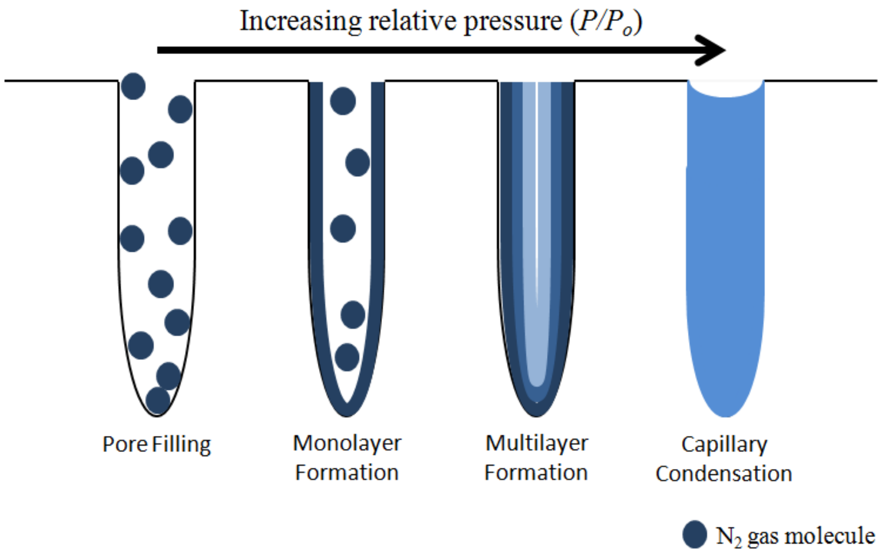

Figure 1.22: Capillary condensation as a consequence of increasing N_2 relative pressure (P/P_o)

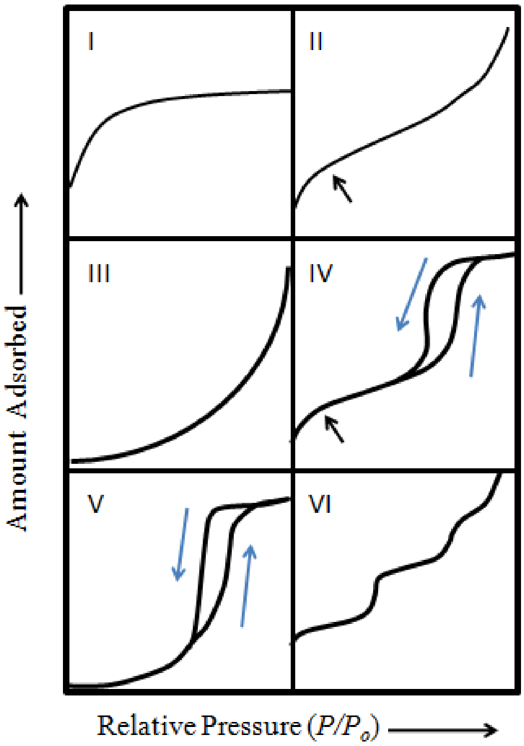

Figure 1.23: Types of adsorption isotherms. The black arrows in the Type *II* and Type *IV* isotherms refer to the point where monolayer coverage is obtained and multilayer coverage is initiated. The blue arrows in the Type *IV* and Type *V* isotherms refer to the adsorption (up) and desorption (down) curves associated with capillary condensation.

The Type *I* isotherm is generally observed for microporous solids with small external surfaces, such as activated carbons and zeolite catalysts. The Type *I* isotherm tends to slope parallel towards the P/P_o axis as the amount of gas adsorbed approaches the limit, caused by saturation of the inherent micropore volume, where P/P_o tends to 1 (Sing *et al*., 1985).

The Type *II* isotherm is generally observed for non-porous solids and concerns the simple monolayer-multilayer adsorption of the gas to the surface of the solid. The black arrows (Figure 1.23) represent the point of total monolayer coverage over the solid surface, i.e. initiation of multilayer formation (Gregg and Sing, 1982).

The Type *III* isotherm is less common but represents systems with weak/strong adsorbate-adsorbate interactions. This is indicated by the exponential increase in the amount of gas adsorbed at higher P/P_o, as the gas molecules are forced to form a monolayer at the surface of the solid for which it has limited attraction. In these cases, over-estimation of the surface area can arise as the gas molecules can tend to cluster.

The Type *IV* isotherm is representative of mesoporous solids and, along with the more uncommon Type *V* isotherm, is characterised by a hysteresis loop. The lower curve of the loop is plotted with measurements based on the progressive addition of gas into the solid (i.e. adsorption), whilst the upper curve of the loop represents measurements taken as gas is withdrawn from the solid (i.e. desorption). The appearance of the hysteresis loop is associated with capillary condensation (where P/P_o reaches a point that causes the condensation of the gas at the surface of the solid, so creating a liquid surface at which further adsorption takes place at the liquid meniscus) which occurs in mesopores. The Type *IV* isotherm follows a similar monolayer-multilayer adsorption profile as the Type *II* isotherm and so it is also possible to visualise the point of total monolayer coverage of the solid.

The Type *VI* isotherm represents stepwise multilayer adsorption onto a uniform non-porous surface. The steps vary in height depending on the monolayer capacity of a particular adsorbed layer (Sing *et al*., 1985).

The work described in this thesis follows a Type *IV* isotherm profile. The Type *IV* isotherm has itself been sub-divided into four types; H1, H2, H3 and H4 (Figure 1.24) which represent different hysteresis loop shapes, whereby the adsorption and desorption of the nitrogen adsorbate progress through different mechanisms, associated with varying pore structures. The pore-blocking theory is used to describe the formation of a hysteresis loop, whereby desorption of the condensed liquid from a large pore is delayed if the only available avenue to the vapour phase is through an adjacent smaller pore (McBain, 1935; Rigby and Fletcher 2004). The typical example of this type of system is an "ink-bottle pore".

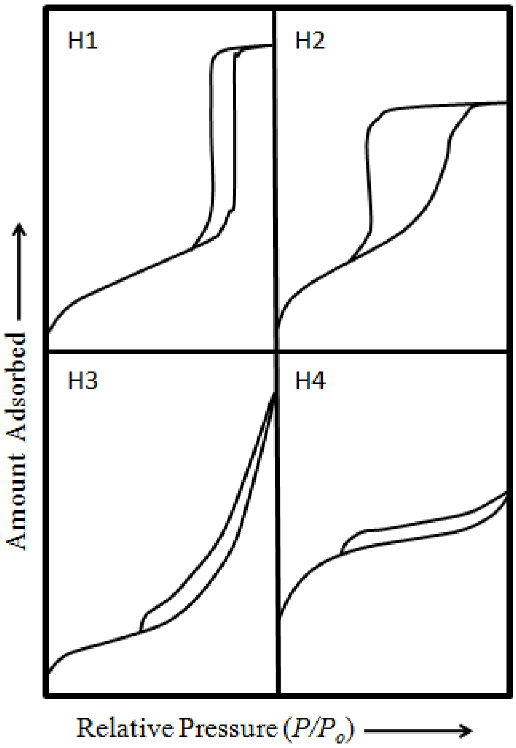

Figure 1.24: Hysteresis loop sub division of the Type *IV* isotherm

The H1 type hysteresis loop is associated with porous solids which consist of agglomerates (a rigid, consolidated assemblage of particles) or regular, compact particles yielding a narrow distribution of pore sizes (Sing *et al.*, 1985). Type H2 loops tend to be observed in porous materials where the pore size and shape is not well-defined. Type H3 loops, where there is no limiting adsorption at high P/P_o, are observed for aggregates which consist of slit-shaped pores. Type H4 loops, whilst similar to H3 loops in association with slit-like pores, are an indicator of microporosity.

1.7.1 Determination of surface area

The Brunauer Emmett Teller (BET) theorem is the most widely used method to calculate the surface area of porous materials. The derivation is based on the assumption that the forces which act on the monolayer to cause capillary condensation also act to allow multilayer adsorption (Brunauer *et al*., 1938). The linear form of the BET equation is shown in Equation 1.20.

$$P / \upsilon(P_o - P) = (1 / \upsilon_m C) + (C - 1 / \upsilon_m C) \cdot P/P_o \qquad \textbf{Equation 1.20}$$

where υ is the total volume of the gas adsorbed at a particular pressure P; υ_m is the volume adsorbed where there is total monolayer coverage (known as monolayer capacity); P_o is the saturation pressure of the gas and C is a constant related to the enthalpy of adsorption of the monolayer (Brunauer *et al*., 1938).

Once the monolayer capacity is calculated, this result can be used to determine the specific surface area S_{BET} of the solid using Equation 1.21 (Sing *et al*., 1985; Rouquérol *et al*., 1994).

$$S_{BET} = \upsilon_m \cdot a_m \cdot N_A \cdot 10^{-20} \qquad \textbf{Equation 1.21}$$

where a_m is the cross sectional area of the monolayer that a single gas molecule occupies assuming a close-packed structure (for nitrogen a_m = 0.162 nm^2 at 77 K) and N_A is the Avogadro constant.

Although BET is the established method for surface area determination, it is widely known that it provides only the simplified view that monolayer-multilayer coverage is the sole process operating during gas adsorption and the process of micropore filling is absent from the calculation (Sing *et al*., 1985). However, the calculated surface area generally falls within the acceptable variance range of surface area values for a solid, so that the method and its data continue to be accepted.

1.7.2 Determination of pore size distribution

Most solids are porous in character, with truly non-porous materials being very rare. Porosity refers to the pore space of a material, where a pore is defined as a void which is deeper than it is wide (Rouquérol *et al.*, 1994). Figure 1.25 highlights the six types of pore architecture commonly found in porous solids. These are made up of open pores (pores in communication with the external surface) and closed pores (pores with no communication to the external surface). Due to the varieties of open pore architecture possible, these are further defined by their shape. Pores are also split into three size ranges: micropores (below 2 nm), mesopores (2 – 50 nm), and macropores (above 50 nm) (Everett, 1972). Solids with a high surface area are likely to have a higher ratio of micropores compared to low surface area solids.

Figure 1.25: Common pore architecture in porous solids, a) closed pore; open pores, b) ink-bottle shaped, c) open cylindrical, d) open-ended (through pore), e) funnel or slit shaped, f) blind cylindrical. Reproduced from (Rouquérol *et al.*, 1994)

The established method for determining pore size distribution in the mesopore region is the Barrett Joyner Halenda (BJH) method (Barrett *et al.*, 1951). This theorem is based on the Kelvin equation (Equation 1.22) which calculates the Kelvin radius (r_k), which itself is based on the curvature of the liquid meniscus formed by capillary condensation and the associated pressure change that occurs, as described by W. Thomson in 1871 (Thomson, 1871; Sing *et al.*, 1985). From equation 1.22, the radius of a cylindrical pore (r_p) can be calculated using Equation 1.23.

$$r_k = (2.\ \sigma^{lg}\ .\ \upsilon^{l}) / (R\ .\ T\ .\ ln(P_o / P))$$ **Equation 1.22**

where $\boldsymbol{\sigma^{lg}}$ is the surface tension of the liquid condensate and $\boldsymbol{\upsilon^{l}}$ is the molar volume of the liquid condensate.

$$r_p = r_k + t$$ **Equation 1.23**

where $\boldsymbol{t}$ is the multilayer thickness, a correction factor to take into account the gas already adsorbed at the solid surface.

The BJH method is based on the analysis of the relationship between the nitrogen isotherm and the distribution of pore volume and area with respect to pore radius. The BJH method makes two assumptions; firstly, that pores are cylindrical in shape (also a requirement for the Kelvin equation), and secondly that the gas phase and adsorbed phase equilibrium during desorption is based on two mechanisms i) physical adsorption on the surface, and ii) capillary condensation filling. The BJH equation is given in Equation 1.24 (Barrett *et al.*, 1951).

$$V_{pn} = R_n . \Delta V_n - R_n . c . \Delta t \sum_{j=1}^{n-1} A_{pj}$$ **Equation 1.24**

where $\boldsymbol{V_{pn}}$ is the pore volume at n^{th}desorption; $\boldsymbol{R_n}$ is a simplification relating to the pore radius where $R_n = r_{pn}^2/(r_{kn} + \Delta t_n)^2$ at the n^{th} desorption; $\boldsymbol{\Delta t}$ is the change in thickness of the physically adsorbed gas layer since the previous desorption step, i.e. the $n - 1^{th}$ desorption; $\boldsymbol{\Delta V_n}$ is the observed volume of gas desorbed at a relative pressure; $\boldsymbol{\sum_{j=1}^{n-1} A_{pj}}$ is the summation of the areas of each pore and $\boldsymbol{c}$ represents the ratio of the averaged Kelvin radius over the averaged total pore radius.

In practice, computation to determine the pore size distribution is carried out by plotting $\boldsymbol{\Delta V_n / \Delta r_p}\ vs\ \boldsymbol{r_p}$ where the plot is limited to calculating the distribution up to pore radii of 300 Å (Barrett *et al.*, 1951). This limit is imposed due to the logarithmic relationship between pore radius and relative pressure, which means that to observe change in pore volume at pressures approaching unity, a larger increments of pore radii must be used at each sample point and the method becomes impracticable. In addition, the relative area of pores of large radii represent only a small fraction of the overall material, hence are unlikely to make a significant contribution to the surface characteristics. Nitrogen porosimetry is therefore unable to determine the pore size distribution of large macropores, and mercury porosimetry is the preferred method for studying these pores. Likewise, the BJH method begins to break down for the microporous region (sub-2 nm) since the model does not take into account the mechanism of micropore filling, the same limitation as seen with the BET theory (Sing et al., 1985; Rouquérol *et al*., 1994).

1.8 Aims of this thesis

The aims of the work described in this thesis may be split into two branches. The first branch aimed to optimise the synthesis of an alginic acid-derived porous carbon material, termed Starbon®, for application as an HPLC stationary phase material. The optimisation aspects described were driven by the need to improve the size and morphology of Starbon® particles to enhance the packing efficiency of this material. The effects of the synthesis process on mesopore structure, a key feature of the material for this application, were also monitored and the surface chemistry of the resulting materials was investigated. The second branch involved the use of the commercially equivalent porous carbon column (PGC), in both targeted and untargeted LC-MS-based approaches, to determine the effect of water deficit on the primary metabolome of several model plant species.

Chapter 2 describes the application of a negative ion mode on-line PGC-LC-ESI-QIT-MS method for studying the changes in the levels of targeted carbohydrates from *Haberlea rhodopensis* leaf blade tissues in response to different water deficit stresses: mild drought, severe drought and rewatering.

Chapter 3 describes the application of a negative ion mode on-line PGC-LC-ESI-QTOF-MS method for the comparison of water deficit effects on the water soluble metabolite fractions from leaf blade samples of two model plant systems; *Arabidopsis thaliana* and *Thellungiella salsuginea*. Untargeted statistical analysis was used to analyse the data from several stress states to determine metabolite changes which are conserved and which differ between the two plant species.

Chapter 4 describes an investigation into the effect of pyrolysis rate on Starbon$^{®}$. Several pyrolysis rates were used and the effects on the pore structure of the resulting materials were analysed by N_2 porosimetry, thermal gravimetry and dye adsorption techniques.

Chapter 5 describes the approaches used to optimise the particle size and morphology of Starbon$^{®}$. The results of milling, spray drying and the formation of carbonised calcium alginate beads are presented and discussed. The peak efficiency of a column packed with material generated using the optimised preparation procedure was investigated and comparisons with PGC and a column packed with Starbon$^{®}$ are made and discussed.

Chapter 6 describes the investigation comparing the surface chemistry characteristics of PGC, Starbon$^{®}$ and carbonised calcium alginate beads using transmission electron microscopy. The carbon hybridisation of the three materials, determined by core loss electron energy loss spectroscopy, is discussed and comparisons are made with model non-graphitising carbons. The chemical environments of carbon and calcium were determined by X-ray photoelectron spectroscopy and a potential mechanism of catalytic graphitisation is proposed and discussed.

Chapter 2

Porous graphitic carbon liquid chromatography electrospray ion trap mass spectrometry for the targeted analysis of carbohydrates in *Haberlea rhodopensis* in response to water deficit

The work described in this chapter has been published in:

Molecular mechanisms of desiccation tolerance in the resurrection glacial relic *Haberlea rhodopensis*

***Cellular and Molecular Life Sciences*, 70 (2013) 689-709**

Tsanko S. Gechev[1], Maria Benina[1], Toshihiro Obata[2], Takayuki Tohge[2], Neerakkal Sujeeth[1, 3], Ivan Minkov[1], Jacques Hille[3], Mohamed-Ramzi Temanni[4], Andrew S. Marriott[5], Ed Bergström[5], Jane Thomas-Oates[5], Carla Antonio[2], Bernd Mueller-Roeber[2, 6], Jos H. M. Schippers[2, 6], Alisdair R. Fernie[2], Valentina Toneva[1]

[1] Department of Plant Physiology and Plant Molecular Biology, University of Plovdiv, 24 Tsar Assen str., Plovdiv 4000, Bulgaria

[2] Max Planck Institute of Molecular Plant Physiology, Am Mühlenberg 1, D-14476 Potsdam-Golm, Germany

[3] Molecular Biology of Plants, Groningen Biomolecular Sciences and Biotechnology Institute, University of Groningen, The Netherlands

[4] ServiceXS B.V., Plesmanlaan 1d, 2333 BZ Leiden, The Netherlands

[5] Department of Chemistry, University of York, Heslington, York, YO10 5DD, UK

[6] University of Potsdam, Institute of Biochemistry and Biology, Karl-Liebknecht-Str. 24-25, Haus 20, 14476 Potsdam-Golm, Germany

2.1 Introduction

The term 'metabonomics' was first defined in 1999 by Nicholson *et al.* as the "quantitative measurement of the time-related multiparametric metabolic response of living systems to pathophysiological stimuli or genetic modification" (Nicholson *et al.*, 1999). Metabolomics is the comprehensive study of the complete pool of low molecular weight metabolites synthesised by an organism (i.e. the organisms' metabolome) at a particular point in time. The terms metabolomics and metabonomics are often used synonymously (Nicholson and Lindon, 2008). However the key difference is that whilst metabolomics quantifies cellular systems as a "snap-shot" in time, metabonomics can be considered a full systems biology approach. Metabonomics studies aim to measure the whole organism (comprising of multiple cell and tissue systems) over a full time-course that takes into account metabolite fluctuations to stimulus (Lindon *et al.*, 2003).

The metabolome of an organism can be studied on its own or in parallel with transcriptome (transcriptomics), genome (genomics) and proteome (proteomics) analyses, in order to enhance our understanding of the correlation between gene function (genotype) and environmental response (phenotype) to a particular internal or external stimulus at the cellular level (Oliver *et al.*, 1998). In 2001, Fiehn proposed further differentiating four distinct approaches to analysing metabolic data, aimed at answering specific questions about the organisms' metabolome. Metabolomics is one approach whilst the other three strategies are *target analysis*, *metabolite profiling* and *metabolic fingerprinting*. Target analysis involves the qualitative and quantitative analysis of compounds constrained to a specific pathway. Metabolite profiling broadens the scope of target analysis to elucidating and quantifying pre-defined classes of compounds (e.g. carbohydrates, polar lipids or steroids) which are involved with a particular pathway or groups of interconnecting pathways. Metabolic fingerprinting involves the rapid screening of samples to enable classification based on origin or biological relevance. Metabolic fingerprinting is considered a high-throughput, diagnostic approach to metabolome analysis and as such less emphasis is placed on quantitation of individual metabolite levels compared to the other approaches (Fiehn, 2001; Fiehn, 2002).

Plant metabolomics is the study of the plant metabolome by analysis of plant samples extracted under specific conditions. It is estimated that there are up to 200,000 different metabolites across all species of the plant kingdom, with a diverse range of chemical properties, and ranging from femtomolar to millimolar in concentration, creating a highly complex system (Fiehn 2002; Fernie, 2003).

Abiotic stresses are environmental factors which have detrimental effects on crop growth and yield. The main abiotic stresses are temperature, drought, salinity, heavy metals and radiation. Drought stress in particular is becoming more prevalent, even in regions throughout the globe where this issue had previously been negligible, owing to the increasing changes in the global climate (Chaves and Oliveira, 2004). Recently, research has been aimed at understanding the mechanisms behind water deficit (WD) in plant species, some of which are known as resurrection plants. The aim is to improve crop management in ‘sub-optimal’ or marginal environments and ultimately develop crop phenotypes which can survive in particular drought-prone areas (Chaves and Oliveira, 2004).

In Europe, only two genera of angiosperms are considered to be resurrection plants, namely *Ramonda* and *Haberlea* from the family Gesneriaceae. These plants tend to grow on rocky surfaces, at a range of altitudes in mountainous regions. In particular, the species *Haberlea rhodopensis*, one of the first plants to be identified as a resurrection plant, is commonly used as a model species to study WD mechanisms.
H. rhodopensis is homoiochloropyhllous meaning that it has adapted to survive for short periods of desiccation, from a few hours to several weeks, whilst preserving its chlorophyll for easy and rapid recovery upon rehydration (Djilianov *et al*., 2011). Further adaptations include the upregulation of abscisic acid during drought which initiates stomatal closure, the accumulation of amino acid and other antioxidants in order to scavenge free radicals (Seki et al., 2003). In addition to this, stress-responsive gene expression and metabolic changes occur, including the alteration of lipid and sterol levels in order to stabilise cell membranes (Markovska *et al*., 1992). Carbohydrates (in the form of soluble sugars or sugar alcohols) are known to act as osmolytes to retain cell turgor pressure (Chaveas and Oliveira, 2004; Seki *et al*.,

2003), whilst it is believed they also play a role in stabilising proteins and other cellular structures (Bartels and Sunkar, 2005).

Although understanding the metabolism of carbohydrates is key to underpinning the overall biochemical pathways behind drought resistance in these plants, the compounds themselves are difficult to analyse owing to their high polarity, poor UV absorbance and the variety of isomeric structures (Antonio *et al*., 2008b). High performance anion-exchange liquid chromatography (HPAEC) with pulsed ampometric detection (PAD) has been often used for the analysis of carbohydrates (Stroop *et al*., 2002; Schiller *et al*., 2002; Guignard *et al*., 2005). However due to the high salt concentration in the mobile phase systems involved can lead to ion suppression when directly coupled with MS; a useful technique for the structural elucidation of metabolites. Generally post-column dilution with the direct addition of pure water or the formation of pure water by electrochemical desalting is used to reduce salt levels, although dilution reduces detection sensitivity (Guignard *et al*., 2005). There are several alternatives to HPAEC-PAD for carbohydrate analysis.

Normal phase (NP) columns have been used in the form of β-cyclodextrin-based stationary phase, which separates carbohydrates using a combined anion-exchange and hydrophilic interaction mechanism, whilst the chiral nature of β-cyclodextrin also enables this stationary phase type to separate sugar enantiomers (Armstrong and Jin, 1989; Schumacher and Kroh, 1995; Feurle *et al*., 1998). Use of ydrophilic interaction chromatography (HILIC) has grown in the field of metabolomics over recent years (Cubbon *et al*., 2010). Example applications of HILIC to plant metabolomics include Tolstikov and Fiehn, who reported a method using HILIC columns coupled to MS for the separation and quantitative analysis of polar metabolites, including carbohydrates and amino acids, in *Cucurbita maxima* leaf phloem tissue (Tolstikov and Fiehn, 2002); whilst Antonio and coworkers described a HILIC/ESI-MS method for the separation of a diverse range of carbohydrate-based metabolites applied to the analysis of *Arabidopsis thaliana* leaf tissue (Antonio *et al*., 2008a).

Ion pair chromatography has also been used in carbohydrate separations. This approach uses a reversed phase (RP) mobile phase system but which includes a ion-pairing reagent (e.g. alkylsulfonic acid or quarternary ammonium salts) in the organic solvent. These large ionic species have an opposite charge to the compounds analysed, effectively neutralising the polar analytes, whilst the hydrophobic regions of the salt enable interaction with the column stationary phase. Ion pair chromatography has been successful for the separation of charged carbohydrates e.g. sulfated glycans (Guo and Conrad, 1988; Karamanos et al., 1997). However, the separation of neutral carbohydrates requires the use of derivatising agents in order to induce the species charging required for generation of the ion pair (Kim *et al.,* 1995; Gennaro *et al*., 2003).

PGC chromatography is another alternative separation technique and has several advantages over standard RP-, NP-, HPAEC, and ion pair columns. These include the ability to separate polar species using MS-compatible RP mobile phase (without the need for derivatising agents), and stability over the 0-14 pH range. The separation of water soluble mono-, di-, and oligosaccharides for WD plant metabolomics studies using PGC chromatography has been reported previously for *Arabidopsis thaliana* (Antonio *et al*., 2007), *Triticum aestivum* (Robinson *et al*., 2007) and *Lupinus albus* (Antonio *et al*., 2008b).

There have been a few studies looking at the effect of WD on the carbohydrate levels of *H. rhodopensis* and have been performed using HPAEC-PAD (Djilianov *et al*., 2011) and gas chromatography (Müller *et al*., 1997) techniques. The work in this chapter describes the development of a robust PGC-LC-MS method for the targeted quantitative analysis of carbohydrates from *H. rhodopensis* leaf blade tissues and their changes in response to water deficit. This work formed part of a collaborative project aimed at combining physiological, metabolome, and transcriptome data to comprehend the intricate response of *H. rhodopensis* to mild drought (4-day WD), severe desiccation (20-day WD), and desiccation followed by subsequent rehydration.

2.2 Aim

The work described in this chapter is part of a collaborative project carried out with the Max Planck Institute of Molecular Plant Physiology, Germany, and the University of Plovdiv, Bulgaria.

The aim of the study in this chapter was to analyse the progressive effects of drought stress on leaf blade tissues of *H. rhodopensis*. Samples of soluble metabolites extracted from control, mild drought, severe desiccation, and desiccation followed by subsequent rehydration conditions were analysed by PGC-LC-ESI-quadrupole ion trap (QIT)-MS and targeted quantitative analysis of the data was performed. The general aims of the work in this chapter are summarised as follows:

- Development of a robust PGC-LC-ESI-QIT-MS method for the analysis of water soluble carbohydrate metabolites.
- Targeted quantitative analysis of selected carbohydrates in drought-stressed *H. rhodopensis* leaf blade samples.
- Comparison of results observed for against available literature on WD response in plant systems.

2.3 Experimental

2.3.1 ***Haberlea rhodopensis* growth and sampling conditions**

Plant growth and sampling were carried out by collaborators Maria Benina (University of Plovdiv, Bulgaria) and Dr Carla Antonio (Max Planck Institute - Golm, Germany). *H. rhodopensis* collected from its natural habitat in the Rhodope mountains was grown in a climate-controlled room on their natural soil at 21^{o}C, 20 μE m^{-2} s^{-1} light intensity, 16-h/8-h photoperiod, and 65% relative humidity. This was the natural light intensity below the trees where *H. rhodopensis* was collected, so that this light intensity was maintained throughout the experiments. For the water stress treatment, water supply was withheld and samples for the mild drought time point and the desiccation time point were taken after four (4-day WD) and 20 days (20-day WD), when the relative water content (RWC) reached 50% and 5%, respectively. Relative water content (RWC) was measured using the formula RWC (%) = [(FM - DM)/(TM - DM)] * 100, where FM, DM, and TM are the fresh, dry and turgid masses of the leaves, respectively. TM was measured after immersing the leaves in H_2O for 24 h and DM was determined after drying the leaves at 80 ^{o}C for 48 h. Rehydration was achieved by resuming water supply and samples were taken when plants regained their normal appearance and RWC four days after re-watering. In all cases fresh rosette leaves were used as samples and were immediately frozen in liquid nitrogen and ground to a fine powder.

2.3.2 Extraction of *Haberlea rhodopensis* soluble metabolites

Metabolite extraction was performed by collaborators Maria Benina (University of Plovdiv) and Carla Antonio (Max Planck Institute - Golm). Primary metabolites were extracted using a methanol/chloroform extraction as previously described (Lisec et al, 2006). Briefly, a total of 20 mg (FW) of powdered leaf material was homogenized in 280 µL of 100 % (v/v) methanol. Extracts were incubated for 15 min at 70 °C on a shaker (950 rpm) and then centrifuged at room temperature, 12,000 *g* for 10 min. The supernatant was transferred to a new tube and mixed with 150 µL chloroform and 300 µL water, and vortex mixed. Extracts were centrifuged at room temperature, 12,000 *g* for 15 min, and aliquots of the resulting polar (upper) phase were taken for further analysis. A total of 150 µL aliquots of the polar phase were evaporated to dryness using a centrifugal concentrator and stored at -80 °C until analysis.

2.3.3 Materials and solvents for targeted analysis

Analytical-grade water and solvents used for chromatography were purchased from Fisher Scientific (Loughborough, UK). The carbohydrate standards fructose, glucose, galactinol, raffinose, stachyose and verbascose were purchased from Sigma Aldrich (Poole, UK); sucrose was purchased from BDH (Poole, UK).

2.3.4 Plant metabolite extract sample preparation

Standard stock solutions of fructose, glucose, galactinol sucrose, raffinose, stachyose and verbascose were prepared in water at a concentration of 1.0 mg mL^{-1} and stored at -20 ^{o}C prior to use. Calibration standards were prepared from these stock solutions by dilution with water. The frozen extracts of the plant material were reconstituted in 150 µL water followed by centrifugation at 10,000 *g* at ambient temperature for 20 min. The supernatant was then analysed by liquid chromatography ion trap mass spectrometry. Due to the high concentrations of the target analytes sucrose and raffinose in these samples, a further 50-fold dilution in water of an aliquot of the supernatant was performed to prevent column overloading for these analytes. A QC sample was prepared by pooling 25 µL aliquots of all samples. Three biological replicates were used for each time point and were each analysed in triplicate.

2.3.5 **Liquid chromatography-mass spectrometry**

LC-MS analyses were performed using a Thermo Finnigan LCQ deca XP plus ion trap mass spectrometer, fitted with a Thermo Finnigan orthogonal electrospray interface, coupled with a Surveyor HPLC system (Thermo Finnigan, San Jose, CA, USA). Chromatographic separation was carried out using a Thermo Scientific Hypercarb™ PGC column (5 µm, 100 mm x 4.6 mm; Thermo Finnigan, Runcorn, UK) at a flow rate of 600 µL min^{-1}. The plant extract sample injection volume was 10 µL, whilst the standard calibrant injection volume was 20 µL. The binary mobile phase system consisted of (A) water modified with 0.1% (v/v) formic acid and (B) acetonitrile modified with 0.1% (v/v) formic acid. The gradient elution profile, modified from Antonio *et al*. (Antonio *et al*., 2008b), was as follows: t = 0-5 min 1-4% B, t = 5-7 min 4-25% B, held at 25% B for 3 min, t = 10-12 min 25-50% B, held at 50% B for 4 min, t = 16-18 min 50-1% B, maintained for 10 min.

The ion trap mass spectrometer was operated in the negative ion mode with the following ionisation conditions: ion source voltage set to 3 kV; capillary voltage -20 V; tube lens offset -60 V; capillary temperature 300 ^{o}C; sheath gas 40 (arbitrary units); auxiliary gas 30 (arbitrary units) and mass range *m/z* 50 – 2000.

2.3.6 **Data analysis**

Paired two-tail t-tests were performed using the "TTEST" Autosum function in Microsoft Excel (Microsoft Office 2007). Results were deemed statistically significant were $p < 0.05$.

2.4 Results and Discussion

2.4.1 **Method development**

The separation of mono-, di-, and oligosaccharides on PGC columns has been reported by several groups to be successful employing a mobile phase system composed of acetonitrile and water ((Koizumi, 1996), (Robinson *et al*., 2007), (Antonio *et al*., 2008b)). The mobile phase system used by Antonio *et al.*was chosen to use for the targeted analysis of carbohydrates in *Haberlea,* as it had been developed to separate similar carbohydrates for quantitation in the drought resistant legume crop *Lupinus albus*. The system was tested using a range of water soluble sugar and sugar alcohol standards that are known osmolytes which are influenced by plant water deficiency: neutral sugars glucose (Glc), fructose (Fru), sucrose (Suc), raffinose, stachyose, verbascose, the sugar alcohols, sorbitol, mannitol, maltitol and galactinol as well as cyclohexyl alcohol inositol.

The individual standards were injected onto the PGC column and their retention times were recorded (Table 2.1). In all cases the compounds were detected in negative ion mode as formylated molecules $[M+HCOO]^-$ using electrospray ion trap mass spectrometry. Using the same chromatographic conditions as Antonio et al. (Antonio *et al*., 2008b) co-elution was observed for the Fru/Glc and mannitol/sorbitol structural isomer pairs (see $t_{R(\mathrm{Antonio})}$ Table 2.1). In order to rectify this, the equilibrating conditions were reduced from 4 % organic solvent (acetonitrile + 0.1 % formic acid) to 1 % organic followed by a shallow gradient of 1-4 % organic over the first five minutes, in an attempt to improve resolution of these isomer pairs; the resulting retention times are tabulated in Table 2.1 ($t_{R(\mathrm{Adapted})}$). The mannitol/sorbitol isomeric pair showed improved resolution under the adapted conditions, whilst peaks associated with the anomeric isomers of Fru and Glc were observed (Figure 2.1).

Figure 2.1 shows the overlap which occurs between one of the anomers of Fru and Glc resulting in what appears as a triple peak when these carbohydrates are injected together. With limited scope to improve resolution further, the peak at ca. 2.8 min was chosen to quantitate Fru and the peak at ca. 3.3 min chosen for Glc. During an initial screen of the *H. rhodopensis* samples it was found that the levels of inositol were too low to be detected, whilst mannitol and sorbitol coeluted to an extent that accurate quantification was not possible, so that these sugars were not targeted for further quantitation.

Standard Compound	Diagnostic ion / *m/z*	$^{a}t_{R(\text{Antonio})}$ / min	$^{b}t_{R(\text{Adapted})}$ / min
Fru	225 $[M+HCOO]^-$	2.60	2.80/3.12
Glc	225 $[M+HCOO]^-$	2.64	3.04/3.28
Inositol	225 $[M+HCOO]^-$	ND	2.41
Mannitol	227 $[M+HCOO]^-$	2.56	2.89
Sorbitol	227 $[M+HCOO]^-$	2.58	3.15
Galactinol	387 $[M+HCOO]^-$	4.34	8.80
Suc	387 $[M+HCOO]^-$	6.58	9.23
Maltitol	389 $[M+HCOO]^-$	5.52	9.07
Raffinose	549 $[M+HCOO]^-$	9.34	9.77
Stachyose	711 $[M+HCOO]^-$	9.28	9.69
Verbascose	873 $[M+HCOO]^-$	9.39	9.77

Table 2.1: Nominal *m/z* and retention time values for standard sugars and sugar alcohols analysed by LC-MS using: [a] gradient reported by Antonio *et al*. (Antonio *et al*., 2008b) and [b] gradient adapted to enhance isomeric pair separation. Entries with two values represent the peak maxima values of an anomeric pair.

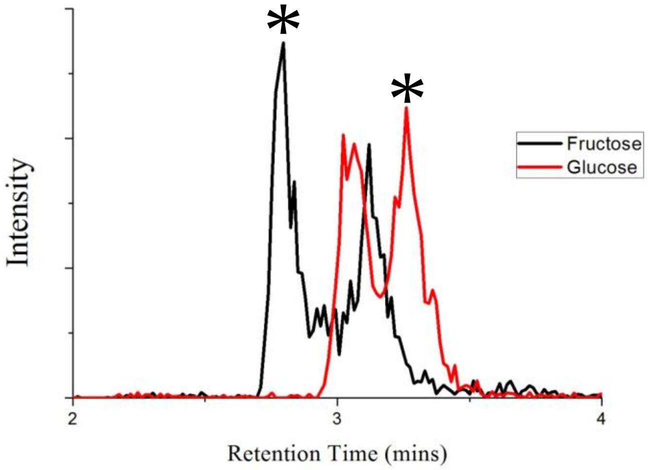

Figure 2.1: Extracted ion chromatogram of Fru and Glc under adapted LC-MS conditions showing the anomeric separation attained using the adapted gradient. The * indicates the peaks used to quantitate Fru and Glc.

2.4.2 **Linearity and repeatability**

The potential for the adapted method to be used for quantitative analysis of the targeted carbohydrates from the leaf blade tissue of *H. rhodopensis* was evaluated by testing the intra- and inter-day repeatability of retention times and the linearity of response of the calibration standards for the remaining targeted analytes.

Intra-day retention time repeatability was determined by analysing the same standard solution three times in a single day. Inter-day retention time repeatability was determined by analysing the same standard solution twice a day over three consecutive days. The relative standard deviation (RSD) values for the targeted analytes were within acceptable limits (< 2 % RSD) for both intra-day and inter-day repeatability (Table 2.2).

Standard Compound	Diagnostic ion /*m/z*	t_R /min	$^a t_R$ (intra RSD) /% (n = 3)	$^b t_R$ (inter RSD) /% (n = 3)	$^c R^2$
Fru	225 $[M + HCOO]^-$	2.75	0.42	0.79	0.9814
Glc	225 $[M + HCOO]^-$	3.40	0.17	1.49	0.9859
Galactinol	387 $[M + HCOO]^-$	8.93	0.45	0.32	0.9914
Suc	387 $[M + HCOO]^-$	9.29	0.19	0.19	0.9640
Raffinose	549 $[M + HCOO]^-$	9.83	0.06	0.13	0.9886
Stachyose	711 $[M + HCOO]^-$	9.75	0.18	0.20	0.9821
Verbascose	873 $[M + HCOO]^-$	9.85	0.29	0.21	0.9978

a = Intra-day RSD of retention times (n = 3 independent measurements); *b* = Inter-day RSD of retention times (n = 3 independent measurements); *c* = Correlation coefficients for the standard curves (eight points) of relative intensities of relativepeak areas against concentration (0-110 µM).

Table 2.2: Nominal *m/z* and retention times, intra- and inter-day repeatabilities of retention times and linearity of calibration curves obtained for standard sugars and sugar alcohols using negative ion PGC-LC-ESI-QIT-MS.

Linearity of response for the standard carbohydrates was determined by plotting integrated peak area versus concentration in the range 0-110 µM. Six-point standard curves were plotted with each point the mean value of three independent measurements obtained using the adapted gradient. The adapted gradient gave values with good linearity of response over the range 0-110 µM for the targeted analytes, with correlation coefficients $R^2 > 0.96$ (Table 2.2).

2.4.3 Targeted PGC-LC-ESI-QIT-MS analysis of water soluble carbohydrates from *H. rhodopensis* leaf blade extracts

The adapted on-line PGC-LC-ESI-QIT-MS method was applied to the separation and identification of seven targeted water soluble carbohydrates (Fru, Glc, galactinol, Suc, raffinose, stachyose and verbascose) for quantitation in leaf blade extracts of the resurrection plant *H. rhodopensis* which had been subjected to water deficit (WD). This work was performed as part of a multi-omics collaboration set up to study the molecular mechanisms which lead to WD tolerance in *H. rhodopensis*. The collaboration was coordinated by Dr Tsanko Gechev and Maria Benina at the University of Plovdiv, Bulgaria.

Figure 2.2 shows photographs of *H. rhodopensis* plants taken at four time-points: control (collected from plants for which watering was maintained throughout the study); 4-day WD (a mild stress treatment in which water had been withheld from the plants for 4 days); 20-day WD (a severe desiccation treatment, with samples collected from plants from which water had been withheld for 20 days); rehydration (samples obtained from plants which were rewatered and had returned to the relative water content of control plants circa 4 days after rewatering commenced). The photographs give insights into the physical changes that *H. rhodopensis* undergoes during WD and makes clear the reason for studying leaf blade samples in this study. At the 4-day WD time-point, leaves begin to wilt (Figure 2.2B) and by 20-day WD the leaves have shrunk and rolled up (Figure 2.2C). After just four days of rehydration, the plant appears, physically, indistinguishable from the control plant (Figure 2.2D). The dramatic changes that the leaf blade undergoes during WD, as well as being the site of biochemical reactions, makes understanding the biochemistry and mechanisms of this organ vital in order to understand the overall picture regarding the ability of resurrection plants to survive severe water deficit.

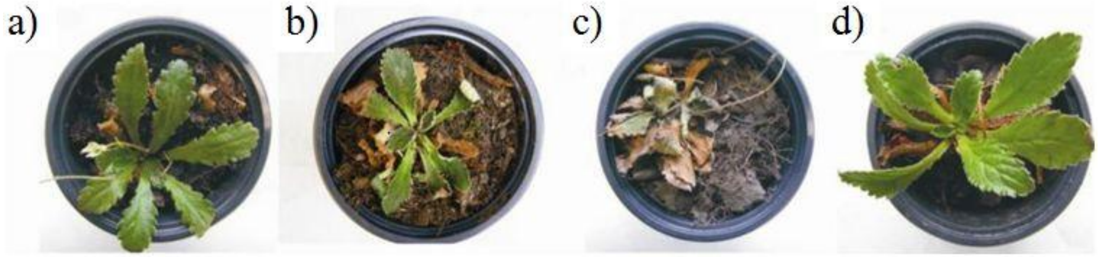

Figure 2.2: *Haberlea rhodopensis* under control conditions (a), 4-day WD (mild stress) (b), 20-day WD (severe desiccation) (c), and after rehydration (d). Reproduced with permission from Gechev *et al*., 2013

Figure 2.3 shows representative overlaid extracted ion chromatograms for each quantified carbohydrate at each of the four time-points. Due to the scale of sucrose and raffinose in contrast to glucose and fructose, the region of the chromatogram between two and four minutes, corresponding to the point of elution for these monosaccharides, has been enlarged inset. The key features observed in the chromatography are the marked decline in peak intensity of the monosaccharides glucose and fructose at the mild stress (4-Day WD) stage as well as the peak intensity rise of sucrose after the onset of WD. A clear drop in peak intensity is also noted for sucrose after rehydration.

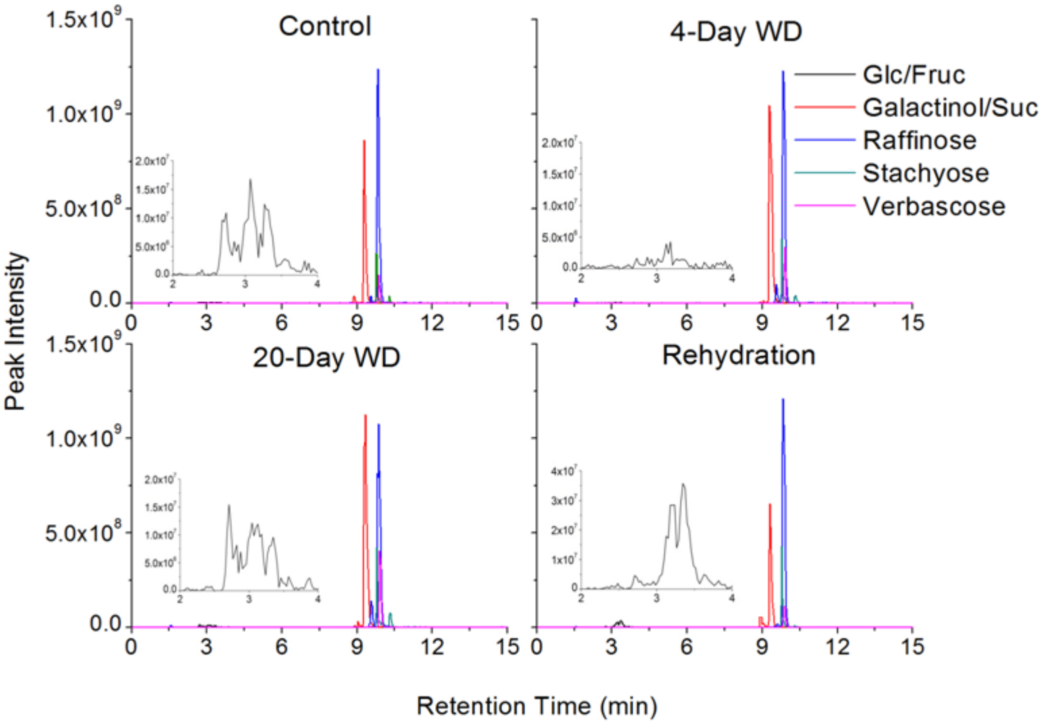

Figure 2.3: Representative extracted ion chromatograms of the seven carbohydrates analysed from metabolite extracts of *H. rhodopensis* at four experimental time-points.

Figure 2.4 shows the carbohydrate quantitation results obtained using the PGC-LC-ESI-QIT-MS method for the *H. rhodopensis* leaf blade extracts. Three biological replicates were generated for each of the four time-points and were each analysed in triplicate. The results are given as a weight-per-weight percentage (w/w %) of each carbohydrate based on the dry weight of the extracted sample. Pairwise t-tests were performed on the data to determine whether a change in w/w % between two time-points was statistically significant, the data pairs tested were; control - 4-Day WD, 4-Day WD - 20-Day WD 20-Day WD - Rehydration. Where the w/w % difference between two time-points is statistically significant it is marked with a star in Figure 2.4.

Relative water content (RWC) values were used to convert the quantified values of each carbohydrate to a dry weight basis as has been previously adopted for metabolite quantitation studies involving *H. rhodopensis* (Müller *et al*., 1997; Djilianov *et al*., 2011). The relative water content (RWC) was determined for each plant sample and found to be 72 %, 42 %, 4 % and 72 % for the control, 4-day WD, 20-day WD and rehydration samples respectively (Gechev *et al*., 2013).

The levels of the monosaccharides Fru and Glc in *H. rhodopensis* show a sharp decline at the imposition of mild WD stress with quantities dropping by ca. 95 % (0.046 w/w % down to 0.003 w/w %) and 92 % (0.033 w/w % down to 0.003 w/w %) respectively. This trend was also observed by Müller *et al*. (Müller *et al*., 1997) and Djilianov *et al*. (Djilianov *et al*., 2011) for *H. rhodopensis* under desiccation conditions and has also been reported in other resurrection plants including *Xerophyta viscosa* (Whittaker *et al*., 2001), *Ramonda nathaliae* (Müller *et al*., 1997) and *Craterostigma wilmsii* (Farrant *et al*., 2007). The results are also consistent with the reduction in chromatogram peak intensity observed for these monosaccharides during WD as shown in Figure 2.3.

The main proposed reason for the drop in Fru and Glc levels is that these monosaccharides are being used in the synthesis of sucrose. There is a literature precedent for this, where results by Whittaker *et al*. (Whittaker *et al*. 2001) reported that sucrose levels rose in *Xerophyta viscosa* leaf tissue at low RWC levels correlated well with the decline in levels of Fru and Glc.

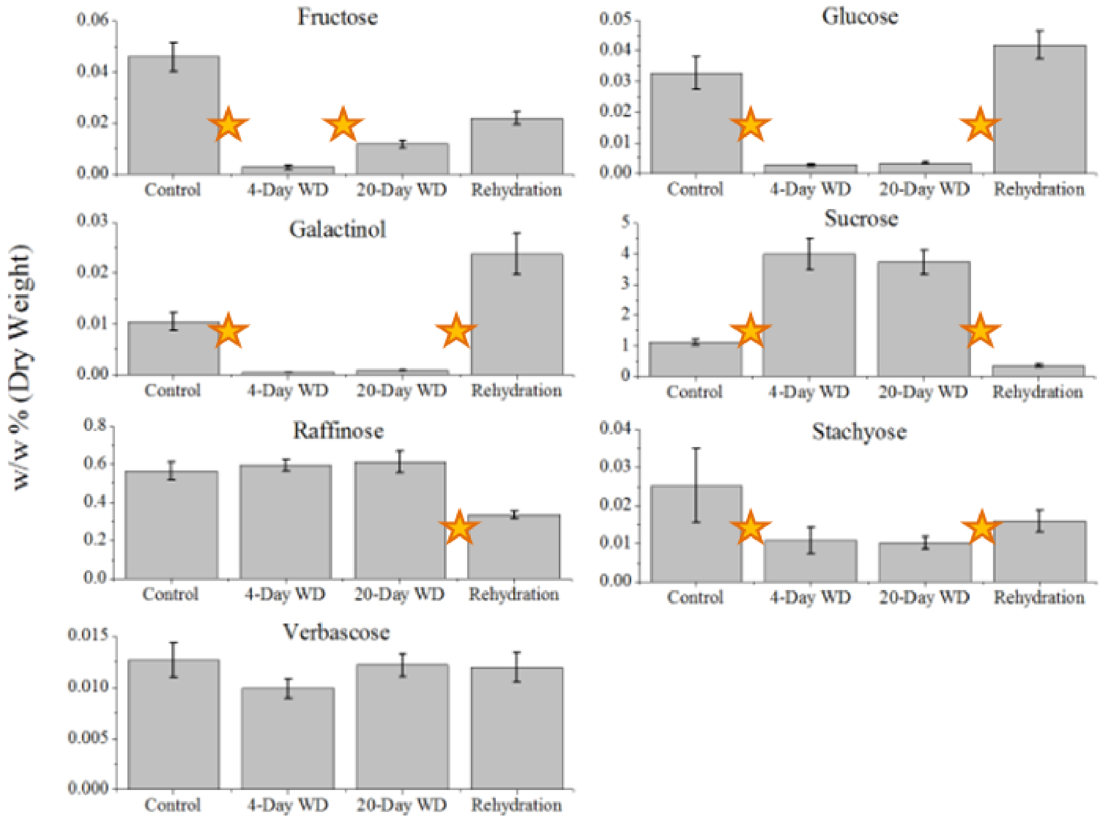

Figure 2.4: Weight-per-weight percentages (w/w %, based on dry weight of samples) of the seven targeted carbohydrates in *H. rhodopensis* leaf blade tissue extracts determined by PGC-LC-ESI-QIT-MS. The four time points are control (Relative water content (RWC) = 72%)), 4-day water deficit (WD)(mild stress, RWC = 42 %) 20-day WD (severe desiccation, RWC = 4 %)) and rehydrated (where RWC returns to control levels, 4 days after rewatering). Data are mean ± SD of three technical replicates from three biological replicates. Paired t-tests were performed on w/w % values between two time-points at the $p < 0.05$ significance limit. The ★ symbol shows differences which were found to be statistically significant.

In this study, the level of sucrose rose almost four-fold during WD. This result for sucrose is a common observation made in drought tolerant plant systems, not limited to resurrection plants, which experience WD (Ghasempour *et al*., 1998; Antonio *et al*., 2007; Farrant *et al*., 2007). This result again correlates well with what is observed in the chromatography, where the sucrose peak intensity rose during WD

The increase in sucrose levels correlated well with the reported upregulation of genes encoding several sucrose synthases, a sucrose transporter and a sucrose responsive element-binding protein in this plant system. It was also noted that hexokinase activity was upregulated at low RWC levels (Gechev *et al.*, 2013). Hexokinase catalyses the conversion of hexoses, like Glc and (albeit at a lower efficiency) Fru, to hexose monophosphates using adenosine triphosphate (ATP) as a phosphate donor (Scharrenberger, 1990). Fru-6-phosphate is a key molecule in the sucrose synthesis pathway, whilst hexokinase conversion of Glc to Glc-6-phosphate is the initial step in the glycolysis pathway. Glycolysis converts Glc to pyruvate and the free energy released is used in the energy-intensive synthesis of ATP and nicotinamide adenine dinucleotide (a biological reducing agent).

Sucrose itself primarily acts as an osmoprotectant, replacing water molecules in the hydration shell of the cell membrane that is lost during WD, thus preventing the fusion of phospholipid molecules to each other which would cause severe membrane damage (Hoekstra *et al.*, 2001). Indeed, sucrose is also believed to play a prominent role in the formation of stable intracellular glasses during dehydration which form from vitrification of cell cytoplasm during desiccation. These glasses protect the cell by maintaining the disorder and physical properties of the general liquid state. In contrast, the lack of a glassy state in the cytoplasm would lead to conformational change proteins and crystallization of chemical compounds embedded in the cell,ultimately leading to cell death (Hoekstra *et al*., 2001).

The level of the sugar alcohol galactinol follows the trend of Fru and Glc and drops by ca. 95 % (0.0104 w/w % down to 0.0005 w/w %) upon mild WD stress. This result follows that observed by Müller *et al*. for *H. rhodopensis*, (Müller *et al*., 1997). Galactinol is used in the synthesis of raffinose-family oligosaccharides (RFOs), whilst Nishizawa *et al*. have reported that galactinol may also work as a hydroxy radical scavenger alongside RFOs in periods of stress (Nishizawa *et al*., 2008). This trend appears to be in contrast to the genomics data for these samples reported by Gechev *et al*. which showed strong upregulation of the mRNA for galactinol synthase during WD (Gechev *et al*., 2013). The difference can be explained by the weak correlation between levels of mRNA and the expressed protein. Although the mechanistical understanding of protein generation seems straightforward, whereby genes are transcribed into mRNA which is sequentially translated to amino acid chains which fold into the functional protein, it has been reported that only ~40 % of variation in protein concentration can be attributed to mRNA abundance (de Sousa Abreu *et al*., 2009; Maier *et al*., 2009). The sources which contribute to this variation in protein abundance are the relative rates of post-transcriptional, translational and protein degradation regulation, as well as cell-to-cell variation in protein expression levels (also know as biological "noise")(Blake *et al*., 2003; Vogel and Marcotte, 2012).

RFOs, α-galactosyl derivatives of sucrose, have been associated with the reduction of oxidative damage to the cell by acting as ROS scavengers (Nishizawa *et al*., 2008). In addition, raffinose and stachyose have been reported to prevent the crystallization of sucrose as it protects the lipid membrane (Caffrey *et al*., 1988). The trends of the three RFOs raffinose, stachyose and verbascose were observed to differ from each other during WD. Raffinose showed no statistically significant change in quantity during WD although levels did drop slightly during rehydration. Stachyose levels dropped by ca. 60 % (0.0251 w/w % down to 0.0109 w/w %) during early stress and remained low throughout WD before recovering slightly during rehydration. The level of verbascose was observed to drop during mild WD stress this had recovered by the 20-day WD desiccation time-point. The result for raffinose differs from that reported by Djilianov *et al*., who observed a two-fold rise in the levels of raffinose in *H. rhodopensis* during WD, and Müller *et al*. who reported that raffinose levels in *H. rhodopensis*, as well as the other European angiosperm resurrection plant species *Ramonda nathaliae* and *Ramonda myconi*, decreased during WD (Müller *et al*., 1997; Djilianov *et al*., 2011). The trend for raffinose may be debatable in *H. rhodopensis* but in general the level of this carbohydrate in WD tolerant plants has been observed to increase during stress (Ghasempour *et al*., 1998; Farrant *et al*., 2007).

The reduction in stachyose content during WD does not correspond to the results reported by Ghasempour *et al*. (Ghasempour *et al*., 1998) who observed a general accumulation of this RFO in WD tolerant plants under stress. The result for stachyose is unexpected when taking into account that the genomics data reported by Gechev *et al*. (Gechev *et al*., 2013), which shows upregulation of a stachyose synthase enzyme during stress. There is no current literature on how verbascose levels are affected by WD, but considering it is a member of the RFOs it may be that levels are maintained to maintain the levels of ROS scavengers in the leaf blade. The fact that the levels of verbascose have returned to control levels at the severe desiccation, 20-day WD time-point after a drop during mild WD stress may be explained if some of the stachyose has been used in the synthesis of verbascose.

2.5 Conclusions

The aim of the study in this chapter was to analyse the progressive effects of drought stress on leaf blade tissues of *H. rhodopensis*.A PGC-LC-ESI-QIT-MS method was developed and used in the targeted analysis of carbohydrates extracted from leaf blade samples of *H.rhodopensis* subjected to control, mild WD, severe WD and rehydration. The method provided good linearity and separation of seven target molecules, including the structural isomers Fru and Glc. The data was collected and reported as part of a multi-omics collaboration coordinated by the University of Plovdiv, Bulgaria.

In this study the levels of Fru, Glc and galactinol were found to drop heavily in the leaf blade tissue during WD; this is believed to be due to their assimilation into larger carbohydrates (e.g. sucrose or RFOs).The level of the osmolyte sucrose increased four-fold throughout the imposition of stress in agreement with the upregulation of several sucrose synthase and sucrose transporter genes. The levels of the RFOs were conserved whilst stachyose levels reduced during WD. The general maintenance of RFOs is thought to ensure that role of ROS scavenging is conserved throught WD.

Chapter 3

Untargeted LC-MS analysis of water soluble metabolites in the plant model systems *Arabidopsis thaliana* and *Thellungiella salsuginea*

3.1 Introduction

Arabidopsis thaliana (thale cress) is a small flowering plant distributed throughout Europe, Asia and North America, and is a member of the mustard (Brassicaceae) family. *A. thaliana* was the first plant to have its complete genome sequenced (five chromosome pairs of around 120 Megabases (Mb) in total) and has since become a key model system for plant genome analysis. The small genome (in comparison to crop plants like rice (389 Mb - International Rice Genome Sequencing Project, 2005) or tomato (ca. 950 Mb - The Tomato Genome Consortium, 2012)) is an important attribute, which facilitates its study to enhance our understanding of differences at the genetic level between various plant systems and provide a foundation for the detailed functional characterisation of plant genes. *A. thaliana* has several advantages as a model plant system, including high fecundity, small size and short life cycle (reducing space and time requirements), as well as the ability to be transformed at the genetic level to generate *A. thaliana* gene knockouts (mutants), functional genomics studies, and for reverse genetic screening, where a DNA sequence is identified for study and plant lines with mutations within that gene sequence are sought (Meinke *et al*., 1998; Arabidopsis Genome Initiative, 2000; Bent, 2000; Bressan *et al*., 2001).

One of the limitations of *A. thaliana* is its intolerance to extended periods of exposure to harsh climates, including drought, cold and highly saline conditions. Crop plants too are generally sensitive to these conditions, and with the increasing global population and crop farming being pushed to expand into marginal lands where these conditions are more prevalent, a model plant system which retains the assets of the *A. thaliana* model but is also tolerant to these stresses has been required. *Thellungiella salsuginea* (synonymous with *T. halophila* (salt cress)) is a halophytic plant (i.e. grows in areas of high salinity), with the ability to grow well in other adverse conditions and, in addition, is a close relative of *A. thaliana* (>90 % nucleotide identity in cDNA sequences) although possessing a genome approximately twice the size (Al-Shehbaz *et al*., 1999; Bressan *et al*., 2001; Zhu, 2001; Amtmann *et al*., 2005; Amtmann, 2009). *T. salsuginea* is able to readily undergo transformations in the same way as *A. thaliana*, so that mutants can be produced and systematically analysed to discover the salt tolerance genes and pathways operating in this plant system. Direct studies, analysing differences in the genomes of *A. thaliana* and *T. salsuginea* using '-omics' approaches, is an important tool in our understanding of extremophile plant biology for exploitation in improving crop performance on these marginal lands (Zhu, 2001; Inan *et al*., 2004; Amtmann, 2009).

Untargeted metabolomics involves the use of analytical methods to acquire data on a wide range of metabolite classes, of which (as opposed to a targeted approach) prior knowledge may be limited. Depending on the sample extraction protocols used, the metabolite pool present in a complex biological matrix could number into the thousands, leading to a high number of detectable features per sample and subsequently large datasets in which key differences may be overlooked due to the scale of data available. Multi-variate statistical techniques, used in an unbiased manner, help to focus the study of a dataset in order to draw out trends and identify the key discriminating features (analytes) which are responsible for these trends. In metabolomics, dataset trends commonly arise from the up- or down-regulation of metabolites in response to external or internal stimuli (Cubbon *et al*., 2007; Pinheiro *et al*., 2011; Viant and Sommer, 2013).

MS-based approaches to untargeted metabolomics have grown in interest over recent years owing to the high sensitivity achievable (Viant and Sommer, 2013). This rise has been complemented by the broad range of instrumentation available, including separation techniques (e.g. LC, GC and GC x GC), ion sources (of which ESI and electron ionisation (EI) are currently the most commonly used) and mass analysers (e.g. ion trap, time-of-flight (TOF), quadrupole-TOF (QTOF), triple quadrupole (QQQ), orbitrap and Fourier transform ion cyclotron resonance (FT-ICR) detectors). Combinations of these techniques mean that almost complete coverage of diverse metabolite classes can be attained from small non-polar hydrocarbons up to large, highly polar molecules such as oligosaccharides and flavonoids (Kind and Fiehn, 2010; Patti, 2011).

The chemical and structural identification of metabolites is seen as a major bottleneck in untargeted metabolomics studies, owing to the wide variety of metabolite types and the range of structural isomers that are present in biological systems (Dunn *et al.*, 2011). In addition, the benefits of accurate *m/z* determination, isotope distribution and elemental composition provided by MS are countered somewhat by the 'soft' ionisation techniques commonly favoured in metabolomics studies which provide limited structural information. Where further identification of a molecular species is required, dissociation (e.g. using collision induced dissociation) can be performed to generate fragment ions. The use of tandem (MS^2) and multiple-stage (MS^n) mass spectrometric techniques enables the recording of this fragmentation data and connecting it to the species from which it came, which, when used in conjunction with databases, can enable potential feature identification (Kind and Fiehn, 2010).

There are in the literature a few examples of direct comparisons of the effects of abiotic stress on the plant genera *Arabidopsis* and *Thellungiella*. For example, Pang *et al*. described a comparative proteomics study of *A. thaliana* and *T. halophila* under salt stress conditions. They found that under stress, *T. halophila* expressed proteins involved in more diverse roles than *A. thaliana* (including protein synthesis, hormone and amino acid metabolism, ROS scavenging and cell wall modifications) leading to a larger number of processes working cooperatively to re-establish plant cell homeostasis (Pang *et al*., 2010). In 2012, Lee *et al*. studied the relative freeze tolerances (determined by electrolyte leakage assays and targeted metabolomics) of several *Arabidopsis* and *Thellungiella* accessions. They reported that some *Thellungiella* accessions were found to tolerate far lower temperatures than any *Arabidopsis* accessions, and indicated that the metabolic adaptation strategies adopted by the two genera were different (Lee *et al*., 2012). However, the author is unaware of studies in the literature comparing the effects of drought stress on the metabolomes of *Arabidopsis* and *Thellungiella*.

3.2 Aim

The work described in this chapter is part of a collaborative project carried out with Dr. Carla Pinheiro of the Instituto de Tecnologia Química e Biológica (ITQB), Lisbon, Portugal and Dr Julie Wilson of the York Centre for Complex Systems Analysis (YCCSA), York, UK.

The aim of the study in this chapter was to analyse the progressive effects of drought stress on leaf blade tissues of *A. thaliana* and *T. salsuginea*. After rewatering, samples of soluble metabolites extracted from plants in early- and late-drought stress conditions were analysed by PGC-UHR-Q-TOF-MS and untargeted multi-variate statistical analysis of the collected datasets was performed. Key features related to drought tolerance in these plant systems were identified and direct infusion MS^2 and MS^n strategies used to gain fragmentation data of the corresponding masses for potential structural identification. The general aims of the work in this chapter are summarised as follows:

- Collect datasets from water-soluble metabolite fractions of drought-stressed leaf blade tissue samples of *A. thaliana* and *T. salsuginea* using PGC-UHR-Q-TOF-MS.
- Perform untargeted, unbiased multivariate and univariate statistical analyses on the collected datasets.
- Highlight key discriminatory features from the dataset, which contribute to the response mechanism of the plant models.
- Isolate and collect fragmentation data by direct infusion FT-ICR-MS using MS^2 and MS^n strategies.
- Elucidate potential identifications based on available literature and metabolite databases.

3.3 Experimental

3.3.1 Plant material and experimental conditions

All plant sample preparation and collection were performed by Dr. Carla Pinheiro of the Instituto de Tecnologia Química e Biológica (ITQB), Lisbon, Portugal. *Arabidopsis thaliana* and *Thellungiella salsuginea* seeds were soaked and stratified at 4 ºC for 4 or 14 days respectively. Seeds were then transferred to pots containing a mixture of coarse sand and peat (Shamrock). Plants were grown in controlled conditions, under a 12 h photoperiod, with temperatures ranging from 20 to 24 °C, with 60-70 % relative humidity and photosynthetically active radiation of 240 μmol m^{-2} s^{-1} (average). Plants were watered every day with demineralized water to yield 85 % soil relative water content. The stress treatments started when most plants had 8 to

10 fully developed leaves (40 days for *T. salsuginea* and 36 days for *A. thaliana*). For the drought stress treatment, water was withheld until the soil relative water content decreased to 10 %; on rewatering, plants were allowed to recover for one day. Soil relative water content was monitored daily, soil relative water content being defined as [(pot weight - weight of the pot with totally dried peat)]/[(pot weight at field capacity - weight of the pot with totally dried peat)] x 100. Plants were harvested at day 0 (last day of watering) and when the soil relative water content in the drought treated pots reached 75% (day 1), 66% (day 3), 45% (day 5), 12% (day 12) and after stress recovery (day 13). The number of leaves per rosette was registered and the shoots were frozen in liquid nitrogen and kept at -80 °C until further analysis.

3.3.2 Extraction of water-soluble carbohydrates

Water-soluble carbohydrates were extracted from *A. thaliana* and *T. salsuginea* rosettes following the chloroform/methanol method (Antonio *et al*., 2008). Briefly, 50 mg of freeze-dried leaf material was ground in liquid nitrogen and extracted with 250 μL ice-cold chloroform:methanol (3:7, v/v), vortex-mixed and incubated for 2 h at –20 ˚C. After incubation, samples were extracted twice with ice-cold water and, after centrifugation at 17,900 *g* at 4 ºC for 10 min, the upper phases were collected and pooled. The combined supernatants containing the water-soluble carbohydrates were evaporated to dryness using a centrifugal concentrator (Savant Speed Vac Plus SC110A, Thermo Electron Corporation, Runcorn, UK). All samples were shipped as dried extracts and reconstituted with 500 µL deionised water and centrifuged at 6800 *g* at 20 °C for 30 min followed by a further 50-fold dilution of small aliquots (10 μL) in deionised water to prevent signal saturation and to minimise matrix effects, followed by liquid chromatography ion trap mass spectrometry (LC-MS) analysis.

3.3.3 Data collection

Leaf blade samples of both *A. thaliana* and *T. salsuginea* were collected at six time-points during the drought stress study: day 0; day 1; day 3; day 5; day 12 and day 13, referring to the number of days that water was withheld from the plant. Samples taken at days 0-5 were termed 'early-stress' samples whilst samples taken at day 12 and day 13 were termed 'late-stress' samples. The watering program for control plants was maintained throughout the experiment. Six biological replicates and six controls for each time-point were analyzed, except for day 1 control samples where only five biological replicates were provided. The samples from the two different plants were run in separate LC-MS runs. Before each LC-MS run, the system was equilibrated using sequential injection of 15 quality control (QC) standards made up of a pool of equal sized aliquots of each sample. The samples were randomized by giving each sample a number with the run order determined using an online random sequence generator (http://www.random.org/sequences/). The samples were run in batches of eight or nine, interspersed by a QC sample. Each individual sample or QC injection was separated by water blank injections. The use of QC standards in this work is analogous to that described previously (Michopoulos *et al*., 2009 and Dunn *et al*., 2012)

3.3.4 Liquid chromatography-mass spectrometry conditions

LC-MS analyses were performed on a Dionex U3000 2D HPLC system coupled to a Bruker maXis UHR-Q-TOF MS with an ESI interface. Analytes were detected in the negative ion mode using the following MS parameters: capillary voltage, 4500 V; nebulizer gas, 2 Bar; drying gas flow, 8.0 L/min; drying temperature, 200 ^{o}C and using a collision energy offset on the collision cell of -10.0 eV. Mass spectra were acquired over the scan range *m/z* 50-1000. Chromatographic separation was carried out using a PGC Hypercarb^{TM} column (5 µm, 100 mm × 4.6 mm; Thermo Electron, Runcorn, Cheshire, UK) at a flow rate of 600 µL min^{-1}. The sample injection volume was 20 µL and the PGC column was used at ambient temperature (25 ^{o}C). The binary mobile phase was composed of (A) water modified with 0.1% (v/v) formic acid (FA) and (B) acetonitrile modified with 0.1% FA. The gradient elution was as follows: 0-4 min maintained at 2% B; 4-7 min, 2 to 8% B; 7-10 min 8-25% B and maintained for 3 min, followed by column regeneration and re-equilibration: 13-19 min, 25 to 40% B; 19-19.5 min, 40 to 50% B held for 1 min; 20.5-21 min 50 to 99% B held for 2 min; 23-25 min 99 to 2% B and maintained for 10 min. All solvents were purchased from Fisher Scientific except formic acid, which was purchased from Sigma Aldrich.

Features corresponding to analytes identified by statistical analysis, were fraction-collected by LC-MS (LC parameters as above), with the LC and MS connected by a flow splitter. Fractions were collected manually in a retention time window which started 0.1 min before peak elution and finished 0.1 min after peak elution (this point was identified by watching the extracted ion chromatogram of the targeted analyte). The collected fractions were then evaporated to dryness using a centrifugal concentrator (Savant Speed Vac Plus SC110A, Thermo Electron Corporation, Runcorn, UK) and resuspended in 100 µL 50:50 water:methanol. Direct infusion MS/MS analysis was performed on a Bruker solariX FT-ICR-MS in negative ion mode with the following MS parameters: capillary voltage, 3800 V; nebulizer gas, 1.2 Bar; drying gas flow, 3.7 L/min and drying temperature 220 ^{o}C. Collision cell parameters: collision gas, argon; gas control setting, 55 % and collision cell pressure read-back 5.4x10^{-6} mbar. Spectra were acquired over the scan range *m/z* 50-1000. Where possible, MS^3 fragmentation of intense MS/MS fragment ions was carried out using sustained off-resonance irradiation collision-induced dissociation (SORI-CID).

3.3.5 Statistical methods

All statistical analysis presented in this chapter was performed by Dr Julie Wilson, YCCSA, York, UK. Full LC-MS datasets were collected for *A. thaliana* and *T. salsuginea* drought-stressed samples. Untargeted multivariate and univariate analyses of the data were performed in order to explore how drought stress altered levels of water-soluble metabolites in the two plant systems over the full time-course of the study. A comparison of the most discriminatory variables identified by the statistical analyses was then made for the two species.

In order to align the chromatograms, *m/z* values were initially truncated to the nearest 0.1 *m/z* unit and the time series (i.e. the retention time window for peak elution) for each *m/z* value was averaged over half minute intervals. Principal Components Analysis (PCA) showed that most of the variance in the data from the two plant species was due to differences in the late-stress samples (days 12 and 13). However, the variance along the second principal component was due to differences between batches. Attempts to correct for inter-batch variation using the QC pool in fact made matters worse due to the strong influence of the late-stress samples, which particularly affect certain variables. The analysis was therefore conducted in two stages. Firstly, the full data were analysed with no QC correction and the variables related to late-stress were identified. The second stage of the analysis was then concerned with the identification of variables showing early-stress differences. The data from the plants sampled under late-stress conditions (days 12 and 13) were therefore removed from the dataset and only data from plants sampled under early-stress conditions and controls were considered. For these data (from early stress plants), the variables were considered in two separate groups: the variables already identified as responsible for late stress differences were labeled "Group A" and all remaining variables were labeled "Group B".

For Group A variables, no QC correction was performed as the presence of day 12 and day 13 extractions in the pools would swamp and thus seriously affect these variables. This subset of variables was analysed to determine whether any of these late-stress variables also showed a response in the early time points. As the variables in Group B were not related to late-stress response, the presence of day 12 and day 13 extractions in the pooled samples was not a problem and QC correction was performed to account for batch differences. As with unit variance-scaling (a technique which ensures all variables have equal potential to influence the statistical model - Keun *et al*., 2003) QC-correction can scale up small variables, including noise, and so the data were denoised prior to QC correction. This was achieved by considering the time series for each *m/z* value and removing those variables with intensities below twice the average for that *m/z* value. The resulting data were analysed to identify any variables showing early-stress response. In both stages of the analysis, PCA, partial least squares discriminant analysis (PLS-DA) and t-tests were performed and variables related to stress response were identified using a combination of the loadings from PCA, VIP scores from PLS-DA and *p* values for t-tests (checking manually for those affected by outliers). Analyses were carried out using software developed in-house using Matlab (Mathworks, 2002). A schematic which summarises the statistical methods and dataset treatment adopted for the LC-MS datasets of both plant species is shown in Figure 3.1.

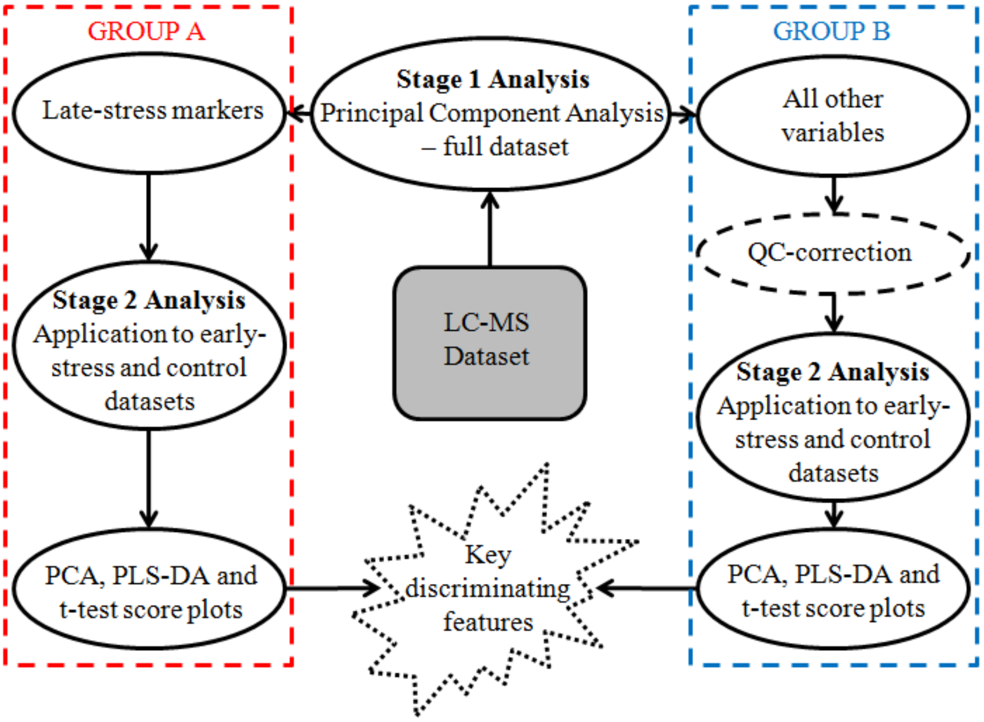

Figure 3.1: A schematic summary of the statistical methods and correctional treatments performed on the LC-MS datasets from *A. thaliana* and *T. salsuginea* in order to determine key discriminating features corresponding to metabolite changes during drought stress.

3.4 Results and discussion

3.4.1 Untargeted LC-MS analysis of water-soluble metabolites

3.4.1.1 Stage 1: Principal components analysis of full scan datasets

A combined, untargeted study of the water-soluble metabolite fractions of *A. thaliana* and *T. salsuginea* leaf blades was performed to pull out the key features that undergo changes as water deficit progresses. Datasets of full scan negative ion mode LC-MS data, collected using a Bruker maXis UHR-Q-TOF MS, were exploited in an unbiased approach using principal components analysis (PCA), a multivariate statistical technique.

PCA was performed separately for the data from each of the two species. The scores plots show a clear separation between the late-stress (days 12 and 13) and the early-stress and control samples for both plants. The groupings were separated along PC1 for the *A. thaliana* and *T. salsuginea* datasets (Fig. 3.2 a and b respectively).

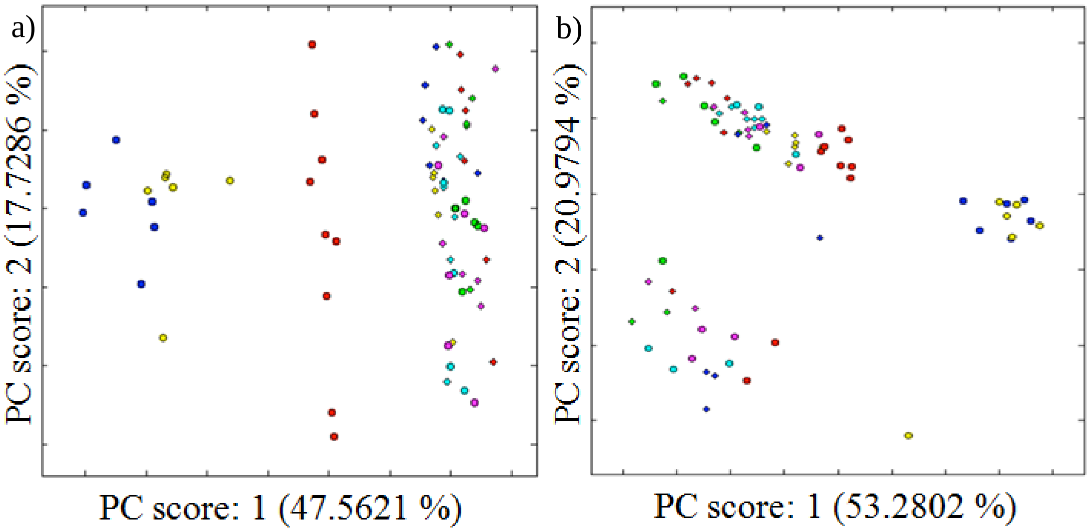

Figure 3.2: Principal components analysis scores plots of a) *A. thaliana* full scan data and b) *T. salsuginea* full scan data. These plots show the separation of late-stress (day 12 and 13, represented by blue (day 12) and yellow (day 13) circles respectively) samples from the rest. QC samples are shown as red circles.

Batch-to-batch variation was observed in the datasets from the two species. Figure 3.3 shows the scores plot for *T. salsuginea* coloured according to batch, highlighting clear differences between batches 7 and 8 and the rest. Batch-to-batch variation is a common issue with large-scale LC-MS analyses, where small analytical changes (e.g. retention time change or reduced mass accuracy), are compounded over time and give rise to block effects (Sangster *et al*., 2007; Draisma *et al*., 2010; Kirwan *et al*., 2013).

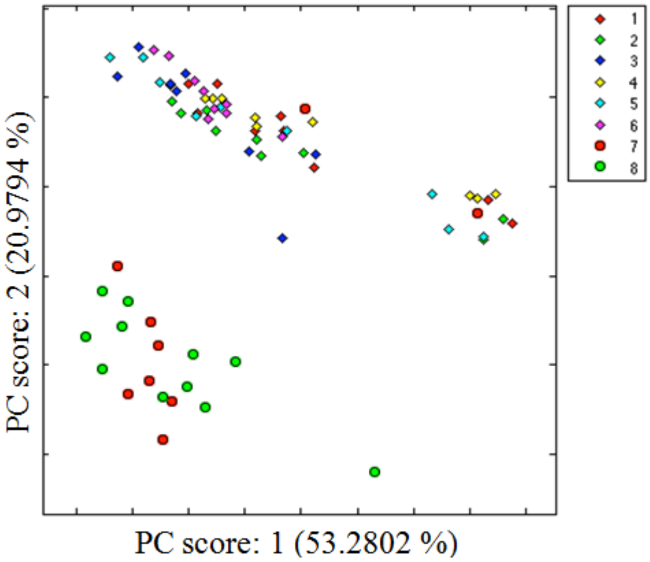

Figure 3.3: PCA scores plot for the first two principal components for *T. salsuginea* samples, coded according to batch.

The initial analysis of the full data for each of the two plant species revealed those variables that could be related to late-stress response. The data from the late-stress time points, i.e. day 12 and day 13, were then removed from the dataset and the data from the early-stress time points and controls were compared. With the late-stress time points removed, inter-batch variation now dominated the variance-based PCA, making identification of early-stress markers difficult. As QC correction of the late-stress markers was adversely affected by the presence of day 12 and day 13 samples in the QC pool, the variables were further considered in two subgroups for examination of the early-stress time points, with the late-stress markers labeled Group A (with no QC correction) and all other variables Group B (on which QC correction was performed).

3.4.1.2 Stage 2 - Group A: PCA of early-stress samples considering late-stress markers

In order to see whether the variables already identified as late-stress markers also showed early-stress response, Group A variables were analysed for signs of early-stress response. No QC correction was performed with these variables. Figures 3.4 a (*T. salsuginea*) and b (*A. thaliana*) show the PCA scores plots obtained. Tendency to group according to stress stage (i.e. days after withholding water) is observed for both plant species. For *T. salsuginea*, progression is observed from the clustering of day 0 and day 1 samples, through the banding of day 3 samples to the clear separation of day 5 samples. For *A. thaliana*, although it could be suggested that day 3 and day 5 samples have separated slightly from the day 0 and day 1 samples, the separation is much less distinct than that observed for *T. salsuginea*. Figures 3.5 (a) (*T. salsuginea*) and (b) (*A. thaliana*) show the intensities of example Group A markers coloured according to stress-state. It can be seen that these late-stress markers also show an early-stress response. Although more than 200 Group A markers were identified for *A. thaliana*, compared to just 65 for *T. salsuginea*, fewer of the Group A markers for *A.thaliana* than for *T. salsuginea* also exhibited a response during early-stress.

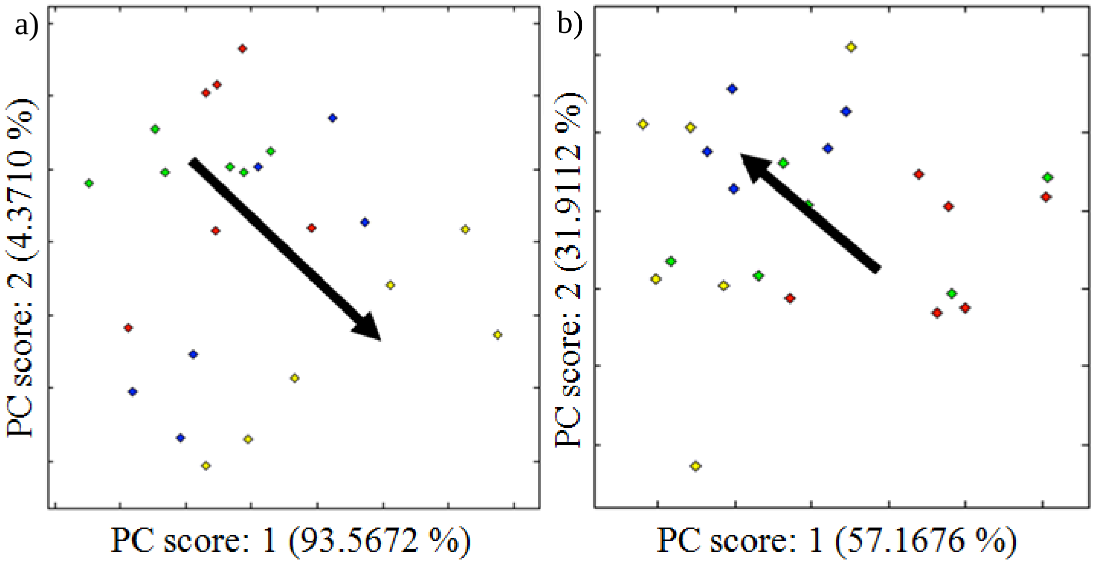

Figure 3.4: PCA scores plots for a) *T. salsuginea* and b) *A. thaliana* early-stress samples considering only Group A markers. The coloured diamonds represent: day 0 (red); day 1 (green); day 3 (blue) and day 5 (yellow) samples. Arrows represent the direction of stress state progression.

These results suggest that *T. salsuginea* initiates a metabolic response to drought stress earlier than *A. thaliana*, which could explain why *T. salsuginea* is able to tolerate much harsher climates than *A. thaliana*. Interestingly, in most cases for both plant species, the variables showing early-stress response were not those exhibiting the greatest late stress response. As the variables showing early-stress response in *A. thaliana* were less convincing (poor separation of the different control and early-stress samples) than those for *T. salsuginea*, they were not considered in further targeted analysis.

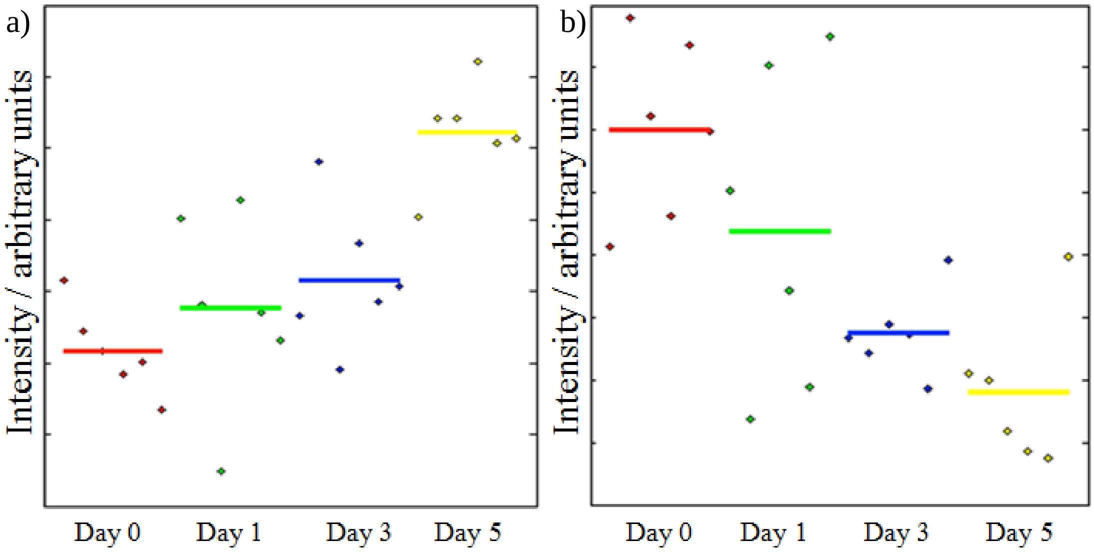

Figure 3.5: Examples of relative intensities for variables in Group A (identified as late-stress markers in the first stage of the analysis) shown for control and early-stress samples (Day 0, red; Day 1, green; Day 3, blue; Day 5, yellow). In (a) the intensity for *m/z* 707.1 at 10.5 minutes for *T. salsuginea* can be seen to increase with increasing stress, whereas in (b) the intensity for *m/z* 405 at 13.5 minutes for *A. thaliana* decreases with increasing stress. The horizontal lines represent the mean of each group.

3.4.1.3 Stage 2 - Group B: PCA of early-stress samples considering all other variables

To determine whether any of the variables that had not already been identified as being involved in late-stress response might still show signs of early-stress response, the Group B variables were also analysed for the early-stress and control samples. After removing the variables identified as late-stress markers (Group A) from the dataset, QC-correction was performed on the remaining variables (Group B). As QC-correction can scale up small variables including noise, the data were first denoised by removing markers with intensities below a fixed threshold; markers less than twice the average intensity within a time series were removed. Figure 3.6 shows PCA scores plots considering only denoised Group B variables for *T. salsuginea* (Fig 3.6 a) and *A. thaliana* (Fig 3.6 b). The plot for T. *salsuginea* again shows some separation of day 5 samples from days 0, 1 and 3 samples, but to a lesser extent than was observed when Group A variables were considered. The plot for *A. thaliana* shows no separation of the early-stress samples. Although an overall trend can be seen in the scores plot for for *T. salsuginea*, no individual Group B variables showed a convincing response to early-stress for either *A. thaliana* or for *T. salsuginea* and Group B variables were not considered further for targeted analysis.

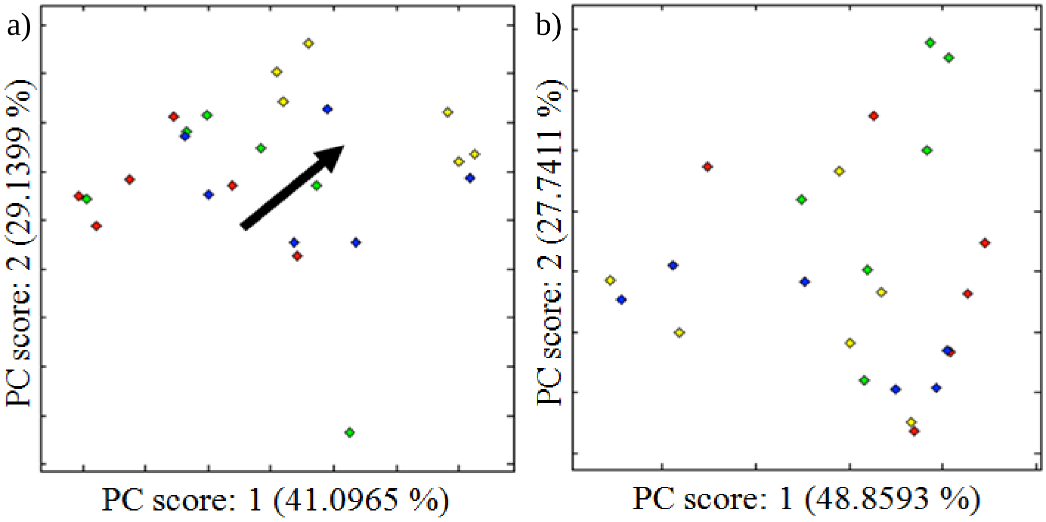

Figure 3.6: PCA scores plots for a) *T. salsuginea* and b) *A. thaliana* of early-stress samples obtained from Group B variables, after denoising. The coloured diamonds represent: day 0 (red); day 1 (green); day 3 (blue) and day 5 (yellow) samples. The arrow represents the direction of stress state progression in *T. salsuginea*.

3.4.2 Key discriminant feature identification using MS^2 and MS^n strategies

In both plant species, Group A markers correspond to those variables able to discriminate late-stress samples from the rest in the first stage of the analysis. In the second stage of the analysis, some of the late-stress markers in Group A were also found to show early-stress response. In addition, some variables from Group B that had not been identified as late-stress markers were identified as showing a response to early-stress in *T. salsuginea*. Each variable represents a chromatogram feature corresponding to an *m/z* bin and retention time window. Three ranking lists of features were prepared, representing *T. salsuginea* early-stress and late-stress and *A. thaliana* late-stress markers. The lists give the ranking of each feature in terms of PCA loadings, PLS-DA loadings, PLS-DA VIP scores and t-test *p*-values. Visual inspection of the extracted ion chromatograms of each feature, plotted using Bruker DataAnalysis software, yielded accurate *m/z* values and allowed isotopic signals to be identified. Features that ranked highly across the three statistical techniques were considered key discriminant features and targeted for identification using MS^2 and MS^n strategies.

The ranked features were dominated by *m/z* bins associated with sucrose (and galactinol for *A. thaliana*) as well as various molecular species for sucrose (i.e. $[M + COOH]^-$, $[2M – 2H + Na]^-$, etc.) and their isotopes. The variety of molecular species of sucrose observed, that indicate the high levels of this carbohydrate in the leaf blade tissue, is not unexpected, as upregulation of sucrose synthesis during drought stress is well known and has been observed in several different drought-resistant and resurrection plant species (*Sporobolus stapfianus* (Whittaker *et al*., 2007), *Lupin albus* (Antonio *et al*., 2008), *Xerophyta viscosa* (Peters *et al*., 2007) and *Haberlea rhodopensis* (Gechev *et al*., 2013)). The carbohydrate raffinose was also identified as its formylated molecule $[M + HCOO]^-$ (*m/z* 549). Both sucrose and raffinose were positively identified based on retention time comparison with authentic standards.

An automated online LC-MS/MS method, carrying out collision induced dissociation in the hexapole collision cell, and exploiting the energy file editor feature of a Bruker solariX FT-ICR-MS was attempted, to collect fragment information for each target feature. The energy file editor works by preparing a collision energy ramp, based on the *m/z* of an analyte, where analytes of higher *m/z* are subjected to higher collision energy in the collision cell to optimise dissociation. However, the automated method yielded few fragments, with many the result of loss of formic acid from formylated molecules. Consequently, fractions were collected manually at the retention time of each feature and directly infused into the mass spectrometer for manual collision induced dissociation (CID)-MS^2 analysis in negative ion mode. The data are summarised in Table 3.1.

Prominent in all three lists were two co-eluting features at *m/z* 191 and *m/z* 405. The feature at *m/z* 191.0197 was assigned as citric acid (accurate mass: 191.0197; error: 0.1 ppm), after comparison of its fragmentation pattern in both METLIN (www.metlin.scripps.edu) and PRIMe (www.prime.psc.riken.jp) metabolomics databases. MS^2 analysis of the feature at *m/z* 405.0236 yielded a single fragment at *m/z* 191.0185 and since the feature co-eluted with citric acid it was tentatively assigned as the $[2M – 2H + Na]^-$ charge-sharing dimer of citric acid (accurate mass: 405.0287; error: 12.6 ppm). Comparing the combined absolute peak intensities of the features at *m/z* 191 and 405 in stressed samples with those in their respective controls, a marginal decline for day 1 and day 3 was observed followed by an increase (above control levels) in day 5 samples. These observations suggest that drought stress is incipient until day 5, when citric acid accumulation becomes apparent. However, by days 12 and 13, citric acid intensities had declined significantly in comparison with controls, an observation that is contradictory to that reported by Urano *et al*. (Urano *et al*., 2009) who reported a rise in citric acid levels during dehydration, albeit for a rapid 15 hour dehydration study as opposed to the slower 13 day dehydration timescale used for this investigation.

A further *T. salsuginea* late-stress feature giving a signal at *m/z* 421.0697 has been tentatively assigned as trehalose-6-phosphate (accurate mass: 421.0753; error: 13.2 ppm). Retention time and fragment ion data correlate well with those reported by Antonio *et al*. (Antonio *et al*., 2007). This feature was upregulated during water deficit, which follows the trend previously reported by Avonce *et al.* (Avonce *et al*., 2004) with trehalose acting as an osmoprotectant, in a role similar to sucrose.

A discriminant feature in *T. salsuginea* early-stress samples, at *m/z* 333.0570, has been assigned as an unidentified monohexosyl glycerol phosphate. The fragment ion at *m/z* 241.0104 corresponds to a neutral loss of 92.0466, potentially a glycerol unit (accurate mass: 92.04734; error: 7.6 ppm). MS^3 analysis of the fragment at *m/z* 241.0104 yielded a fragment at *m/z* 78.9589 that suggests the presence of a phosphate group (accurate mass: 78.9591; error: 2.5 ppm). The neutral mass loss of 162.0516 could be indicative of a hexose unit (accurate mass: 162.0528; error: 7.4 ppm). One potential candidate could be α-D-galactosyl-(1,1')-sn-glycerol-3-phosphate, otherwise known as isofloridoside phosphate. This compound has been reported to play a major role in osmotic regulation of cells in the flagellate *Ochromonas malhamensis* during water loss (Kauss *et al*., 1978).

A key discriminating late-stress feature in *T. salsuginea* at *m/z* 251.1015 was tentatively assigned as a $[2M - 2H + Na]^-$ charge sharing dimer of proline (accurate mass: 251.1013; error: 0.7 ppm). The only fragment ion peak, at *m/z* 114.0557, corresponds to the deprotonated molecule of proline (accurate mass: 114.0561; error: 3.1 ppm). Although attempts were made to obtain MS^3 data on this fragment ion, the intensity of this peak once isolated was too low to generate good fragment data. The feature is upregulated with respect to controls during water deficit, which, if proline, is consistent with observations previously reported (Lugan *et al*., 2010; Krasensky and Jonak, 2012). Proline is an important metabolite in many stress states, including cold stress and salt stress, and is involved in a number of roles including ROS scavenging and acting as a protein protectant (Krasensky and Jonak, 2012). Although the same feature was present in *A. thaliana*, univariate analysis suggested that it was not a discriminating factor during drought stress in that plant, and so was not included for further analysis. It is also noted that a second *T. salsuginea* late stress feature at *m/z* 277.1819 fragmented to give a proline fragment ion at *m/z* 114.0556. However, no further structural assignment for this feature has been made.

T. salsuginea - Group A early-stress features

t_R /min	*m/z*	Putative molecular formula	Direct Infusion Fragment ions / *m/z*	Potential Assignment[a]
1.55	272.9587	-	261.1551, 244.9624, 228.9677, 216.9679	UC
1.55	288.9361	-	260.9398, 244.9450	UC
10.60	415.1450	-	367.3549, 343.8891, 279.9969, 146.9654	UC
10.60	461.1507	-	415.1418	UC
11.10	333.0571	-	241.0105 (MS^3 – 78.9589), 152.9953	galactosyl glycerol phosphate
12.45	325.1836	-	253.0888, 239.0734, 225.0578, 216.0087, 197.0269, 183.0114, 170.0036, 119.0499	UC

T.salsuginea - Group A late-stress features

t_R /min	*m/z*	Putative molecular formula	Direct Infusion Fragment ions / *m/z*	Assignment
2.50	251.1015	$C_{10}H_{16}N_2NaO_4$	114.0557	Proline charge-sharing dimer
6.30	307.0650	-	195.0498, 177.0395, 129.0187	UC
6.30	413.0862	-	377.0659 (MS^3 – 329.0457), 195.0498	UC
16.65	421.1864	$C_{12}H_{23}O_{14}P$	353.1965, 309.1713, 241.0100, 87.0403	Trehalose-6-phosphate
19.30	277.1819	-	114.0556	Proline-bound metabolite

A. thaliana - Group A late-stress features

t_R /min	*m/z*	Putative molecular formula	Direct Infusion Fragment ions / *m/z*	Assignment
10.45	257.0257	-	-	UC
11.60	309.1739	-	183.0121	UC
13.80	191.0197	$C_6H_7O_7$	173.0090, 129.0193, 111.0087	Citric acid/ Isocitric acid
13.80	405.0235	$C_{12}H_{16}O_{14}Na$	191.0180	Citric acid charge-sharing dimer
16.00	384.9724	-	340.0714, 325.2130, 314.2699, 268.9615, 214.1448, 186.1135	UC

Table 3.1: Accurate *m/z* values and fragment ions for targeted features using negative ion direct infusion FT-ICR-MS/MS, where bracketed MS^3 values are the fragment ions produced by SORI-MS. [a]UC = Unknown Compound

3.5 Conclusions

The aim of the study in this chapter was to analyse and compare the progressive effects of drought stress on leaf blade tissues of *A. thaliana* and *T. salsuginea*. A PGC-LC-UHR-QTOF-MS method was used in the untargeted analysis of water-soluble metabolites extracted from leaf blade samples of *A. thaliana* and *T. salsuginea*. The samples were divided into early-stress (control (day 0) plus 1 day, 3 days and 5 days after initiation of drought stress) and late-stress (12 days and 13 days after initiation of drought stress). Full scan LC-MS datasets were collected and analysed using multivariate and univariate statistical techniques.

In PCA scores plots for the two plant species, separation of late-stress samples and control/early-stress samples was the dominant observation. For *T. salsuginea* early-stress samples, a progression according to stress state was observed when considering only those variables already identified as late stress markers (Group A). This progression was less pronounced in the *A. thaliana* data and suggests that *T. salsuginea* responds much earlier to drought stress. When applied to early-stress samples, Group B markers (variables of low contribution to sample split) showed no significant progression paralleling increasing stress state in either plant species.

Targeted analysis of key discriminant features from Group A markers was performed using MS^2 and MS^n strategies. Ranked lists of features showing late stress response for *T. salsuginea* and for *A. thaliana* as well as features showing early stress response in *T. salsuginea* were compiled. In all three lists, various molecular species of the osmoprotectant sucrose dominated the rankings, although citric acid was also identified as a prominent feature. In addition, two possible features related to proline were assigned; proline has been demonstrated to act as an ROS scavenger and protein protectant during drought stress. A feature corresponding to a potential galactosyl glycerol phosphate was also assigned. Future work in this study includes the analysis of reference standards for the current potential assignments as well as further literature and database searching to identify the other unknown compounds.

Chapter 4

Effects of pyrolysis rate on the pore structure and adsorbent capacity of naturally-templated alginic acid-derived Starbon®

4.1 Introduction

Chapters 2 and 3 give some indication as to the ability of porous graphitic carbon to separate polar analytes. There has been minimal advancement in synthesis of this material type; a likely result of the dominance of Hypercarb™ over the PGC market. In recent years, researchers in the Green Chemistry Centre of Excellence at the University of York have developed a biomass-derived porous carbon material termed Starbon® which offers a more sustainable naturally-templated synthetic route in comparison to industrially-manufactured PGC. In particular, work by White *et al.* has shown the potential for this material to be used in liquid chromatography by separating a range of carbohydrates (White *et al.*, 2010). The work in this chapter and chapters 5 and 6 describe further research conducted to improve on the current synthesis of Starbon® in order to develop a high-performance stationary phase medium.

One of the rate-limiting processes in the preparation of alginic acid-derived Starbon® is the pyrolysis program used to carbonise the aerogel precursor. White *et al.* (White *et al.*, 2010) used a variable rate program involving several stages whilst Parker *et al.* (Parker *et al.*, 2013) used a single rate program to reach the final temperature of carbonisation. However, both program types retain low pyrolysis rates which lengthens the time for carbonisation and thus for preparing the final product. This has been a feature of pyrolysis programs in the preparation of other carbon aerogels (Zhang *et al.*, 1999; Horikawa *et al.*, 2004; Job *et al.*, 2005) and presents a real obstacle both in terms of the energy and financial costs associated with slow pyrolysis under an inert atmosphere which reduces the cost effectiveness of preparing these materials on an industrial scale.

There are few examples of literature which report the effect of pyrolysis rate on the textural properties of porous carbons. Previous investigations have been carried out with carbon xerogels (Moreno *et al.*, 2013) as well as mesoporous carbons prepared by liquid impregnation (LI) and chemical vapour deposition (CVD) methods (Yang and Mokaya, 2008). Pyrolysis rate was found to have a limited effect on the porosity of both carbon xerogels and CVD-prepared carbons whilst LI-prepared carbons showed increased structural disorder and micropore development at high pyrolysis rates. In particular, the results reported by Moreno *et al*. (Moreno *et al*., 2013) mean that carbon xerogels can be carbonised on a faster timescale than before without significantly affecting textural properties, making their synthesis more attractive to take to industrial scale.

The effect of pyrolysis rate on the textural properties of naturally-templated porous carbons, including Starbon®, has not been studied previously. Were Starbon® to follow the trend of carbon xerogels and CVD-prepared porous carbons, maintaining mesoporosity at higher pyrolysis rates, then the time required to carbonise Starbon® could be diminished significantly. However, should Starbon® follow the trend of LI-prepared porous carbons it would mean that slow pyrolysis rates would need to be retained when preparing the materials for chromatographic applications.

4.1.1 Aims

The aim of the study in this chapter was to determine the effect of pyrolysis rate on the textural properties and adsorption capacity of alginic acid-derived Starbon® materials. The impact of pyrolysis rate on these materials was analysed using N_2 sorption porosimetry and thermal gravimetric techniques. The effect on adsorption capacity was determined by methylene blue adsorption. The general aims of the work in this chapter are summarised as follows:

- Prepare alginic acid-derived Starbon® materials at several rates of pyrolysis.
- Analyse the effect on textural properties of these materials using N_2 sorption porosimetry.
- Analyse the effect on mass loss and volatile release from these materials using thermal gravimetry (TG) and thermal gravimetry-infrared (TG-IR) analysis.
- Test adsorbent capacity by studying the adsorption of the dye molecule methylene blue.

4.2 Experimental

4.2.1 Synthesis of alginic acid-derived Starbon® materials

Alginic acid from brown algae (Sigma Aldrich, UK) was gelatinised in distilled water (1 g: 20 mL alginic acid:water ratio) and stirred for 2 h at 90 ^{o}C. The resulting gel was then retrograded at 5 ^{o}C for 24 h. The water was exchanged for ethanol and the resulting alcogel dried in supercritical CO_2 ($scCO_2$). Drying was conducted using a Thar SFE-500 supercritical extractor heated to 40 ^{o}C and held at a pressure of 120 Bar for 2 h under dynamic flow conditions (40 g min^{-1} CO_2). The extractor was subsequently allowed to depressurise over a period of 12 h. The dried aerogel was pyrolysed by heating under a N_2 atmosphere (N_2 flow: 100 mL min^{-1}, BOC) in a Netzsch 409 thermal gravimetric system fitted with a 3.5 mL alumina crucible. Prior to heating the oven was evacuated and backfilled two times with N_2. All samples were pyrolysed to 800 °C.

4.2.2 N_2 sorption porosimetry

N_2 sorption porosimetry was performed using a Micrometrics ASAP 2010 porosimeter with samples dried under vacuum for 4 h at 90 ^{o}C to remove any residual moisture prior to analysis. Figures were generated using OriginPro 8 software.

4.2.3 Thermal gravimetry-infrared (TG-IR) spectroscopy

TG-Infrared (TG-IR) spectroscopy was performed under a N_2 atmosphere using Netzsch 409 thermal gravimetric system coupled via a heated transfer pipe to a Bruker Equinox 55 FT-IR spectrometer. Samples (sample weight 100 mg) were mounted into a 3.5 mL aluminium crucible. The oven was evacuated and backfilled three times prior to analysis. Data was collected in chromatography mode set at 64 scans per spectrum. The spectrometer resolution was 4 cm^{-1}.

4.2.4 Methylene blue adsorption study

A 10 mg L^{-1} standard stock solution of methylene blue dye was prepared in a 2 L volumetric flask using deionised water. Sample material (5 mg) was weighed into a sample tube which was then filled with 25 mL of the stock dye solution and stirred for 24 h. (Due to complete adsorption of dye by the 1 and 2 K min^{-1} samples at this scale, 5 mg of sample material was stirred in 100 mL stock standard solution in a 100 mL volumetric flask). The non-adsorbed dye solution was filtered and UV-vis analysis performed using a Jasco V-550 UV-vis spectrometer.

4.3 Results and Discussion

4.3.1 Sample preparation

The pyrolysis precursor was prepared following the method of Parker *et al*.(Parker *et al*. 2013) after which pyrolysis to 800 ^{o}C was conducted at heating rates of 1, 2, 3, 5, 6, 7, 10 and 20 K min^{-1} using a Netzsch 409 thermal gravimetry (TG) system. The TG system was used to prepare the samples as it afforded good heating control under an inert N_2 atmosphere as well as providing key information in understanding the effect of rate of pyrolysis on the resulting materials.

4.3.2 N_2 sorption porosimetry analysis

Table 4.1 summarises the N_2 sorption data collected for each sample. The main observations are the decrease in both desorption pore volume and average pore diameter, suggesting that there is a decline in mesoporosity as the rate of pyrolysis is increased. This trend is visualised by comparing pore size distribution plots (Figure 4.1(a)); here, dV/dlog(D) at a given pore diameter is directly related to the volume of nitrogen gas adsorbed. For materials formed at low rates of pyrolysis a significant proportion of nitrogen is adsorbed in the mesopore/ low macropore region (2-50 nm) in the form of a peak centred around 20 – 30 nm. As pyrolysis rates increase, this peak volume reduces and shifts towards the micropore region such that when the precursor is pyrolysed at 3 K min^{-1} macroporosity (defined as a pore diameter > 50 nm) disappears completely. By 10 K min^{-1} there is no discernable mesopore peak with a complete shift to the micropore region observed.

[a] k_p / K min^{-1}	[b] S_{BET} / m^2 g^{-1}	[c] PV_{des} / cm^3 g^{-1}	[d] PD / nm	[e] SE_{D-R} / kJ mol^{-1}	[f] Mic. / %
1	492	0.78	12.89	23.03	23.2
2	400	0.51	11.42	23.94	27.8
3	385	0.42	10.35	24.77	31.8
5	310	0.21	9.05	23.97	44.2
6	313	0.18	8.18	25.90	48.5
7	434	0.15	7.74	30.22	60.9
10	585	0.07	3.85	31.73	86.8
20	465	0.02	3.64	32.75	93.5

[a] k_p = Pyrolysis heating rate, [b] S_{BET} = Brunauer-Emmett-Teller surface area, [c] PV_{des} = Barrett-Joyner-Halenda (BJH) desorption pore volume, [d] PD = BJH desorption average pore diameter, [e] SE_{D-R} = Dubinin-Radushkevich surface energy, [f] Mic. = Percentage microporosity

Table 4.1: N_2 sorption data for all pyrolysed Starbon® samples

N_2 sorption isotherm plots for Starbon® samples generated at each of the different heating rates (Figure 4.1(b)) provide further evidence of this general trend. The isotherm plots show a progression of the volume of N_2 adsorbed at the material surface as the system relative pressure (P/P_o) is increased from 0 to 1 and then subsequently desorbed leading to the Type IV hysteresis loops observed. Figure 4.1(b) shows how the amount of N_2 adsorbed by meso/macropores, represented by the rise in the volume of gas adsorbed above ca. 0.8 P/P_o, evidently reduces as the heating rate is increased. It is also noted that the hysteresis loops broaden as mesoporosity reduces indicating that the external pore openings are narrower in materials generated at higher pyrolysis rates.

The surface energy of a material determined by the Dubinin-Radushkevich equation, correlates to the adsorption potential of that material and these values for the pyrolysed Starbon® materials are also given in Table 4.1 (Hsieh and Teng, 2000). Here, surface energy values (SE_{D-R}) tend to increase with increasing rates of heating with a marked change in these values between 6 and 7 K min^{-1}.

This adsorption potential step change, between the materials formed at 6 and 7 K min^{-1}, may be due to the large increase in microporosity between these samples. The narrow gap between the walls of a micropore can lead to the overlap of adsorption potential thus intensifying the attractive forces at these pores and enhancing adsorption potential above that theoretically expected (Lowell and Shields, 1991). The BET surface area (S_{BET}) difference between the sample pyrolysed at 6 K min^{-1} and those pyrolysed at 7 K min^{-1} and above is considerable, whilst supporting data from the pore size distribution plots for these higher heating rate samples highlight an apparent rise in the proportion of the total pore volume associated with the ultra-micropore region (< 0.7 nm). The rise in ultra-micropore content is likely due to the collapse of micro/mesopore structure during pyrolysis and could result in the overall adsorption potential step change between the sample pyrolysed at 6 K min^{-1} and those pyrolysed at higher rates.

Overall, the porosimetry results show that when using high pyrolysis rates, the textural properties of Starbon® are altered from a predominantly mesoporous pore network to a microporous carbon. This, in part, follows the trend reported by Yang and Mokaya for mesoporous carbons prepared using a LI method (Yang and Mokaya, 2008), where an increase in microporosity was observed at higher pyrolysis rates. However, a key difference is that Yang and Mokaya used a silica template to prepare the mesoporous carbon, as such the increase in microporosity was much less dramatic than that shown for Starbon® and pore volume and surface area was largely preserved for the LI-prepared carbons, again unlike for Starbon®.

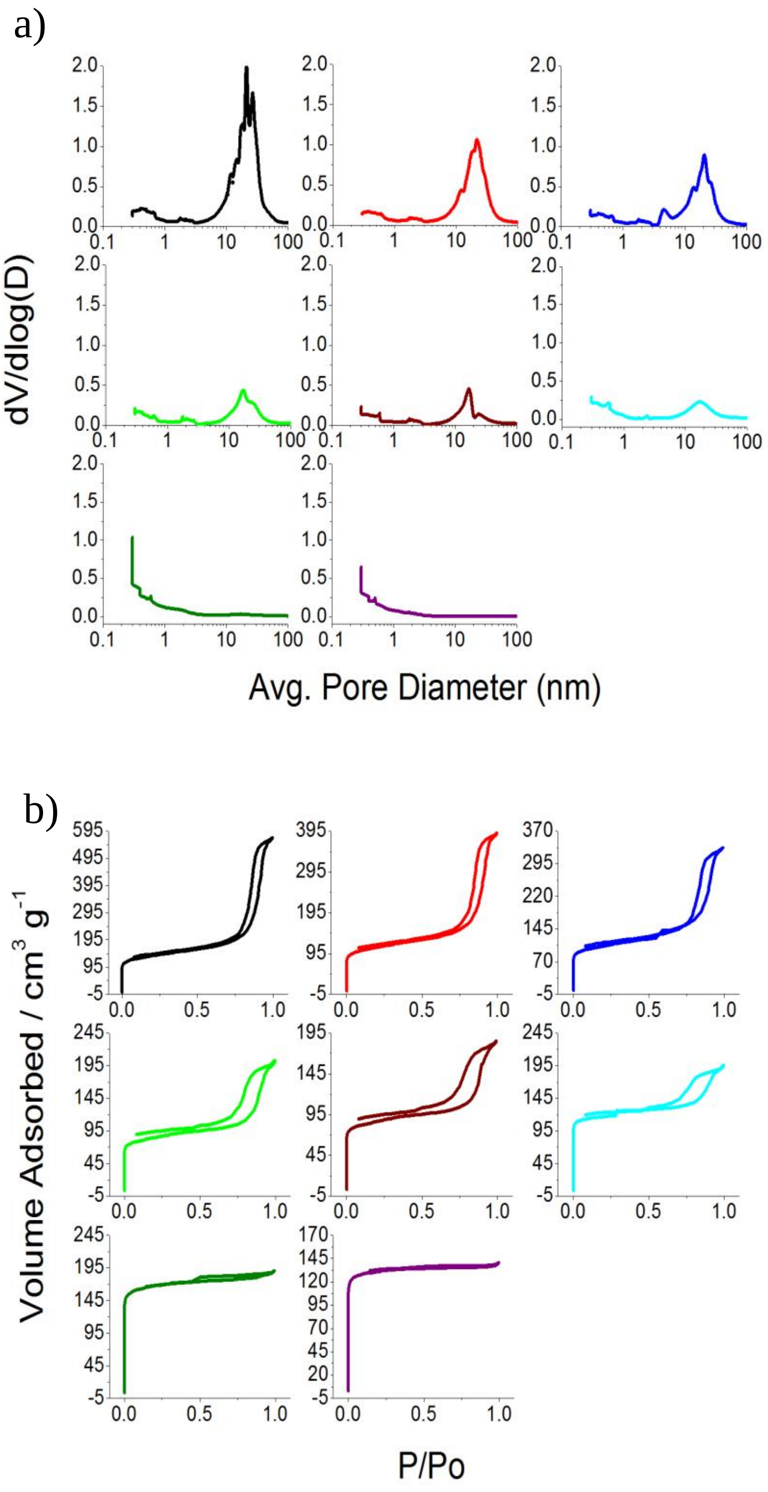

Figure 4.1: (a) Adsorption pore size distribution and (b) N_2 sorption isotherm plots. The plots are arranged in ascending order of pyrolysis rate, represented by the following colours: 1 K min^{-1} = Black; 2 K min^{-1} = Red; 3 K min^{-1} = Blue; 5 K min^{-1} = Light Green; 6 K min^{-1} = Brown; 7 K min^{-1} = Cyan; 10 K min^{-1} = Dark Green; 20 K min^{-1} = Purple

4.3.3 Thermal gravimetric analysis

In order to study the pyrolysis process and how the rate of heating affects the material during the pyrolytic formation of Starbon®, data from TG, differential TG (DTG) and TG coupled to a Fourier-transform infrared spectrometer (TG-IR), recorded during the pyrolysis process, were examined. Figure 4.2(a) provides a representative profile of the TG and DTG data collected during pyrolysis at 1 K min^{-1}, the remaining heating rates showed very similar profiles. The TG trace shows two steps of decomposition; the first, between 50 and 110 ^{o}C is associated with water loss. The second, at around 220 ^{o}C, is a more significant decomposition step which results in mass loss of 30-40 %. This step is associated with the decarboxylation of the uronic acid residues and has been described previously (Perlin, 1952; Soares *et al*., 2004). Above 220 ^{o}C, further mass loss associated with the loss of other functionalised groups (e.g. olefins) was observed however this occurred at a much slower rate..

Figure 4.2(b) plots the DTG data for all samples, where the maximum rate of decarboxylation is determined at the apex of the DTG peak. Increasing the rate of pyrolysis results in a corresponding rise in the maximum rate of decarboxylation, which in turn implies that there is a greater volume of volatiles generated per minute. This was confirmed by TG-IR analysis which was used to record the volatile components emitted from the sample. Figure 6.3 shows the TG-IR time-series for the Starbon® sample pyrolysed at 10 K min^{-1} which is dominated by the intense asymmetric stretch band of carbon dioxide (ca. 2300 cm^{-1}) released on decarboxylation. TG-IR at slower rates of pyrolysis (2 K min^{-1} and 5 K min^{-1}) produced similar plots, although the intensity of the carbon dioxide stretch was much reduced indicating that the rate of CO_2 evolution was much lower in these samples.

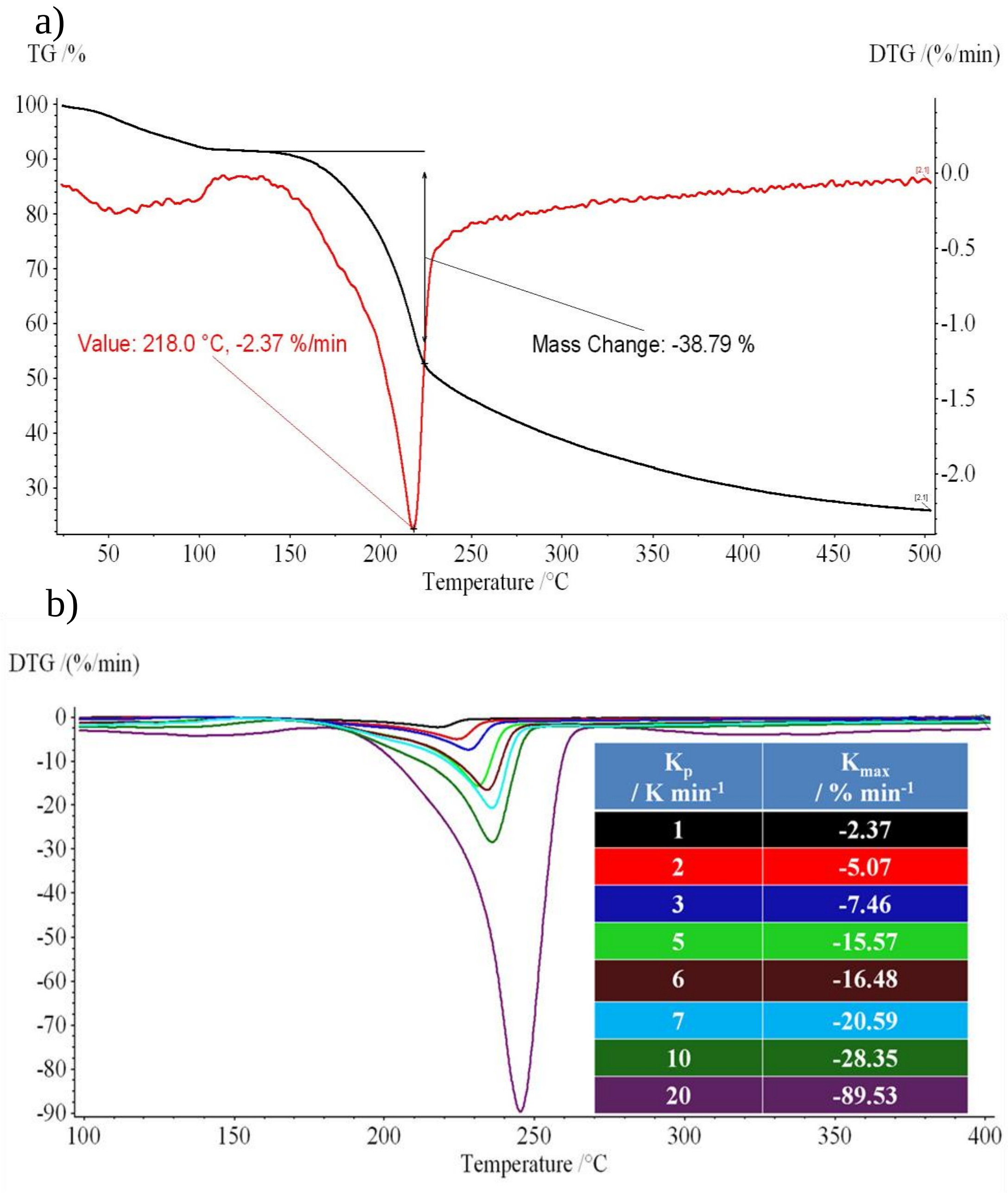

Figure 4.2: (a) Representative thermal gravimetry (TG-black line) and differential TG (DTG-red line) plots showing effect of pyrolysis at 1 K min^{-1}; (b) DTG plots for all samples with table showing K_{max}, the maximum rate of mass loss per sample

The generation of increasing volumes of volatile molecules as the rate of pyrolysis increases suggests that greater pressure would be exerted on the pore network of these materials and that they are increasingly prone to structural collapse. Coupled to this, it has previously been reported that the pyrolysis of expanded polysaccharides in the presence of water causes the collapse of the pore networks (Budarin *et al*., 2006; Robitzer *et al*. 2011a). This is due to the high surface tension of water generated at the hydrophilic polysaccharide pore walls which, when volatilised, exerts sufficient force to weaken and thus collapse the pore structure. Although the water in our preparation was exchanged for an organic solvent and then dried ($scCO_2$), water may still be present due to residual surface tension in the narrow, polar pore networks (Job *et al.*, 2005). In addition, water vapour, potentially generated from the breakdown of the carbohydrate residues' hydroxyl groups was observed by TG-IR spectroscopy during pyrolysis. At fast pyrolysis rates it is conceivable that sufficient water vapour is generated to weaken the sample pore structure. This, combined with the pressure arising from the rapid production of volatiles are believed to be the factors which affect the Starbon® pore structure during fast pyrolysis.

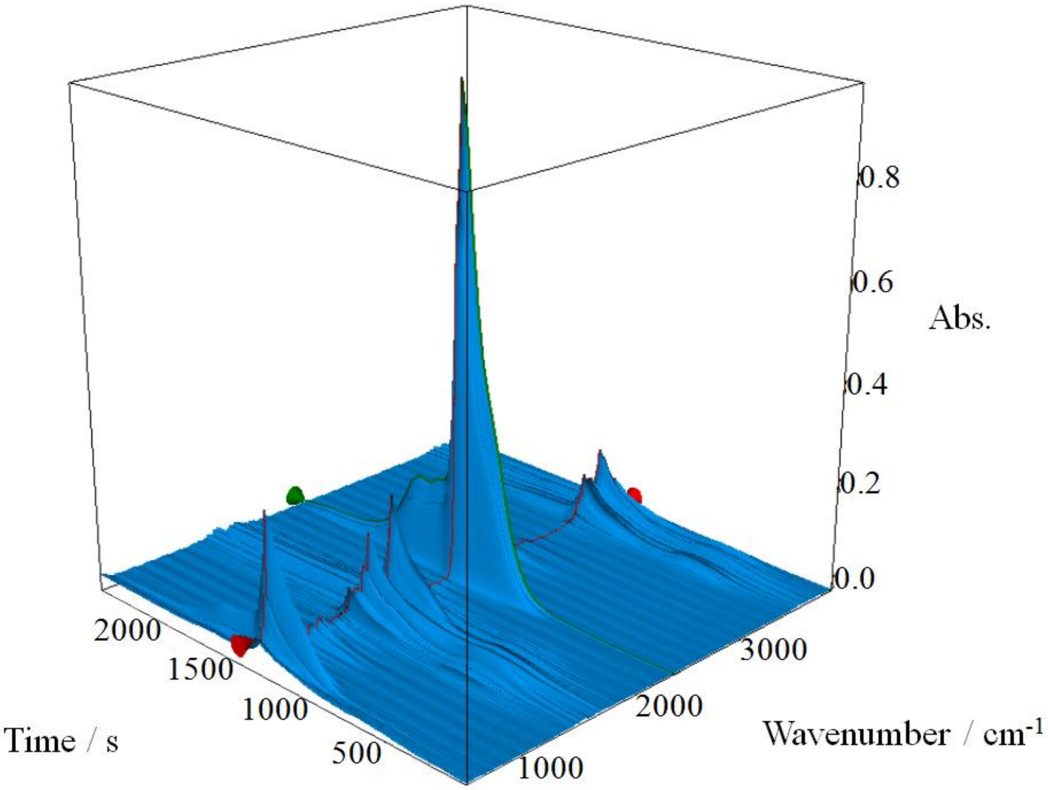

Figure 4.3: TG-IR time-series of alginic acid-derived Starbon® pyrolysed at 10 K min^{-1}

The factors postulated here are in agreement with those of Yang and Mokaya, who suggested that rapid gas evolution from higher rates of heating was responsible for disrupting the forming carbon network in LI-based porous carbon synthesis (Yang and Mokaya, 2008).

4.3.4 Methylene blue adsorption study

Pyrolysis rate has a clear effect on the textural properties of Starbon® with the materials generated being more microporous at higher rates. As a chromatographic stationary phase, the development of microporosity is detrimental to Starbon® as these pores can result in irreversible binding of analytes. The formation of ultramicropores at the highest pyrolysis rates (> 7 K min^{-1}) also reduce the accessibility of analytes through these materials. The ability to separate analytes by chromatography depends on the analytes ability to interact with the stationary phase, whereby the larger the number of interactions, the higher the resolution and the better the separation of the analytes. Therefore, an important property required by Starbon® as a stationary phase is accessibility to as high a proportion of the surface area as possible in order to maximise the number of sites of interaction.

In 2000, Hsieh and Teng reported how increasing the proportion of the total pore volume that was due to mesopores enhanced the adsorption capacities of activated carbons, determined by comparing carbons with differing mesopore content but similar total pore volumes (Hsieh and Teng, 2000). An adsorption study using the dye molecule methylene blue (Figure 4.4) was performed in order to determine how material adsorption capacity may be altered by the mesopore content of Starbon®, as well as provide evidence in order to evaluate the differences in material accessibility. The material (5 mg) was stirred in a vessel containing a 10 mg L^{-1} stock solution of methylene blue for 24 hours and the absorbance measured by UV-visible spectroscopy from which the adsorbent capacity was determined.

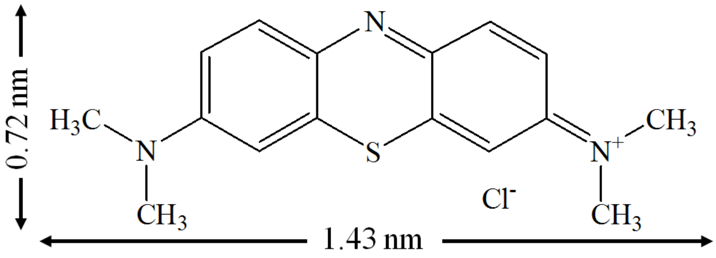

Figure 4.4: Structure and dimensions of methylene blue

The data, summarised in Table 4.2, shows a clear trend of decreasing adsorbent capacity with decreasing sample mesoporosity. The adsorbent coverage value shows the percentage area of the adsorbent that has adsorbed the dye, assuming monolayer coverage. The coverage is larger for materials produced at lower heating rates with increased accessibility due to the extended mesopore network in these materials. The trend in adsorbent capacity is reversed slightly between samples pyrolysed at 6 K min^{-1} and 7 K min^{-1} although this could be due to the large increase in total surface area countering the reductions in both pore diameter and pore volume. Above 7 K min^{-1} adsorption is limited and shows that these materials, with large surface areas but exhibiting a high ultramicropore content, are almost totally inaccessible to the dye. This result also appears to correlate well with the the desorption pore volume of the materials (Table 4.1). The adsorbent capacity calculated for Norit (39 mg g^{-1}) was within 10 % of that reported by Parker *et al.* (42 mg g^{-1} - Parker *et al.*, 2013) and is just one third that of the best adsorbing Starbon®.

[a] k_p / K min^{-1}	[b] Adsorbent Capacity / mg g^{-1}	[c] Surface Area / m^2 g^{-1}	[d] Adsorbent Coverage / %
Norit	39	71	9
1	138	252	51
2	110	201	50
3	47	86	22
5	39	71	23
6	25	46	15
7	30	55	13
10	10	18	3
20	9	16	4

[a] k_p = Pyrolysis heating rate, [b] Calculated based on the UV-visible adsorbance of methylene blue at 664 nm, [c] Based on methylene blue surface area = 1.026 nm^2, [d] Adsorbent Coverage = (Surface Area of Adsorbed Methylene Blue/BET Surface Area)*100 (Assumes monolayer coverage only)

Table 4.2: Adsorbent capacities and surface area dye coverage for methylene blue

4.4 Conclusions

The rate of pyrolysis has been investigated for the first time on the textural properties of alginic acid-derived Starbon®. In general, the mesoporosity of Starbon® decreases with increasing rates of pyrolysis and eventually leads to a predominantly microporous material. The results correlate well with the observations made by Yang and Mokaya (Yang and Mokaya, 2008) for LI-prepared porous carbons.

The internal pressures associated with rapid formation of volatile compounds, as well as the increased surface tension and pore shrinkage due to the presence of water vapour are proposed to be the factors affecting mesopore content in Starbon® produced at high rates of pyrolysis. This effect on porosity was investigating by determining the adsorption capacities of these materials for the dye molecule methylene blue. The results showed that there was a positive correlation between mesopore content and adsorption capacity highlighting the importance of mesopores for both adsorption and, consequently, chromatography applications.

With regards to developing Starbon® as a chromatographic stationary phase, the results show that a lower pyrolysis rate is favoured to produce materials with larger mesoporous pore volumes (increasing analyte accessibility) and a less microporous pore network. These characteristics will help improve column efficiency, through increasing the potential sites of interaction, whilst reducing the potential for unfavourable irreversible binding of analytes in highly adsorbent micropore channels.

Chapter 5

Investigation into morphological control of alginic acid-derived Starbon® towards high-performance separations applications

The work described in this chapter has been published in:

A natural template approach to mesoporous carbon spheres for use as green chromatographic stationary phases

***RSC Advances*, 4 (2014) 222-228**

Andrew S. Marriott[1,2], Ed Bergström[2], Andrew J. Hunt[1], Jane Thomas-Oates[2], James H. Clark[1]

[1]*Green Chemistry Centre of Excellence, Department of Chemistry, University of York, Heslington, UK*
[2]*Centre of Excellence in Mass Spectrometry, Department of Chemistry, University of York, Heslington, UK*

5.1 Introduction

In liquid chromatography, the column efficiency (i.e. the number of theoretical plates, where a “plate” is a point of interaction between the analyte and stationary phase)) of a particle-packed column is influenced by three factors: eddy diffusion (A-term); longitudinal diffusion (B-term); and mass transfer (C-term), proposed by Van Deemter in the 1950's (Van Deemter *et al*., 1956). The development of high-quality commercial columns comes from the ability to form a homogenous, stable bed of stationary phase particles to give reproducible chromatography. Particle size and morphology are key parameters that need to be controlled in order to produce high performance stationary phase material. One of the advantages of the alginic acid-derived Starbon® synthesis over that of commercial PGC is the natural formation of a mesoporous structure without the need for a silica template (White *et al*., 2010). However, the current method of synthesis includes no steps to ensure the generation of particles which exhibit the narrow size distribution and circular morphology required for high performance stationary phase material.

Particle size alters the efficiency of a column by affecting the A- and C-terms. Theoretically, smaller particle sizes result in smaller interstitial sites between particles and therefore a more homogeneously packed column; however, a recent investigation by Gritti *et al*. into the effect of particle size distribution on band broadening suggests that adding a small proportion of larger particles to a batch of small particles can improve column packing (Gritti *et al*., 2011). This minimises the influence of the A-term by reducing the pathlength variance as analyte molecules pass through the column. A smaller particle size also means that a greater number of particles are packed into a column of a defined volume than if that column was packed with particles of a larger size. This in turn increases the plate count of that column, increasing the efficiency. For example, a recent study by Durham and Hurley (Durham and Hurley, 2007) described the enhanced resolution capabilities of sub 2 µm particle packed columns over the more common 5 µm particle packed columns. In addition, Unger *et al*. (Unger *et al*., 2008) described how reducing particle size aids mass transfer by minimising the diffusion pathlength into the pore structure. However, a major limitation is that as the particle size decreases the back pressure of the column increases. Thus there is a lower limit to the size of particle that can be packed, dependent on the maximum pressure of the HPLC system (Kirkland and DeStefano, 2006; Unger *et al*., 2008).

In terms of particle morphology, several studies have shown that columns packed with small spherical particles outperform those packed with irregular particles of equivalent size, and that this is related to the method of packing (Verzele *et al*., 1987; Unger *et al*., 2008; Lottes *et al*., 2009). Slurry packing (and variations of this) is the commonly used packing process, where the stationary phase is mixed with solvent into a slurry before being packed into a column under high pressure (Unger *et al*., 2008). Spheres slide over each other much more easily than do irregular shapes, which lowers the rate of particle agglomeration which reduces the viscosity of the slurry compared to that of a slurry containing irregular particulates. This, in turn, ensures quick settling and the generation of a flat, stable particle bed (Verzele *et al*., 1987; Lotte *et al*., 2009).

Controlling the morphology and size of Starbon® particles has not been investigated previously; therefore investigating synthesis methods to this end (whilst retaining mesoporosity) would improve the packing properties of Starbon® (and therefore efficiency of the resulting column) for HPLC applications.

5.2 Aims

The aim of the study in this chapter was to investigate processes which provided particle size and morphology control during Starbon® synthesis, whilst retaining the inherent mesoporosity of the material. Milling (hand and mechanical), spray drying, and sodium alginate spraying methods were investigated. Promising materials were packed into columns and their performance compared to that of a Starbon® packed and a commercial PGC column. The general aims of the work in this chapter are summarised as follows:

- Study the effects of milling (hand and mechanical) and spray drying techniques on Starbon® particle size and morphology, using particle size distribution (PSD) and particle circularity measurements.
- Study pore characteristics of the resulting materials using N_2 porosimetry.

- Investigate the method of sodium alginate spraying for its ability to generate alginate spheres and the effect of calcium removal on the structure of the spheres.
- Compare and contrast the chromatography and efficiency of HPLC columns packed with alginate spheres and Starbon® against a commercial PGC column.

5.3 Experimental

5.3.1 Preparation of alginic acid-derived Starbon®

Alginic acid from brown algae (Sigma Aldrich) was mixed in deionised water (1 g: 20 mL alginic acid:water). The mixture was stirred for two hours at 90 °C. The resultant sol gel was then cooled for a minimum of 24 h at 5 °C. The removal of water was performed by solvent exchange with ethanol, a lower surface tension solvent, using a method reported previously (Robitzer *et al.*, 2008). The excess solvent of the resulting alcogel was removed by Buchner filtration and dried using a Thar SFE-500 supercritical carbon dioxide extractor heated to 40 °C at a pressure of 120 Bar for 4 h under dynamic flow conditions (40 g min^{-1} CO_2). The extractor was depressurized slowly over 12 h.

Pyrolysed material was prepared by heating under a N_2 atmosphere (N_2 flow: 150 mL min^{-1}, BOC) in a ceramic furnace which contained a quartz round bottomed flask. All samples were pyrolysed to 800 °C at a rate of 1 K min^{-1} followed by a hold of 20 min.

5.3.2 Preparation of calcium alginate mesoporous carbon spheres (AMCS)

Sodium alginate (Sigma-Aldrich) was mixed in deionised water (1 g : 50 mL sodium alginate : water) to yield a viscous solution. The solution was passed through an electrospray ionization emitter source at 1 mL/min using a constametric 3200 solvent delivery system (LDC Analytical). The solution was nebulized using 9 psi air, and sprayed into a constantly-stirred solution of 0.24 M calcium chloride and cured in solution for 24 h to prepare hydrogel spheres of calcium alginate. The hydrogel spheres were transferred into deionised water and washed. At this stage the spheres were acid-washed using hydrochloric acid (0.1 M or 0.5 M), as required, to reduce the calcium content of the material. Solvent exchange, $scCO_2$ drying and pyrolysis were carried out as above.

5.3.3 Milling conditions

Hand-milling was performed using a ceramic pestle and mortar. The Starbon® sample was ground for five hours. Ball-milling was performed using a Retsch PM400 planetary ball mill. The Starbon® sample was sealed in a milling chamber with seven steel ball bearings. The sample was milled at 300 rpm for 15 min.

5.3.4 Spray-drying conditions

Spray-drying was performed using a Büchi-290 mini spray-dryer coupled with a Büchi B-295 inert loop. For all experimentation the spray-dryer was operated by Rob Osborne (Büchi, UK) at Büchi UK Ltd. (Oldham, UK).

5.3.5 Particle size and morphology analysis

Particle size distribution and particle circularity were measured using a Micromeritics Particle Insight instrument. All analysis was performed by Chris Pilkington (Micromeritics, UK).

5.3.6 N_2 sorption porosimetry

Porosimetry analysis was performed using a Micromeritics TriStar. Samples were degassed under room pressure at either 110 °C for 8 h for non-pyrolysed materials or 160 °C for 6 h for pyrolysed materials prior to analysis.

5.3.7 X-ray fluorescence spectrometry

X-ray fluorescence spectrometry was performed using a Rigaku NEX-CG XRF spectrometer fitted with a 50 W X-ray tube with Pd anode. Samples were filled into 32 mm sample cups to a depth of 10 mm. Data were analysed (i.e. elemental quantification and peak fitting routines) using RPF-SQX software.

5.3.8 Scanning electron microscopy

Images were obtained from a JEOL 6490LV SEM system. Samples were sputter-coated with gold/palladium before analysis. Images were collected by Ms. Meg Stark (Technology Facility, University of York, UK)

5.3.9 Fourier-transform infrared (FT-IR) spectroscopy

Spectra were recorded using a Bruker Vertex 70 FT-IR spectrometer fitted with an attenuated total reflectance (ATR) golden gate attachment with diamond top plate analysis window. Resolution was 4 cm^{-1} and 64 scans were averaged to obtain the spectra in the 4000 – 600 cm^{-1} range. Spectra were recorded using a blank analysis window as a reference.

5.4 Results and discussion

5.4.1 Study of Starbon® particle morphology

Figure 5.1 shows the scanning electron microscopy (SEM) image of Starbon® prepared by heating to 800 °C at 1 K min^{-1}. It is clear that there is considerable heterogeneity in both particle size and shape, and the size distribution of these particles is very broad.

The Starbon® particles were compared against a commercial equivalent (Hypersil 5 µm), which has the particle morphology characteristics desired for chromatographic applications. Table 5.1 summarises the data, comparing mean particle diameter and mean particle circularity, the latter measuring the "roundness" of a particle on a scale from 0-1 where 1 means the particle fits to a perfect sphere, determined by image analysis of particles suspended in solution.

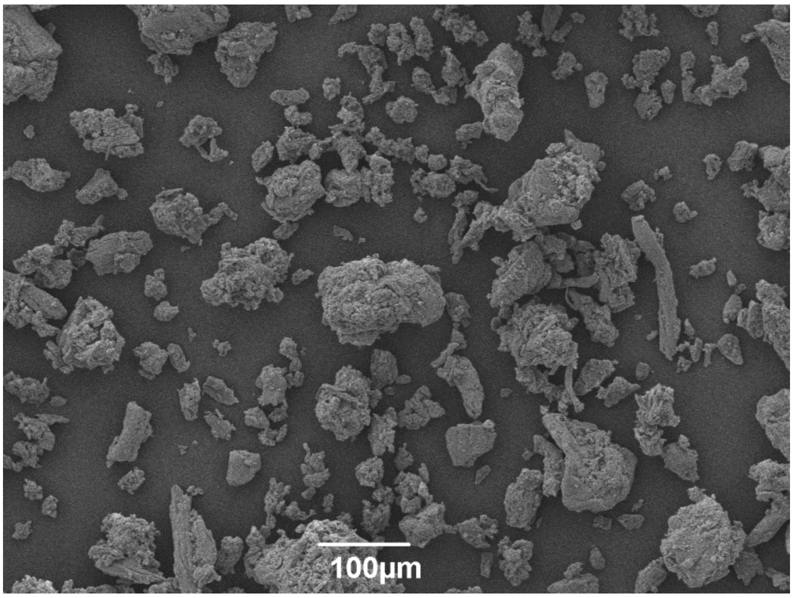

Figure 5.1: SEM image of Starbon® prepared by heating to 800 °C at 1 K min^{-1}

Sample	[a]MPD / µm	[b]MPD-SD / µm	[c]MPC	[d]MPC-SD
Commercial PGC	7.0	6.6	0.777	0.163
Starbon®	28.6	12.6	0.594	0.162

a = Mean particle diameter; b = MPD standard deviation; c = Mean particle circularity (1.000 = perfect sphere); d = MPC standard deviation

Table 5.1: Comparison of mean particle diameter and mean particle circularity for commercial PGC material and Starbon® material prepared on heating to 800 °C

Particle size analysis data by White (White, 2008) for Starbon® material described a bimodal distribution, with maximum values at 9.1 µm and 53.1 µm and an average value of 22.7 µm. Here, the particle size distribution was unimodal with a mean particle diameter of 28.6 µm. The difference in the mean average values between the two studies is likely a result of the differing pyrolysis temperatures (800 °C here, as opposed to the 1000 °C material prepared by White (White, 2008)) which means that the materials reported here have undergone less pyrolysis-induced shrinkage. However, the two different mean particle diameter values for Starbon® are still around four times larger than that of the commercial material, with the standard deviation value for Starbon® (800 °C) twice that of the commercial material. The particle circularity value for Starbon® is lower (0.594) than that of the commercial material (0.777) and in agreement with the SEM image, which highlights a wide variation in particle shape.

Several techniques were attempted in order to improve the particle size distribution and particle morphology of the Starbon® material in an attempt to generate material with characteristics similar to those of the commercial PGC material.

5.4.2 Milling

Two different milling techniques, hand-milling with a pestle and mortar and ball-milling, were tested with the aim of grinding the material to the desired size and shape. Both techniques are simple to set up, although ball-milling has the added advantage of being an automated process. For a comparison of the two techniques, a hand-milled sample was prepared by grinding a sample of Starbon® (prepared by pyrolysingd to 800 °C at 1 K min^{-1}) for five hours (termed HM-Starbon®-800); the ball-milled sample was milled for 15 minutes at a milling speed of 300 rpm (termed BM-Starbon®-800).

Table 5.2 shows the mean particle diameter and mean circularity and respective standard deviation values determined for the HM-Starbon®-800 and BM-Starbon®-800 samples by Micromeritics using their Particle Insight apparatus. The values for the un-milled Starbon® sample (termed UM-Starbon®-800) and commercial PGC materials are also included to aid comparison.

The mean particle diameter values for the two milled samples are lower than those of the un-milled Starbon® material and their standard deviation values (MPD-SD values of 7.3 and 5.0 for HM-Starbon®-800 and BM-Starbon®-800 respectively) suggest a narrower particle size distribution. In terms of mean particle circularity, HM-Starbon®-800 has values very similar to the commercial PGC material. The BM-Starbon®-800 material (0.656) has an improved particle circularity value over the un-milled material (0.594), although the BM-Starbon®-800 material has a broader distribution of circularities.

Sample	*a*MPD / µm	*b*MPD-SD / µm	*c*MPC	*d*MPC-SD
Commercial PGC	7.0	6.6	0.777	0.163
UM-Starbon®-800	28.6	12.6	0.594	0.162
HM-Starbon®-800	20.6	7.3	0.746	0.148
BM-Starbon®-800	17.6	5.0	0.656	0.176

a = Mean particle diameter; b = Mean particle diameter standard deviation; c = Mean particle circularity (1.000 = perfect sphere); d = Mean particle standard deviation

Table 5.2: Micromeritics Particle Insight analysis results comparing commercial PGC material and UM-Starbon®-800 material with HM-Starbon®-800 (96% particles in 10-70 µm range) and BM-Starbon®-800 (98% particles in 8-50 µm range)

The results from Particle Insight analysis suggest that hand-milling is the better method in terms of delivering particles which have a more uniform morphology. However, the process itself is highly labour and time intensive, especially if generating particles at the desired diameter range of 5-10 µm; therefore hand-milling is not deemed feasible for upscaling to generate sufficient material for packing test columns. Although particle shape is not adequate, the automated ball-milling process was able to produce particles of smaller and more uniform diameter than the un-milled material.

Microscopy and N_2 porosimetry techniques were used to determine the structural effects of ball-milling on Starbon® material. Scanning electron microscopy (SEM) images comparing un-milled (Figure 5.2(a)) and ball-milled (Figure 5.2(b)) material show the effect of ball-milling on particle morphology. The general appearance of the ball-milled material is that of agglomerated fragment particles generated from the fracturing of larger Starbon® particles. Particle shape appears to be varied and is in accordance with the particle circularity data for this material.

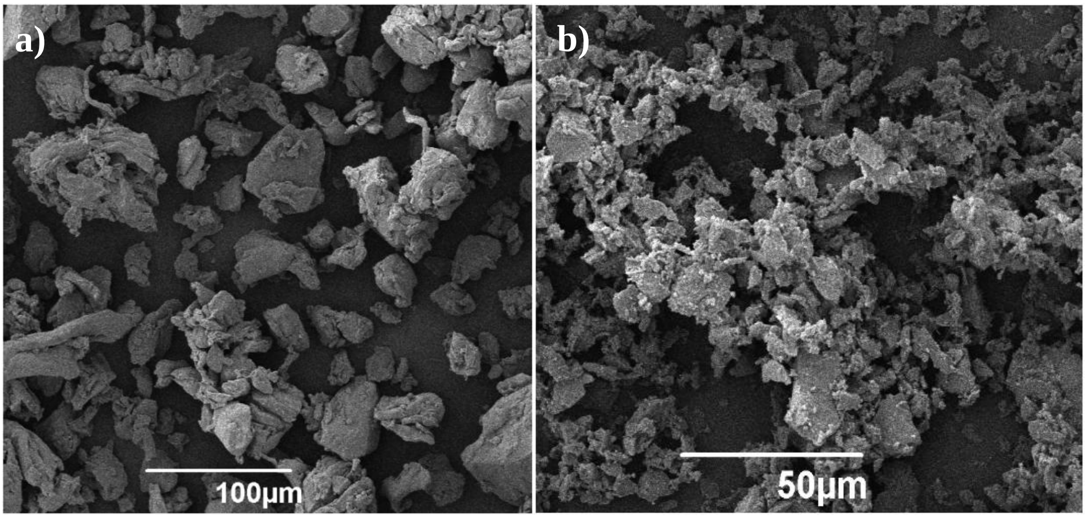

Figure 5.2: SEM images of (a) UM-Starbon®-800 and (b) BM-Starbon®-800 materials

Table 5.3 shows the N_2 sorption porosimetry data for the UM-Starbon®-800 and BM-Starbon®-800 material. The data clearly show that the structure of UM-Starbon®-800 is compromised when treated with the ball-mill, reducing the mesoporosity of the particles as well as significantly reducing the surface area of the material. Some loss of surface area is attributed to the rapid agglomeration of the particles after fracturing and could perhaps be reversed by ball-milling the materials in wet conditions e.g. in ethanol (Chen *et al.*, 1999). Although it has been suggested that there is a critical milling time, at which carbon materials reach a surface area maximum before it reduces again (Disma *et al.*, 1996; Chen *et al.*, 1999), this occurs through micropore formation and would not be favourable for generating stationary phase material.

Sample	${}^{a}S_{BET}$ / m^2 g^{-1}	${}^{b}V_{des}$ / cm^3 g^{-1}	${}^{c}PD_{des}$ / nm	^{d}Meso/Macro / %
UM-Starbon®-800	308	1.28	21.90	81
BM-Starbon®-800	49	0.07	9.57	68

a = BET surface area; b = BJH nitrogen desorption pore volume; c = BJH average desorption pore diameter; d = 100 – ((volume desorbed / total volume adsorbed)*100)

Table 5.3: N_2 sorption data for un-milled and ball-milled Starbon® material

It is clear that mechanical milling processes are too destructive for preparing smaller Starbon® particles whilst retaining mesoporosity, and that the resulting particle shapes are not acceptable.

5.4.3 Spray-drying

Spray-drying has been used as a technique for the high throughput synthesis of spherical mesoporous silica particles (Bruinsma *et al.*, 1997; Lind *et al.*, 2003; Ide *et al.*, 2011). The spraying mixture in all cases followed the Stöber method for mono-disperse silica particle formation (Stöber *et al.*, 1968), involving a water/ammonia/tetraalkoxysilane system in an alcohol solution, although modification of the original method was required to ensure the particles produced were mesoporous. The mixture, when spray-dried rapidly, calcines in air to produce dry mesoporous particles in the micrometer range. Ide *et al.* (Ide *et al.*, 2011) studied the effectiveness of these materials as HPLC stationary phases, and reported higher retention factors than equivalent commercial columns, possibly due to the greater surface area open for interaction with the analytes.

The use of spray-drying as a technique for producing spherical Starbon® particles was thus studied. The study by Ide *et al.* (Ide *et al.*, 2011) utilised a Büchi 290 mini spray-dryer, so a feasibility study using this instrument was organised with Büchi UK. An expanded alginic acid alcogel precursor was used as the spray mixture since it has been previously reported that drying from the hydrogel state causes a collapse of the internal structure of the dried material (Budarin *et al.*, 2006).

The experiment used conditions which were designed to produce particles in the low micrometer size range. The expanded alginic acid alcogel was pumped slowly from a duran flask through to the spray nozzle by a peristaltic pump running at 7% efficiency in order to reduce the volume of spray and increase the drying efficiency of the instrument. The material was dried at 100 ^{o}C (SD-Starbon®-100), the maximum possible, considering the flash point of ethanol. In order to reduce the risk of solvent explosion, the system was coupled to a Büchi B-295 inert loop which ensured that a nitrogen-filled closed loop system was established. The material was collected in a cyclone separator. A fine powder was produced from this process. In order to test the effect of drying temperature on the properties of the powder a similar experiment was also run using a drying temperature of 80 ^{o}C (SD-Starbon®-80). SEM images of the spray dried SD-Starbon®-80 product are shown in Figure 5.3. These images show that the particles displayed a wide range of shapes and sizes (Figure 5.3 a and b), and this was also representative of the particle morphology observed for the SD-Starbon®-100 material (images not shown).

The irregularity of the particles is likely to be due to the nature of the alcogel, as the solubility of the solute in a solvent can affect particle morphology. A study by Tsapis *et al.* (Tsapis *et al.*, 2002) determined that the ratio between solvent evaporation rate (κ) and solute diffusion rate (D_i), with its value termed a "Peclet number"(P*e*), can be applied to understand the morphology of particles obtained by spray drying. The ratio is shown in equation 5.1 (Tsapis *et al.*, 2002).

$$Pe = \kappa / 8D_i \qquad \textbf{Equation 5.1}$$

P*e* < 1 means that the solute diffuses as quickly as the solvent evaporates, so that the resulting particle retains the properties of the solute in the dry state and is spherical in shape. A mixture with a P*e* > 1 means that diffusion of the solute occurs at a slower rate than droplet evaporation. This leads to a build up of the solute at the droplet surface and due to the increased viscosity of the surface, a solute shell is formed. Once the droplet is completely dried the resulting morphology, dependent on the solute and the pressure differences within the system, can vary from hollow spheres to irregular, crumpled particles (Tsapis *et al*., 2002; Vehring, 2007).

Expanded alginic acid gel is not freely soluble in ethanol; this means that the evaporation of ethanol occurs faster than the diffusional motion of the expanded alginic acid through the solvent. Therefore the alcogel mixture is likely to possess a P*e* > 1, consistent with the poor particle morphology observed. In addition to this, a study into the effect of carbohydate excipients on particle morphology highlighted that carbohydrates which formed crystalline particles were more likely to form porous spheres, whereas carbohydrates forming amorphous particles (like alginic acid) were more likely to form hollow shell particles. Crystallisation of the carbohydrate during drying was reasoned to prevent the radial distribution of the carbohydrate to the exterior of the droplet, maintaining porosity in the resulting particle (Elversson and Millqvist-Fureby, 2005).

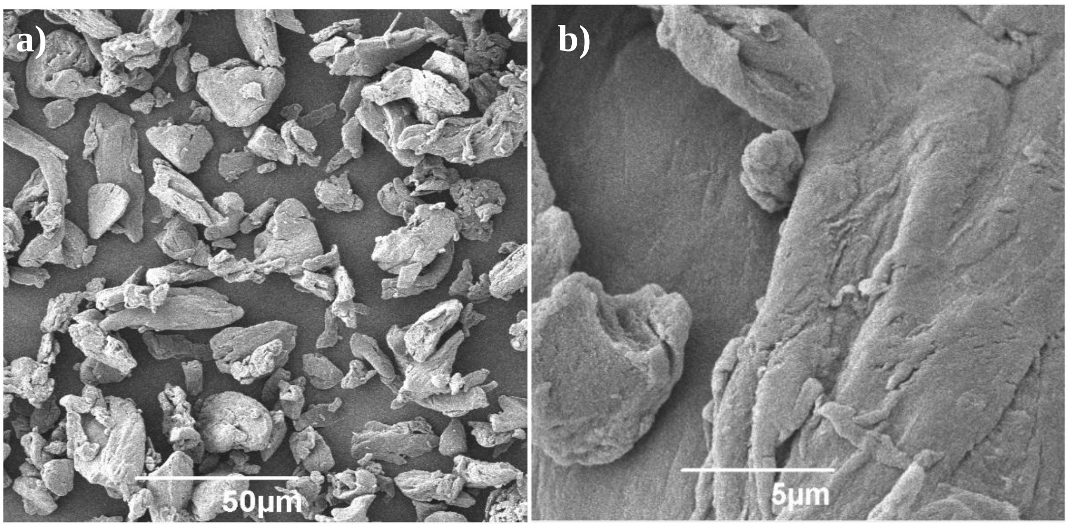

Figure 5.3: SEM images of SD-Starbon®-80 at (a) x 500 and (b) x 5000 magnification

The N_2 porosimetry data (Table 5.4) for SD-Starbon®-80 and SD-Starbon®-100 show that the sample spray dried at the higher temperature has a less porous textural properties. This could conceivably be correlated to the increase in the rate of droplet evaporation at the higher temperature, leading to more hollow and brittle particles being produced. Although the material is mesoporous, the lack of morphological control, coupled with poor solubility of alginic acid in ethanol suggests that this technique is not viable for producing dried Starbon® particles with spherical morphology for chromatographic applications.

Sample	$^{a}S_{BET}$ / m^2 g^{-1}	$^{b}PV_{des}$ / cm^3 g^{-1}	$^{c}PD_{des}$ / nm	^{d}Meso/Macro / %
SD-Starbon®-80	117	0.41	10.17	87
SD-Starbon®-100	85	0.31	9.57	87

a = BET surface area; b = BJH nitrogen desorption pore volume; c = BJH average desorption pore diameter; d = 100 – ((volume desorbed / total volume adsorbed)*100)

Table 5.4: N_2 sorption data for spray-dried expanded alginic acid

5.4.4 Sodium alginate spraying

It is widely known that water-soluble sodium alginate forms a hydrogel when cured in a solution of divalent ions, due to the greater affinity of alginate for divalent ions than for sodium ions (Grant *et al.*, 1973; Morris *et al.*, 1978; Fenoradosoa *et al.*, 2010; Papageorgiou *et al.*, 2010). Calcium alginate gel beads formed in this way are used as gelatinisers in the food industry (Draget *et al.*, 2005) as well as drug delivery vehicles (Tønnesen and Karlsen, 2002; Bulut and Sanli, 2013).

Quignard *et al.* (Quignard *et al.*, 2008) have recently shown that aerogels can be manufactured as 1.5 mm spheres (by syringing sodium alginate drop-wise into calcium chloride solution) with highly mesoporous networks (PV_{meso}: 1.16 cm^3 g^{-1}, PD: 38 nm) and large surface areas (S_{BET}: 570 m^2 g^{-1}), which are similar to the values obtained for the dried expanded alginic acid intermediate in the Starbon® process. However, although the shape and structure of such material would be ideal for chromatographic separation, a search of the literature has revealed no research into the possibility of using this material as a precursor for the development of chromatographic material.

The aim of the work described in this section was to develop and demonstrate proof-of-concept for producing mesoporous carbon spheres using a natural template process, which draws inspiration from the food and drug industry. The study was attempted to determine whether calcium alginate aerogels can be used to develop particles with spherical morphology, and that can be readily converted to PGC, whilst retaining the particle morphology.

5.4.4.1 Method development for low micron-sized alginate-derived carbon spheres

Initially, an experimental procedure modified from that used by Quignard *et al*. was attempted; 2 % sodium alginate solution was pumped by an HPLC pump through a 100 µm capillary (instead of dropping the solution by pipette) into 0.24 M calcium chloride solution which was stirred throughout (Quignard *et al.*, 2008). The hydrogel beads were allowed to "ripen" for 18 h. The solvent exchange process and supercritical drying process remained the same, although the pressure for supercritical drying was set at 85 bar rather than the 74 bar used in the literature method. SEM images of these particles after $scCO_2$ drying are seen in Figure 5.4.

Almost all of the particles were tear-drop shaped (Figure 5.4(a)) which could be a result of the limited distance between the end of the capillary and the surface of the calcium chloride solution. This distance had been reduced after observing that at large distances the sodium alginate droplet would hit the calcium chloride solution and form plate-shaped gel particles, presumably due to the impact velocity. The surface of the particles appeared highly porous with extensive porosity (Figure 5.4(b)) and this was reflected in the N_2 sorption porosimetry data (S_{BET} = 322 m^2 g^{-1}; PV_{meso} = 0.54 cm^3, PD = 13.32 nm and Meso/Macro = 78 %). Although the values for surface area and pore volume were markedly lower than those of Quignard *et al*. (Quignard *et al*., 2008) the material still clearly showed good mesoporosity, with the possibility of forming the material into the spheres which are vital for efficient chromatographic column packing.

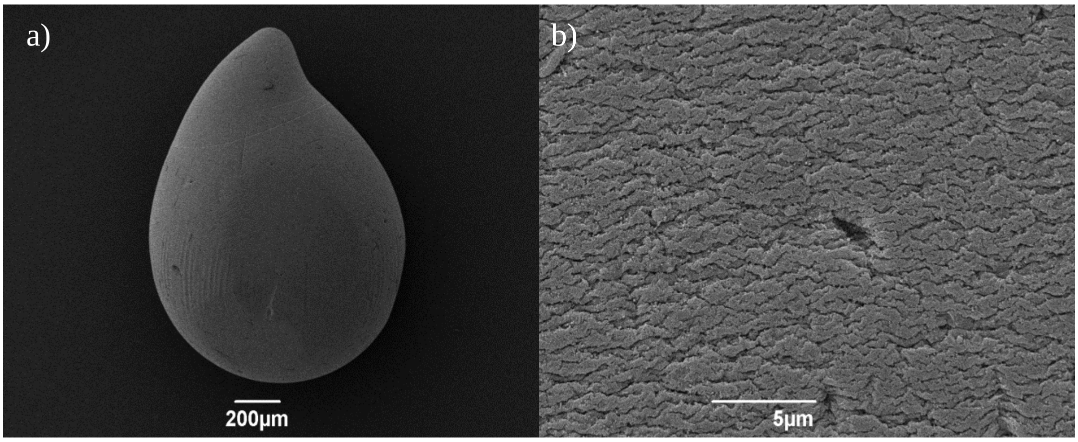

Figure 5.4: SEM images of capillary-dropped calcium alginate spheres at (a) x 55 and (b) x 5000 magnification

In order to generate particles in the low micron region a nebuliser emitter from an electrospray ionization source, used to generate a finer sodium alginate droplet spray, was studied. The experimental apparatus is shown in Figure 5.5a. The subsequent washings, solvent exchange and $scCO_2$ drying generated a porous calcium alginate aerogel. This technique yielded calcium alginate spheres of ca. 70 μm (Figure 5.5b). Pyrolysis under a nitrogen atmosphere to 800 °C at a rate of 1 K min^{-1} yielded calcium alginate-derived mesoporous carbon spheres (AMCS). Scanning electron microscopy (SEM) investigation, comparing an Starbon® pyrolysed to 800 °C with AMCS (Figure 5.6) shows images of these materials at low and medium magnification.

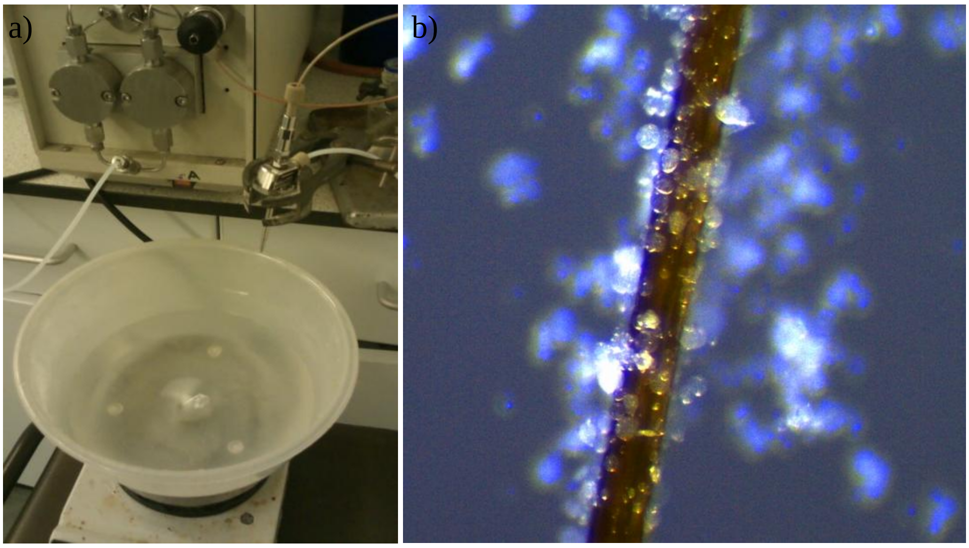

Figure 5.5: a) Photograph showing the experimental apparatus used to generate low micron range calcium alginate spheres b) Leica microscope image of calcium alginate spheres. The capillary tubing pictured has a 90 μm outer diameter.

The Starbon® images (Figure 5.6 a and b) show the highly varied particle morphology of the material and agglomeration of particles is visible. In contrast, the AMCS images (Figure 5.6 c and d) show spherical/teardrop particles with negligible agglomeration. At medium magnification, both Starbon® and AMCS show an expanded open pore structure.

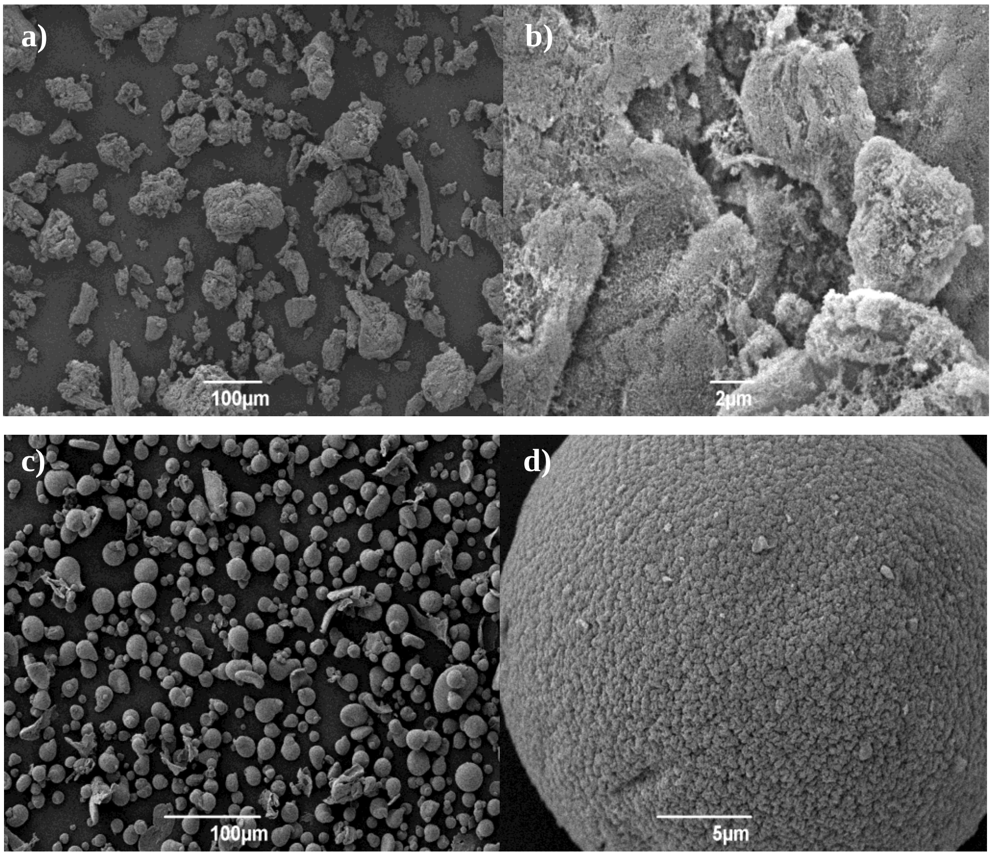

Figure 5.6: SEM images of alginic acid-derived Starbon® (a) x250 and (b) x6000 magnification and AMCS (c) x250 and (d) x5000 magnification. Both samples were pyrolysed to 800 °C.

Particle size distribution and circularity data were collected for the AMCS and Starbon® samples, as well as a commercial PGC sample (Hypersil PGC, 5 μm particle size, Hypersil, Runcorn, UK) (Table 5.5).

The data show that both Starbon® and AMCS have distinctly larger mean particle diameters than the commercial PGC material; however AMCS show a smaller and narrower distribution of particle sizes than the Starbon® material, which shows a significant improvement over Starbon® and is consistent with what was seen in the

SEM images. That AMCS had more consistently spherical particles (based on a higher circularity value and narrower standard deviation) than the commercial PGC was a surprising but pleasing result.

Sample	^{a}MPD / µm	^{b}MPD-SD / µm	^{c}MPC	^{d}MPC-SD
Commercial PGC	7.0	6.6	0.777	0.163
AMCS	23.4	9.5	0.795	0.139
Starbon®	28.6	12.6	0.594	0.162

a = Mean particle diameter; b = Mean particle diameter standard deviation; c = Mean particle circularity (1.000 = perfect sphere); d = Mean particle standard deviation

Table 5.5: Mean particle diameter and circularity data collected using a Micromeritics Particle Insight analyzer.

5.4.4.2 Investigation of calcium removal on material structural properties

Calcium ions trapped within regions of poly-G blocks in alginic acid in an arrangement described by the “egg-box” model gives rise to the structural stability of calcium alginate. The effect of calcium content on the structural properties of the AMCS precursor and AMCS materials was investigated by washing the spheres, before solvent exchange, with hydrochloric acid (HCl) at two concentrations; 0.1 M and 0.5 M. The samples were washed up to three times with the appropriate acid concentration and investigated at the aerogel precursor stage as well as after pyrolysis.

The percentage calcium content (based on total sample mass), determined by X-ray fluorescence analysis, of each sample at the precursor aerogel stage was determined (Figure 5.7). Successive washes with 0.1 M and 0.5 M HCl reduced the material’s calcium content, with 0.5 M HCl removing calcium to a greater extent after three washes than 0.1 M HCl (0.0095% as opposed to 0.123% after 3 washes with 0.1 M HCl). The greatest drop in calcium content occurred at the first wash, accounting for a ca. 82% (7.56% to 1.32%) and ca. 96% (7.56% to 0.317%) reduction of calcium using the 0.1 M and 0.5 M acid respectively, when compared to the unwashed material.

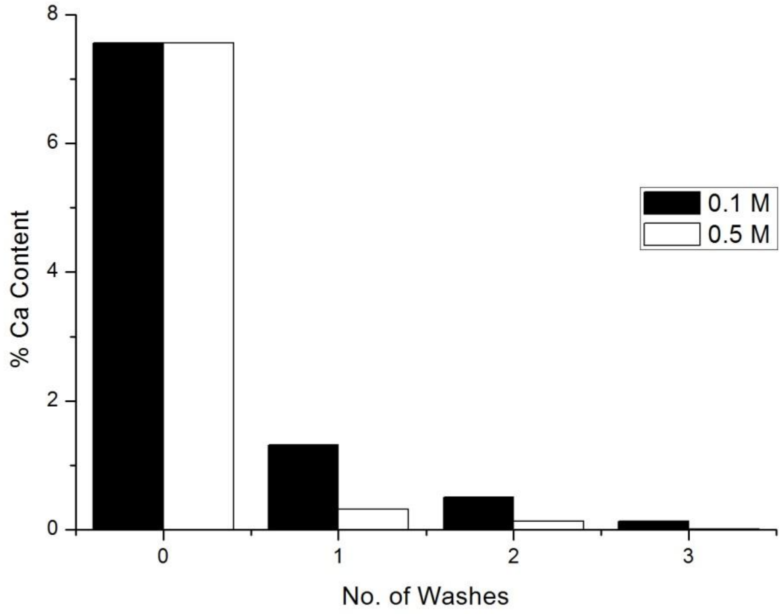

Figure 5.7: Graph plotting the total % Ca content (based on total sample mass), determined by X-ray fluorescence analysis, in the materials after 0, 1, 2 or 3 washes with hydrochloric acid at either 0.1 M or 0.5 M.

Fourier-transform infrared (FT-IR) spectroscopy analysis of the unwashed precursor yields a spectrum that is identical to that of a commercial calcium alginate standard (Figure 5.8(a)). With increasing numbers of washes (Figure 5.8(b)), there is a reduction in intensity of the bands at 1595 cm^{-1} (assigned to the carboxylate anion (COO^{-}) asymmetric stretch vibration (Gómez-Ordóñez and Rupérez, 2011)) and 1418 cm^{-1} (assigned to a combination of the C-OH deformation vibration and carboxylate symmetric stretch vibration) coupled with an increase in the band at 1733 cm^{-1} (assigned as a protonated carboxylic acid vibration); these observations are consistent with the progressive removal of calcium as the number of acid washes increases. These transitions appear to correlate with those reported by Huang *et al*. for the acid-washing of sodium alginate (Huang *et al*., 1999). The FT-IR spectra of the samples washed with 0.5 M HCl were identical to the spectrum of the 0.1 M HCl sample washed three times.

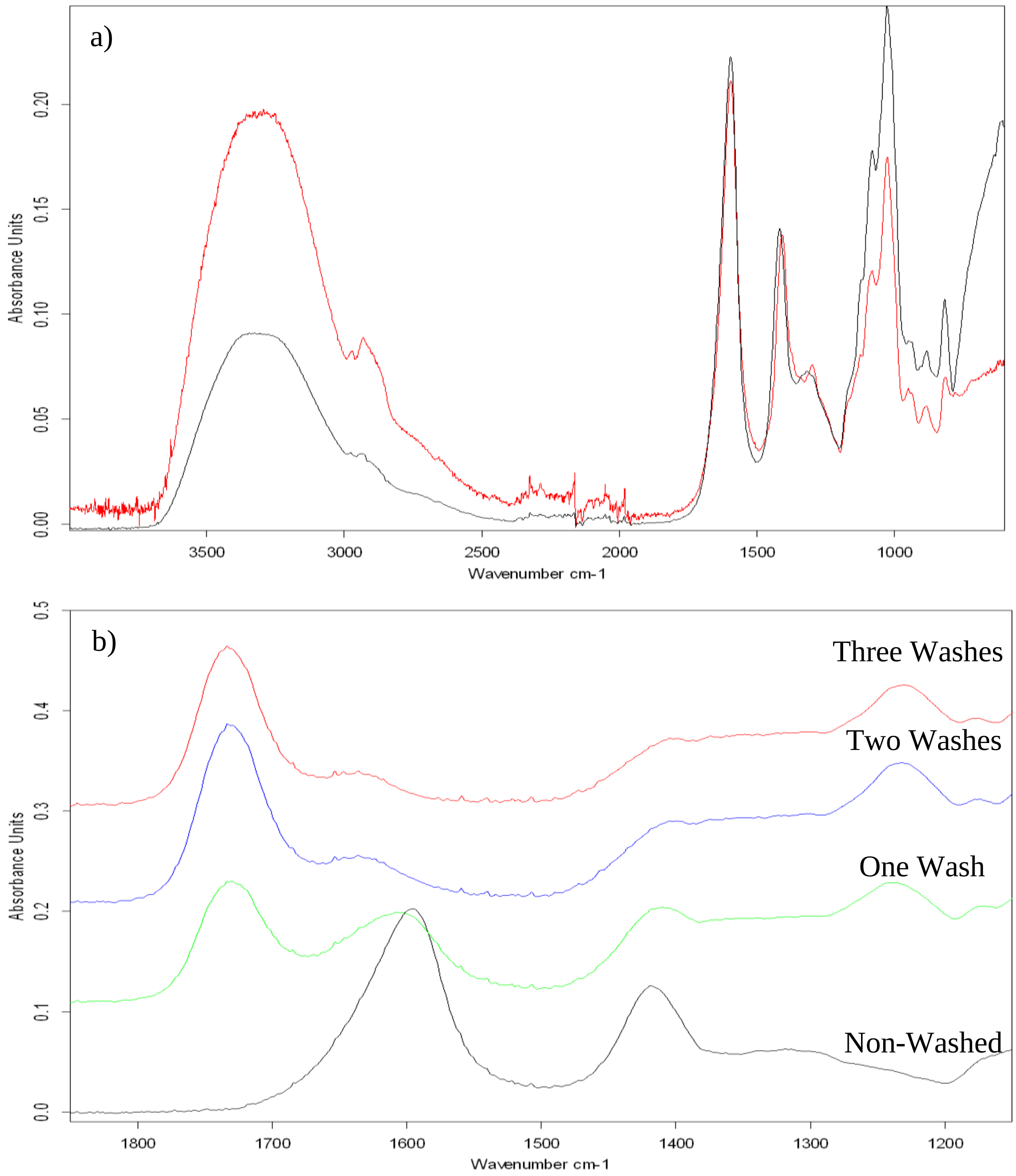

Figure 5.8: (a) FT-IR spectra of calcium alginate aerogel precursor (black) and a commercial calcium alginate standard (red) (b) FT-IR spectra of calcium alginate aerogel precursor after incremental washings with 0.1 M HCl

N_2 adsorption porosimetry was used to assess the effect of calcium removal on the pore network of the aerogel precursor (Table 5.6). All samples present highly mesoporous networks (average pore diameters within the 2–50 nm mesopore range, as defined by IUPAC (Everett, 1972)) with deep open access demonstrated by large pore volumes between 2.80 and 4.10 $cm^3\ g^{-1}$, equivalent to ≥ 95 % of the total pore volume.

The effect of calcium content is marked with regards to average pore diameter and to a lesser extent surface area, both showing a downward trend as the number of washes increases for both concentrations of HCl. It is proposed that the observed trends are due to the increased disorder of the poly-G regions within the gel as a result of calcium removal, which compromises the structural integrity of the resultant gel.

Type	Conc. of HCl / M	No. of Washes	$^{a}S_{BET}$ / $m^2\ g^{-1}$	$^{b}PV_{des}$ / $cm^3\ g^{-1}$	^{c}PD / nm	^{d}Meso/Macro / %
Aerogel Precursor	Unwashed		404	4.01	35.60	96
	0.1	1	343	2.93	34.91	95
	0.1	2	311	3.74	32.13	96
	0.1	3	295	2.83	27.41	96
	0.5	1	311	3.24	34.87	96
	0.5	2	289	2.91	31.68	96
	0.5	3	295	3.33	30.33	96
AMCS	Unwashed		561	1.20	12.49	81
	0.1	1	515	2.23	19.80	90
	0.1	2	498	0.71	15.94	74
	0.1	3	481	0.36	15.22	59
	0.5	1	431	0.97	16.84	81
	0.5	2	475	0.40	13.52	61
	0.5	3	415	0.02	4.52	7

a = BET surface area; b = BJH nitrogen desorption data; c = BJH Average Desorption Pore Diameter; d = 100 – ((Volume Desorbed/Total Volume Adsorbed)*100)

Table 5.6: N_2 sorption data for aerogel precursor and resulting AMCS material types

Further investigation into the effect of calcium ion removal on the structural properties of the AMCS was performed. The AMCS samples were prepared by pyrolysis of the precursor materials under a nitrogen atmosphere to 800 °C.

Table 5.6 summarizes the N_2 adsorption porosimetry data for the all the AMCS produced. Comparing against the data for the precursor material, there are clearer and more marked differences between the samples with the trends reflecting that of the relative calcium content before pyrolysis. Interestingly, the unwashed material seems anomalous, with the 0.1 M once washed material having the greatest pore volume and widest pore diameter. It is unclear why this is the case, although it can be speculated that the high concentration of calcium (hence high rigidity of the poly-G regions of the precursor material) reduces the ability of the spheres to expand and contract during pyrolysis. As a consequence, the release of volatiles (at its most pronounced during the decarboxylation of the uronic acid residues) may trigger greater structural collapse than would have been predicted in the unwashed material.

Of additional interest is the 0.5 M three times washed sample, which yielded to an almost complete breakdown of mesoporous structure and therefore highlights that there is a minimum calcium content required in the alginate polymer in order to retain material rigidity during pyrolysis.

The knowledge of calcium content effect on the pore structure of these materials, coupled with the observed changes in surface chemistry during pyrolysis enhances the tuning capabilities of AMCS, extending the application potential of these materials beyond chromatographic stationary phase production (White *et al*., 2010).

5.4.4.3 Application of AMCS as a chromatographic stationary phase

In order to investigate the potential of AMCS as a chromatographic stationary phase, a 100 mm x 4.6 mm i.d. HPLC column was packed with 0.1 M-once washed AMCS using a high pressure column packer (denoted AMCS-LC-MS). All column packing was performed by Ken Butchart at Fortis Technologies, Neston, UK. Separation of a standard solution of a mixture of the polar analytes glucose, sucrose, raffinose, stachyose and verbascose, and the sugar alcohols mannitol and maltitol (50 $\mu g\ mL^{-1}$ of each analyte) was attempted using the method conditions given in Chapter 2 (Section 2.3.5) and the results compared with those from a column high pressure-packed with Starbon® material (denoted Starbon®-LC-MS) and a commercial PGC column (denoted PGC-LC-MS), as attempted previously by White *et al*. (White *et al*., 2010). The retention times of the seven analytes from each column are summarized in Table 5.7, whilst the extracted ion chromatograms for each analyte (detected as the formylated molecule $[M+HCOO]^-$) obtained from the Starbon®-LC-MS, AMCS-LC-MS and PGC-LC-MS systems are shown as Figure 5.9(a), (b) and (c), respectively.

Carbohydrate standard	Observed species / *m/z*	Starbon® t_R / min	AMCS t_R / min	PGC t_R / min
Glucose	225 $[M+HCOO]^-$	2.6	4.9	3.9
Mannitol	227 $[M+HCOO]^-$	2.7	5.1	3.5
Sucrose	387 $[M+HCOO]^-$	8.6	8.4	8.6
Maltitol	389 $[M+HCOO]^-$	8.5	8.2	8.5
Raffinose	549 $[M+HCOO]^-$	8.6	8.8	9.2
Stachyose	711 $[M+HCOO]^-$	8.6	8.8	9.1
Verbascose	873 $[M+HCOO]^-$	8.7	8.9	9.2

Table 5.7: Nominal *m/z* values and retention times obtained for standard compounds using the AMCS-LC-MS, Starbon®-LC-MS and PGC-LC-MS systems.

The seven analytes elute in a similar order from the three systems, with maltitol eluting marginally earlier than sucrose, and raffinose, stachyose and verbascose co-eluting. The spread of retention times for these five analytes is narrower for the Starbon®-LC-MS system (0.2 min) than for the other two systems (0.7 min), which could indicate limited resolving power for the Starbon®-LC-MS system. The largest variation in retention times over the three systems are seen for glucose and mannitol, with the AMCS-LC-MS system (4.9 min and 5.1 min respectively) retaining these analytes longer than the PGC-LC-MS (3.9 min and 3.5 min) and Starbon®-LC-MS (2.6 min and 2.7 min) systems. A combination of stationary phase packing efficiency of the Starbon® material and the presence of highly adsorbent micropores in the AMCS material may explain this variation. Since glucose in particular is a challenging analyte to retain, even on PGC, this observation could indicate a potential functional advantage of the new AMCS material over commercial PGC.

The AMCS-LC-MS system displays Gaussian peak shapes. with slight tailing similar to that observed from the PGC-LC-MS system, whereas the Starbon®-LC-MS peak shape is poorer, with several analytes eluting with shouldered fronting (e.g. sucrose and maltitol) as well as much broader baseline peak widths. The peak shapes for glucose and mannitol are much sharper from the PGC-LC-MS system than from the AMCS-LC-MS and Starbon®-LC-MS systems, with some resolution of the glucose α and β anomers observed.

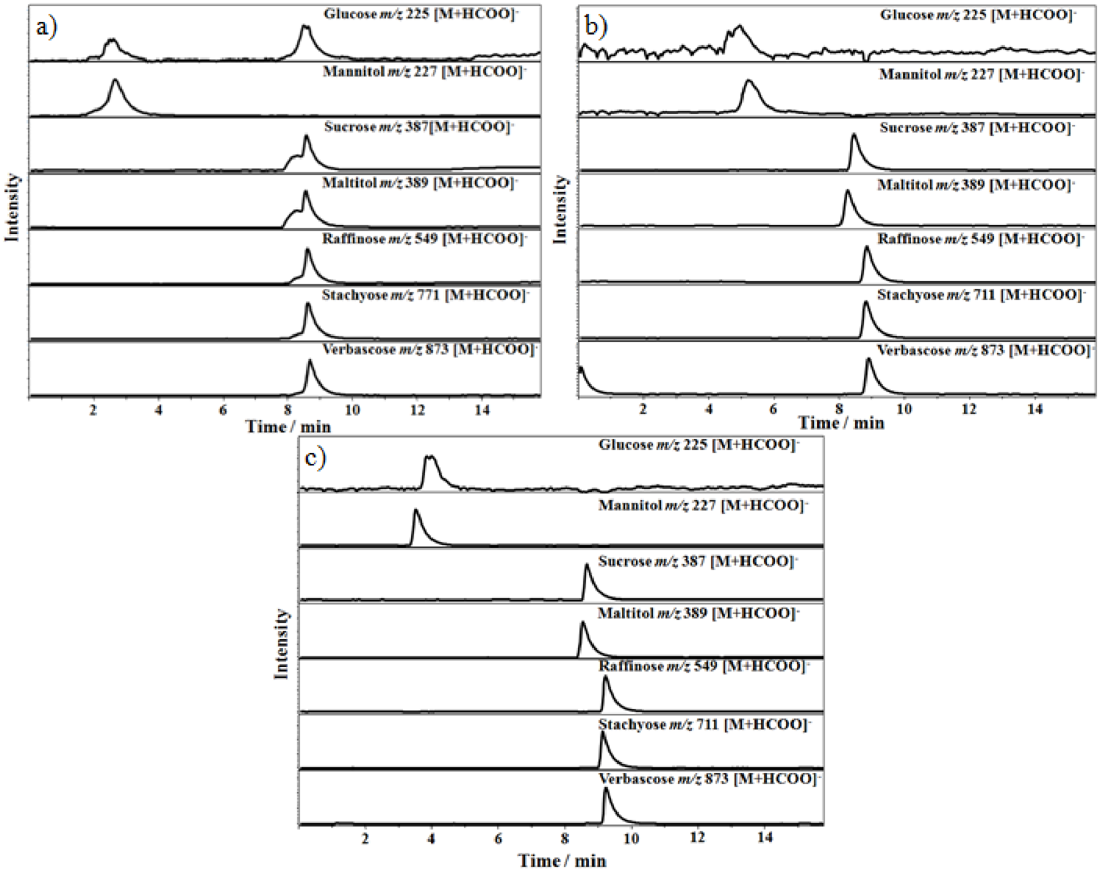

Figure 5.9: Extracted ion chromatograms of 50 μg mL^{-1} standard solution of a mixture of glucose, mannitol, sucrose, maltitol, raffinose, stachyose and verbascose obtained on the (a) Starbon®-LC-MS, (b) AMCS-LC-MS and (c) PGC-LC-MS system

In order to determine the efficiency of the three systems used in this work Van Deemter curves (Figure 5.10) were constructed based on the retention time and peak width (based on FWHM) values of a 50 μg mL^{-1} sucrose standard eluting under isocratic conditions at various flow rates. Van Deemter curves plot theoretical plate height against flow rate and give an insight into the efficiency of a column i.e the number of theoretical plates.

The curve for the Starbon®-LC-MS system starts at a much larger plate height value (0.263 mm) than the other two systems (0.043 mm and 0.026 mm for the AMCS-LC-MS and PGC-LC-MS systems respectively). The Starbon®-LC-MS curve appears to be level at this stage which defines this columns maximum efficiency. Eddy diffusion is not affected by mobile phase velocity as flow pathlength remains the same throughout and represents the minimum plate height that can be attained. This implies that eddy diffusion contributes more to peak broadening in the Starbon®-LC-MS than in the AMCS-LC-MS and PGC-LC-MS systems. This is likely to be the result of the wide particle size distribution, which includes fines (particles below 1µm), and poor particle shape limiting the ability to efficiently pack this material into a column. This fits well with the poor peak shape and resolution observed in the chromatography. At low flows, the AMCS-LC-MS system has a plate height value which closely resembles that of the PGC-LC-MS system indicating that the packing efficiency is much better with this material than the Starbon®. The slight difference between the value for the PGC and the AMCS is probably a result of the larger particle sizes in the AMCS-LC-MS system, which will leave larger interstitial gaps between stationary phase particles.

In terms of the steepness in the curvature of the lines, the AMCS-LC-MS data resembles that of the Starbon®-LC-MS system, and contrasts with the flatter trend for the PGC-LC-MS system. This indicates that the PGC-LC-MS system is affected by the mass transfer effect to a much lesser extent than the other two systems, which could be due to the templated mesopore structure of commercial PGC which means the analyte/stationary phase interaction will be consistent throughout the material. In contrast, the AMCS and Starbon® materials are predominantly mesoporous with some microporosity. It may be that interaction with the more strongly adsorbing micropores could lead to peak broadening at higher flow rates. In addition, the larger average particle diameters of the AMCS and Starbon® materials in comparison to PGC mean that pathlengths through the particles are longer, which lengthens the time it takes to establish an equilibrium between the analyte and the mobile phase into which the analyte would be transferred.

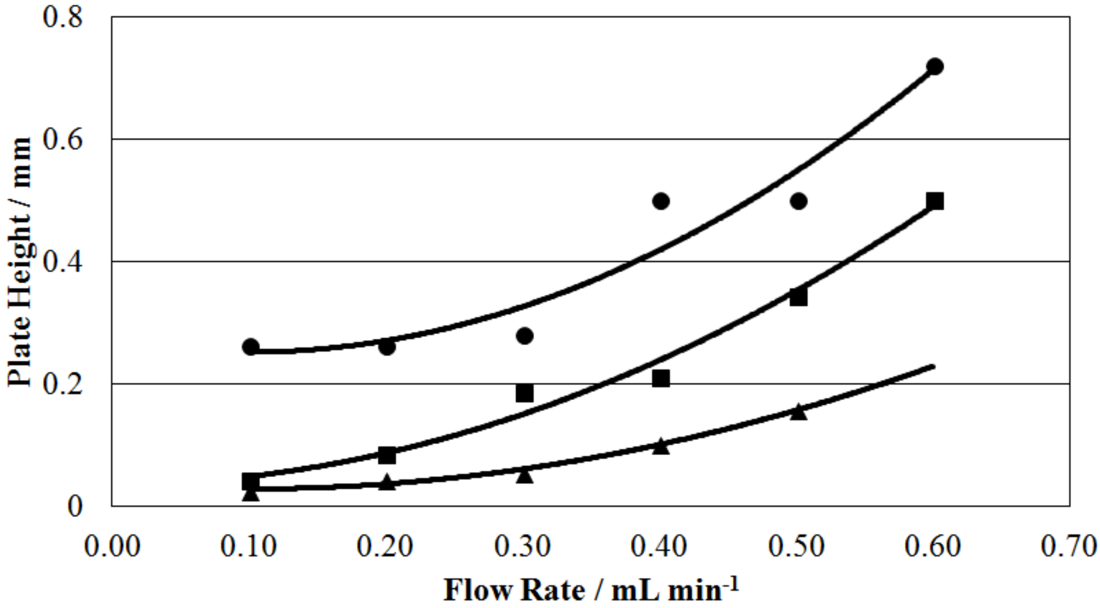

Figure 5.10: Van Deemter curves for a 50 µg mL^{-1} sucrose standard solution eluting at various flow rates from the AMCS-LC-MS (■),Starbon®-LC-MS (●) and PGC-LC-MS (▲) systems.

5.5 Conclusions

In summary, a number of techniques were investigated in order to develop a synthesis method for Starbon® which would achieve spherical particle morphology and average particle sizes at 5-10 µm, whilst retaining high mesoporosity.

Hand-milling was found to improve particle morphology, but the time required to reduce the average particle size meant this approach was not feasible as a long-term solution. Mechanical ball-milling improved both particle morphology and particle size, but the mesoporosity of the resulting materials was lost. Spray-drying retained mesoporosity, but particle morphology and size were not improved over the current Starbon® synthesis.

The preparation of mesoporous carbon spheres utilizing an inexpensive and readily available biomass-derived starting material (sodium alginate), natural solvents (water, ethanol and supercritical CO_2 ($scCO_2$)) and nebulising spray technology was demonstrated. Pyrolysis of the precursor under an inert atmosphere yielded, for the first time, porous carbonaceous spheres via a "natural" templating process made possible by the structural properties of the alginate precursor. By controlling the calcium content of the precursor a new method to tune material structure has been described which extends the remit of possible applications for this type of carbon.

The application of this material to chromatography and comparison of its performance with that of a commercial PGC column and a column packed with Starbon® material has been demonstrated, with the separation of a standard carbohydrate mixture. The performance of the mesoporous carbon spheres was found to more closely resemble that of commercial PGC than of Starbon®, and whilst further reduction of particle size is required, they represent a promising step forward in the development of a more environmentally friendly, biomass-derived carbon stationary phase.

Chapter 6

Investigation into the structure of alginic acid-derived mesoporous carbons by microscopy and spectroscopy

The work described in this chapter has been published in:

Investigating the structure of biomass-derived non-graphitizing mesoporous carbons by electron energy loss spectroscopy in the transmission electron microscope and X-ray photoelectron spectroscopy

***Carbon*, 67 (2014) 514-524**

Andrew S. Marriott[1,2,3], Andrew J. Hunt[1,2], Ed Bergström[1,3], Karen Wilson[4], Vitaliy L. Budarin[1,2], Jane Thomas-Oates[1,3], James H. Clark[1,2], Rik Brydson[5]

[1] Department of Chemistry, University of York, York, UK
[2]Green Chemistry Centre of Excellence, University of York, York, UK
[3]Centre of Excellence in Mass Spectrometry, University of York, York, UK
[4]School of Chemistry, Cardiff University, Cardiff, UK
[5]Institute for Materials Research, School of Process, Environmental and Materials Engineering (SPEME), University of Leeds, Leeds, UK

6.1 Introduction

The work described in chapter 5 showed how HPLC columns packed with both alginic acid-derived Starbon® and AMCS materials offered similar chromatographic separation of a series of carbohydrates to that of a commercial PGC column. This result is surprising given the differences between the synthesis pathways of the biomass-derived porous carbons and PGC; in particular, regarding the carbonising precursor type and final pyrolysis temperatures used. An investigation analysing the carbon microstructure of both Starbon® and AMCS was proposed in order to understand how this microstructure relates to that present in PGC.

The distinction of a carbon material as either 'graphitizing' or 'non-graphitizing' was first made by Rosalind Franklin in 1951 and is dependent on whether or not, after high-temperature heat treatment, the materials forms crystallite graphite (graphitizing) or not (non-graphitizing) (Franklin, 1951). The compact pre-orientation of layer-planes at low temperature in high density graphitizing carbons, derived from aromatic hydrocarbon systems (e.g. pitches and coal tars) or chemical vapour deposition of hydrocarbon gases, enables crystallite growth (Franklin, 1951; Daniels *et al*., 2007). In comparison, non-graphitizing carbons (derived from coals, biomass and organic by-products from agriculture and industry - (McEnaney, 1988)) are low density materials, which form cross-linked layer-planes. These cross-linked planes (also traditionally thought responsible for the porosity in these materials, such as that found in microporous carbons (McEnaney, 1988) and carbogenic molecular sieves (Foley, 1995)), are unable to rearrange and graphite crystal growth is inhibited (Franklin, 1951). A study by Knox *et al*. (Knox *et al*., 1986) on porous graphitic carbon (PGC) described this material as a non-graphitizing carbon, made up of two-dimensional "turbostratic" graphite; “turbostratic” graphite was first described by Warren in graphitised carbon blacks (Warren, 1941).

The carbon structure present in alginic acid-derived Starbon® has been studied previously. However, the characterisation techniques used have generally been of an indirect nature, identifying only that the materials show extended aromaticity (White *et al*., 2010; Parker *et al*., 2012). Thus there is a need to use a method that allows the direct comparison of the two-dimensional graphite structure of a commercial PGC material, with the amorphous carbon structure (typical of a carbon prepared from a biomass precursor) of alginic acid-derived Starbon® material, in order to understand why alginic acid-derived Starbon® shows retention similar to that on PGC. Amorphous carbons may contain various proportions of sp^3, sp^2 and sp^1 carbons, along with potential hetero-atom inclusions such as oxygen, nitrogen or sulfur, in the carbon network depending on the precursor source. The inherent poor crystallinity of amorphous carbons makes these materials difficult to analyse by general methods e.g. X-ray diffraction. Alternative techniques have been adopted including ^{13}C nuclear magnetic resonance (NMR), (UV) Raman spectroscopy and electron energy loss spectroscopy (EELS) in the transmission electron microscope (TEM) (Zhang *et al*., 2011). However, NMR spectra can be affected by the conductance of aromatic carbons at high pyrolysis temperatures. The disadvantage of Raman comes from weak sp^3 scattering (Robertson, 1991).

EELS-TEM is an analytical technique that involves the use of fast incident electrons (100-400 keV) to impart momentum and energy to electrons in a material; the subsequent loss of this energy creates the detected signal (Daniels *et al*., 2003). Of particular interest for the analysis of carbon materials, the appearance, position and intensity of features in the carbon K-edge region (280-300 eV) of the EELS spectrum, provide information on the bonding type and extent of sp^2/sp^3 hybridisation in the carbon structure (Papworth *et al*., 2000). The characterisation by EELS of a material’s microstructure can enhance our understanding of its effects on the material’s properties at the macroscopic level (Zhang *et al*., 2011). EELS has already been applied to various carbon material types, including graphite (Batson, 1993), carbon thin films (Papworth *et al*., 2000) and carbon nanotubes (Henrard *et al*., 1999). More recently, model series of graphitizing and non-graphitizing carbons were analysed by EELS and included a method to identify and quantify fullerene content in the carbon samples (Daniels *et al*., 2007; Zhang *et al*., 2011). In addition, the relaxation of the excited electrons generates a characteristic amount of energy, which can be detected by energy dispersive X-ray (EDX) analysis to determine the spatially localised elemental composition of a material (Daniels *et al*., 2007). To date, there have been no EELS studies reported based on the analysis of biomass-derived carbon materials.

Although EDX analysis can determine the quantitative atomic composition of a material feature (e.g. nanoparticle) it is unable to determine the chemical environment of these atoms; X-ray photoelectron spectroscopy (XPS) is a surface analysis technique which can provide this information. XPS uses X-rays to eject from an atom a photoelectron, the kinetic energy of which is dependent on the incident radiation and correlated to the binding energy of the electron in the orbital of the atom (Winograd and Gaarenstroom, 1980). Spectrum peaks associated with photoelectrons, emitted from core-level electrons, are sharper than those from valence-shell electrons. As such, the localisation of the core electrons means that chemical environments can be assigned to specific atoms. For example, with regards to carbon materials, core-level XPS of carbon (C 1*s*) has been applied to determine sp^2/sp^3 hybridisation ratios (Díaz *et al*., 1996; Haerle *et al*., 2001).

The purpose of the work described in this chapter is to characterise the microstructure and chemical composition of alginic acid-derived Starbon® and AMCS, applying TEM imaging and diffraction techniques combined with compositional analysis using EDX and electron energy loss spectroscopy (EELS) together with a semi-quantitative analysis of the EELS carbon K-edge, to determine both the fraction of sp^2-bonded carbon atoms and the degree of fullerene character (Zhang *et al*., 2011). In addition, XPS analysis of the calcium (Ca 2*p*) and carbon (C 1*s*) components of the alginic acid-based samples has been applied and is discussed. Two alginic acid-derived Starbon® samples were studied here: one pyrolysed to 1000 °C (Starbon® A1000) and the other to 800 °C (Starbon® A800). These samples represent respectively materials prepared using the same pyrolysis temperature as White *et al*. (White *et al*., 2010) and the pyrolysis temperature more recently favoured for the preparation of Starbon® material (Parker *et al*., 2012; this thesis). This data is directly compared with similar data for a commercial PGC material. Coupled to this, the research into morphology control (Chapter 5) has highlighted the effect that calcium ions play in the structural properties of AMCS, where microporosity of the material was observed to increase as calcium levels decreased. To date, no analysis of the effect of calcium removal on the microstructure of these materials has been attempted. Two different AMCS samples were studied here; an unwashed sample (AMCS-UW; the sample has not undergone an acid-wash step to remove bound calcium ions), and an acid-washed sample (AMCS-W; washed using 0.1 M HCl).

6.2 Aims

The aim of the study described in this chapter was to investigate the chemical microstructure of alginic acid-derived Starbon® and AMCS materials. EELS-TEM, EDX and XPS techniques were performed. Analysis of the distribution and composition of the calcium species in the two materials was also attempted. This work was carried out in collaboration with Professor Rik Brydson who performed all EELS-TEM and EDX operations (LENNF, University of Leeds, UK) and Dr Karen Wilson who performed XPS analysis (Cardiff University, UK). The general aims of the work in this chapter are summarised as follows:

- Collect high resolution TEM images of a commercial PGC and the alginic acid-derived Starbon® and AMCS materials.
- Analyse the EELS spectra of all three material types, collected at the carbon K-edge, to generate information on ratios of carbon hybridisation and percentage fullerene character.
- Use EDX and XPS to determine the elemental composition of the alginic acid-derived Starbon® and AMCS materials.
- Collect and analyse core-level XPS spectra of the C 1*s* and Ca 2*p* signals to determine the chemical environments of each atom type present in the alginic acid-derived Starbon® and AMCS materials.

6.3 Experimental

6.3.1 Chemicals

Alginic acid from brown algae and sodium alginate were purchased from Sigma (Poole, UK). Commercial PGC was purchased from Hypersil (Runcorn, UK). Calcium chloride and all solvents were purchased from Fisher (Fisher Scientific, Loughborough, UK).

6.3.2 Alginic acid-derived Starbon® precursor synthesis

Alginic acid from brown algae (Sigma) was gelatinised in distilled water: a suspension of the polysaccharide (1 g in 20 mL water) was stirred for two hours at 90 °C. The resulting gel was then retrograded at 5 °C for 24 h. The water was exchanged for ethanol and the resulting alcogel dried in supercritical CO_2 ($scCO_2$). Drying was conducted using a Thar SFE-500 supercritical extractor heated to 40 °C and held at a pressure of 120 Bar for 2 h under dynamic flow conditions (40 g min^{-1} CO_2). The extractor was subsequently allowed to depressurise over a period of 12 h.

6.3.3 Preparation of AMCS precursor

Sodium alginate (Sigma-Aldrich) was mixed in deionised water (1 g in 50 mL water) to produce a viscous solution. The solution was passed through an electrospray ionization emitter source that had been detached from the mass spectrometer, at a flow rate of 1 mL/min using a constametric 3200 solvent delivery system (LDC Analytical). The solution was nebulized using 9 psi air, and was sprayed into a constantly-stirred 0.24 M solution calcium chloride and cured in solution for 24 h to prepare hydrogel spheres of calcium alginate. The hydrogel spheres were transferred into deionised water and washed. At this stage, the AMCS-W sample spheres were acid-washed using hydrochloric acid (0.1 M or 0.5 M), as required, to reduce the calcium content of the material. The removal of water was performed by solvent exchange with ethanol (a lower surface tension solvent) using a method reported previously (Robitzer *et al.*, 2011b). The excess solvent was removed from the resulting alcogel by Büchner filtration before the material was dried by $scCO_2$. The drying was performed using a Thar SFE-500 supercritical extractor heated to 40 °C at a pressure of 120 Bar for 4 h under dynamic flow conditions (40 g min^{-1} CO_2). The extractor was depressurized slowly over 12 h.

6.3.4 Preparation of carbonaceous alginic acid-derived Starbon®/AMCS material

Starbon® and AMCS precursors were pyrolysed by heating under a N_2 atmosphere (N_2 flow: 150 mL min^{-1}, BOC) in a ceramic furnace which contained a quartz round bottomed flask. All samples were pyrolysed to either 800 °C (Starbon® A800, AMCS-UW and AMCS-W) or 1000 °C (Starbon® A1000) at a rate of 1 K min^{-1} followed by a hold of 20 min.

6.3.5 N_2 sorption porosimetry

N_2 porosimetry was performed on a Micromeritics Tristar volumetric apparatus at 77 K. The samples were outgassed at 160 °C for 8 h under atmospheric pressure before analysis.

6.3.6 Transmission electron microscopy (TEM)

TEM characterisation was carried out with a FEI Supertwin CM200 thermally assisted field emission gun transmission electron microscope operated at 197 keV (point resolution 0.24 nm) equipped with an ultra thin window Oxford Instruments energy dispersive X-ray (EDX) detector, and running ISIS software and Gatan (GIF200) EELS imaging filter. TEM samples were prepared by grinding and ultrasonically dispersing the powders in methanol, one drop of the dispersion was deposited onto a copper grid (400 mesh) covered by a holey carbon-coated film (Agar Scientific), and the sample was dried in air for about 15-20 minutes. All EELS spectra were collected in diffraction mode from areas some 180 nm in diameter; core loss spectra were all collected using ‘magic’ collection angle conditions for which spectra are crystallographically orientation independent (Daniels *et al*., 2003). Carbon K-edge spectra were processed and fitted using the Digital Micrograph software package (Gatan). Fitting and analysis of the EELS carbon K-edge was performed using the approach described by Zhang *et al*. (Zhang *et al*., 2011). All TEM and EELS analysis was carried out by Professor Rik Brydson (LENNF Facility, University of Leeds, UK).

6.3.7 X-ray photoelectron spectroscopy

X-ray photoelectron spectroscopy (XPS) were performed on a Kratos AXIS HSi X-ray photoelectron spectrometer equipped with a monochromatic Mg Kα X-ray source (energy 1253.6 eV) and a charge neutralisation gun. Spectra were recorded at an analyzer pass energy of 20 eV. Spectra were energy referenced to the C 1*s* photoelectron peak at 284.6 eV, with quantification performed using CASA-XPS 2.3.15 following Shirley background subtraction. Sensitivity factors for C 1*s* (0.318), Ca 2*p* (1.95), N 1*s* (0.505) and O 1*s* (0.736) were used to correct the signal intensities and quantify the surface composition. Peak fitting for Ca and carbohydrate features was performed using a 30:70 Gaussian-Lorentzian peak shape, whilst deconvolution of graphitic-like sample data required an asymmetric Doniach

Sunjic line shape. Spectra were fitted with the minimum number of components required to provide a good envelope, with full width half maxima (FWHM) kept fixed within each class of material. Typical FWHM values were 1.5-1.7 eV for Ca 2*p*; while for the C 1*s*, FWHM were 2.5 eV for the AMCS and Starbon® precursors and 1.5 eV for the pyrolysed products. Binding energies for components were chosen using reference data from the NIST XPS database (http://srdata.nist.gov/xps/). All XPS analysis was carried out by Dr Karen Wilson (Cardiff University, UK).

6.4 Results and discussion

6.4.1 N_2 sorption porosimetry

Table 6.1 summarises the surface area and pore structure characteristics of the samples as determined by N_2 sorption porosimetry. All samples are predominantly mesoporous, with the commercial PGC material having the highest mesopore content at 94 %. Pore diameter is well within the mesopore range for all samples, although the commercial PGC material had a narrower pore size distribution (not shown). This is to be expected, as this material is synthesised using a hard-templating route, for which a template of a specified pore size is used (West *et al.*, 2010). The alginic acid-based samples have greater surface area than the commercial PGC material as well as larger pore volumes, although there is significant variation among these samples. This is to be expected because of the expanded nature of these materials, arising from the natural-template route used to synthesise these materials.

Sample	$^{a}SA_{BET}$ / $m^2\ g^{-1}$	$^{b}PV_{des}$ / $cm^3\ g^{-1}$	$^{c}PD_{des}$ / nm	^{d}Meso. / %
Commercial PGC	101	0.67	18.35	94
Starbon® A800	396	1.78	21.04	91
Starbon® A1000	605	0.88	13.09	72
AMCS-UW	562	1.20	12.49	81
AMCS-W	515	2.23	19.80	90

a = BET surface area; *b* = BJH desorption pore volume; *c* = BJH desorption pore diameter; *d* = Percentage mesoporosity

Table 6.1: N_2 sorption data for commercial PGC, AMCS and Starbon® samples

6.4.2 Transmission electron microscopy (TEM)

6.4.2.1 High resolution TEM

Figure 1 shows high resolution transmission electron micrographs of: commercial PGC (Figure 6.1(a) and (b)); Starbon® A800 (Figure 6.1(c) and (d)); Starbon® A1000 (Figure 6.1(e) and (f)); AMCS-UW (Figure 6.1(g) and (h)) and AMCS-W (Figure 6.1(i) and (j)). These images are representative of the microstructures observed within these materials at both low and high magnifications.

Commercial PGC exhibits a high proportion of disordered, closed loop structures of graphitic layer stacks exhibiting both rounded (i.e smooth) curvature and also very angular curvature (Figure 6.1 (a) and (b)). The graphitic stacks (consisting of (002) planes) are ca. 1-2 nm thick (3 to 6 graphene layers) and display a range of widths varying between 5 and 15 nm. Low magnification micrographs (Figure 6.1(a)) show the enclosed pore structure but also reveal that no long-range order graphitization exists at the macroscopic scale. These images are consistent with those reported by Zhang *et al*. (Zhang *et al*., 2011) for non-graphitizing carbons pyrolysed above 2000 °C, and is consistent with the literature describing PGC synthesis, in which temperatures in excess of 2000 °C are required to reduce the micropore content (West *et al*., 2010). Interestingly, there is also evidence of smaller, quasi-flat but highly-aligned carbon layers which appear similar to those described by Harris *et al*. for low temperature-pyrolysed graphitizing microporous carbons, derived from anthracene (Harris *et al*., 2000).

In the Starbon® A800 sample, there is only minimal ordering of (002) graphitic planes, limited to 2-3 aligned layers at most (Figure 6.1(c)). A high degree of rounded layer curvature is also evident, which indicates a large degree of fullerene-like character (i.e. the presence of carbon pentagons and heptagons in addition to normal graphitic hexagons) which results in a very closed-loop structure. At low magnification, the material appears particulate in nature and the images show the porous, irregular-shaped nature of the alginic acid-derived Starbon® particles.

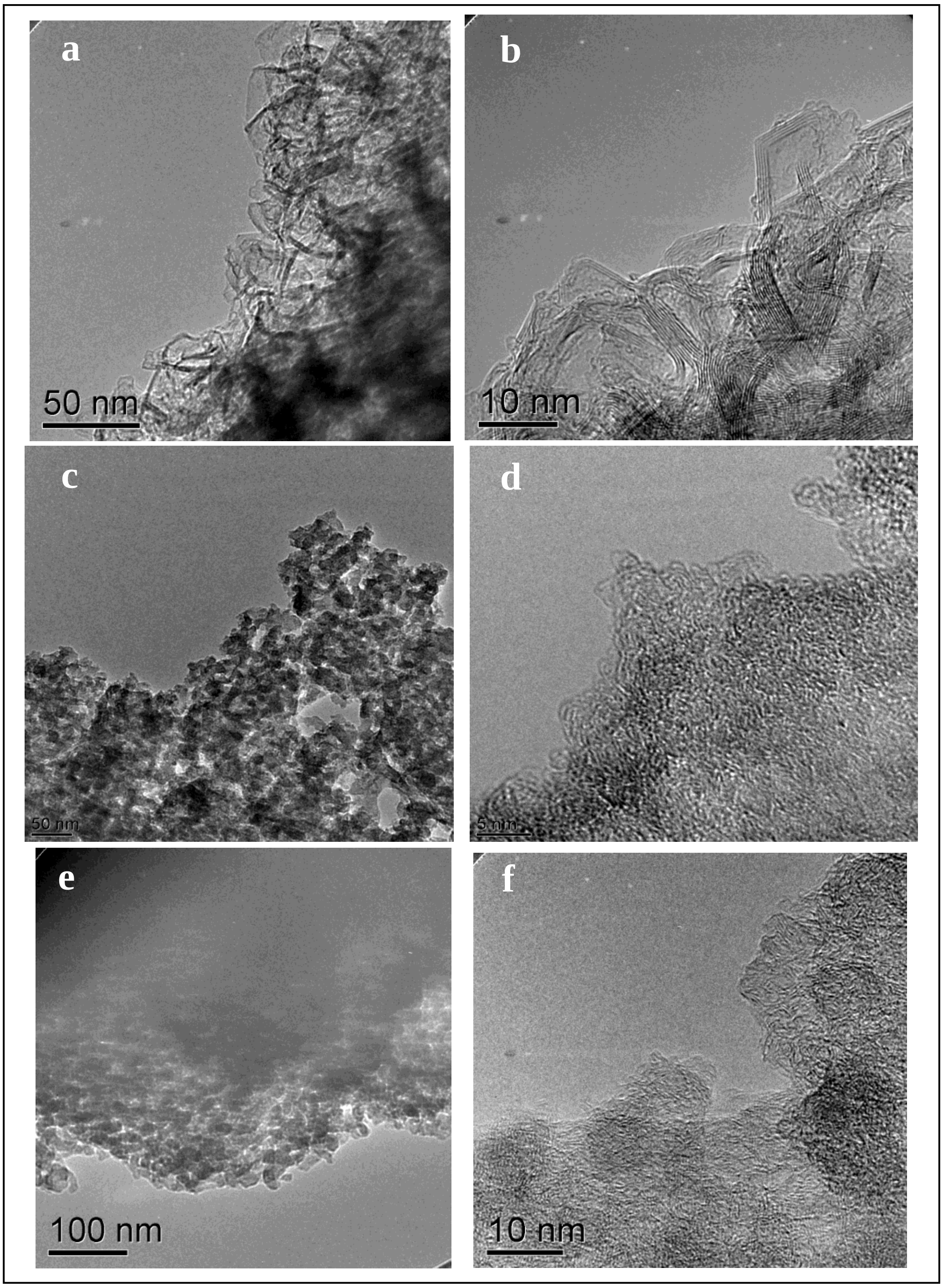

Figure 6.1: High resolution TEM images of commercial PGC at a) low and b) high magnification; Starbon® A800 at c) low and d) high magnification; Starbon® A1000 e) low and f) high magnification; AMCS-UW g) low and h) high magnification and AMCS-W i) low and j) high magnification. The white arrow in figure 1(g) highlights a region of crystalline calcium.

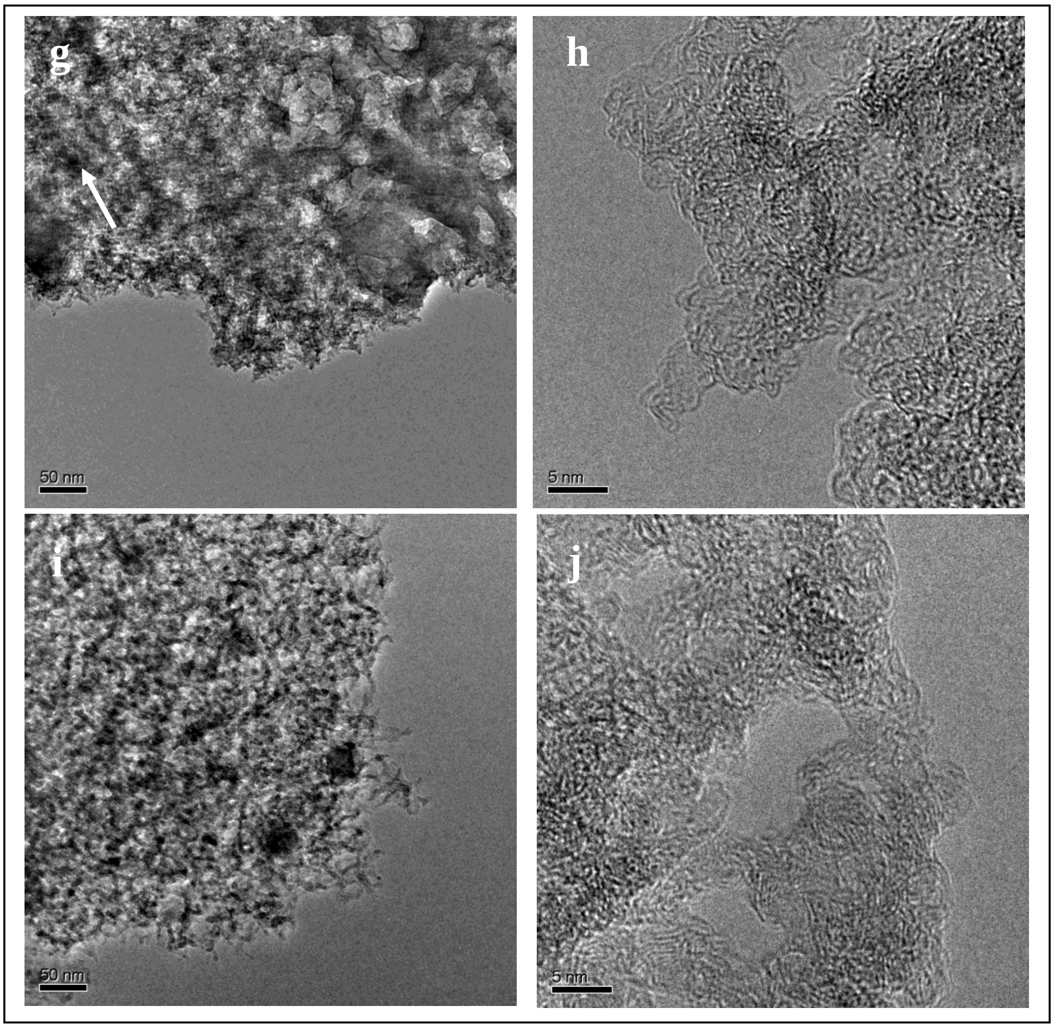

Figure 6.1: (continued)

For Starbon® A1000, the regions sampled at low magnification (Figure 6.1(e)) display the same particulate microstructure and pore structure as observed for Starbon® A800. However, at higher magnification (Figure 6.1(f)), the fullerene-like character is more obvious with more distinct loop structures apparent, which exhibit slightly thicker stacks (between 3-5 graphene layers). Based on the observations at high magnification of short range graphitic order and limited graphite stacking, Starbon® A1000 appears to closely resemble a non-graphitizing carbon pyrolysed to 1000 °C, as described in the paper of Zhang *et al*. (Zhang *et al*., 2011).

With regards to the AMCS samples, the carbon microstructures (Figures 6.1 (h) and (j)) show extensive fullerene-like character with a high degree of smooth curvature, which is also found to enclose a more open network of pores. There is evidence for the presence of closed-loop structures in both washed and unwashed samples, although the washed sample revealed slightly thicker layer packets (4-5 graphene layers), which were less obvious in the AMCS-UW material. However, it is at low magnification where the differences are clearer between the AMCS samples. Both samples differ from alginic acid-derived Starbon® in that the structure is less an agglomeration of particulates and appears to be a more expanded carbon-based material; in particular, Figure 6.1(g) gives evidence for an extended open mesopore structure. Both AMCS materials show a high degree of mesoporosity, together with distinct, dense nanoparticulate regions (observed as dark areas, due to mass-thickness contrast in TEM bright field images); for AMCS-W, these nanoparticulate regions are homogeneously distributed throughout the material, whereas for AMCS-UW this homogeneous distribution is interspersed with additional larger crystalline nanoparticulate regions (as indicated by selected area electron diffraction, and which appear very dark in TEM bright field images due to diffraction contrast). EDX spectroscopic analysis of these samples in the TEM indicates a higher percentage of calcium in these regions of high density than in the more open (less dense) regions, suggesting that these nanoparticles are predominantly a calcium species. The chemical nature of these nanoparticles and crystals were investigated by XPS and are discussed below (see Section 6.4.3).

It is clear that there are significant differences between the microstructures of the commercial PGC, alginic acid-derived Starbon® and AMCS materials. This makes the fact that they exhibit such similar properties in terms of chromatographic separation all the more interesting. In order to understand further the nature of the carbon environments present in these materials, core loss EELS data were collected at the carbon K-edge, which relates to transitions from the carbon 1*s* core level to empty p-like final states above the Fermi level. Analysis of the carbon K-edge using the procedure described by Zhang *et al*. (Zhang *et al*., 2011) is used to gain semi-quantitative information on the level of carbon sp^2 bonding from the relative intensity of the π^* transition at 285 eV, and on the degree of fullerene character from the relative intensity of the residual peak at 287/287.5 eV.

6.4.2.1 Core loss EELS

Representative EELS plots fitted at the carbon K-edge for Starbon® A800 and commercial PGC are shown in Figure 6.2 (a and b respectively). The percentage sp^2

content and percentage fullerene character data derived from these fitted plots using the procedure described by Zhang *et al*. (Zhang *et al*., 2011) for all the samples are summarised in Table 6.2.

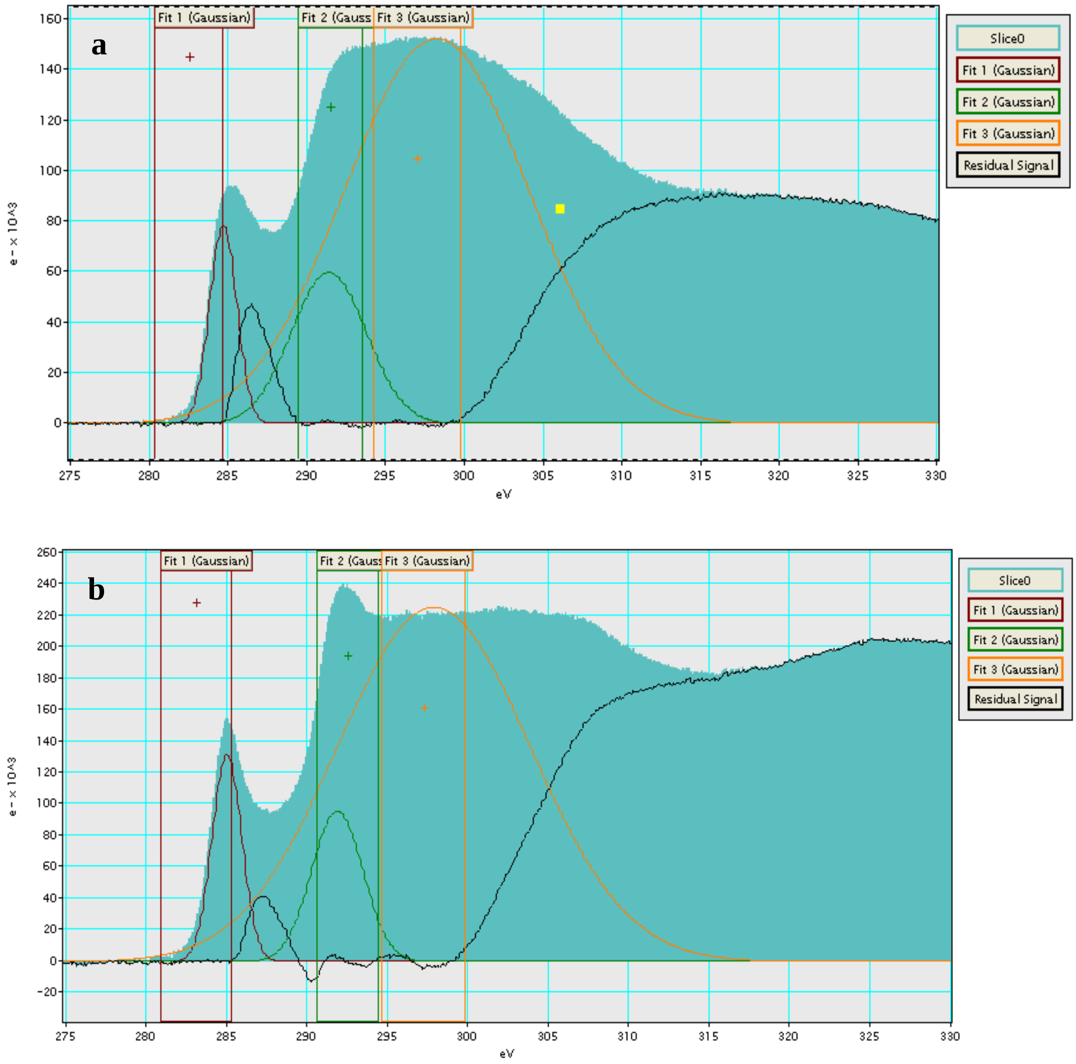

Figure 6.2: Fitted EELS plots at the carbon K-edge for a) Starbon® A800 and b) commercial PGC. The fitted peaks represent: **Fit 1** - C1*s* to π* transition (C-C bond); **Fit 2** - C1*s* to σ* (C-C bond); **Fit 3** - C1s to σ* (C=C bond) and **Residual Signal** - represents fullerene content.

The commercial PGC material exhibits an sp^2 content of greater than 90 % which is expected, given the predominance of highly aligned graphitic layers in this material, and reveals a percentage fullerene content of around 30 %. This data appears to correlate with the evidence provided by the TEM images. This material shows similar though slightly lower values when compared with a phenolic resin-derived, non-graphitizing carbon pyrolysed to 2500 °C investigated by Zhang *et al*. – that exhibited percentages of ca. 98 % carbon *sp*^{2} content and 35 % fullerene character respectively (Zhang *et al*., 2011).

Sample	Percentage *sp*^{2} content / %	Percentage fullerene character /%
Commercial PGC	90 ± 4	30 ± 1
Starbon® A800	72 ± 2	66 ± 12
Starbon® A1000	87 ± 7	55 ± 16
AMCS-UW	76 ± 3	53 ± 5
AMCS-W	82 ± 4	57 ± 6

Table 6.2: Summary of core loss EELS data for all commercial PGC, AMCS and Starbon® samples. Errors represent the standard deviation of analysis from at least three different sample regions.

Starbon® A800 shows a lower *sp*^{2} content (of 72 %) than that observed in Zhang's phenolic resin-derived, non-graphitizing carbon pyrolysed at the same temperature of 800 °C (ca. 84 % - Zhang *et al*., 2011). Meanwhile Starbon® A1000 shows a carbon *sp*^{2} content similar to that seen in a comparative, non-graphitizing carbon pyrolysed at 1000 °C (87 % and 92 % respectively (Zhang *et al*., 2011)). However, both Starbon® A800 and Starbon® A1000 samples show significantly higher levels of fullerene character compared to the standard phenolic resin-derived, non-graphitizing carbons, with 66 % and 55 % compared to 47 % and 26 % for materials pyrolysed to 800 °C and 1000 °C respectively. The AMCS samples show similar values to the Starbon® materials, with fullerene character calculated to be in the range 50 – 60 %.

A recent study by Powles *et al*. (Powles *et al*., 2009) reported the use of molecular-dynamics simulations to describe how self-assembled *sp*^{2}-bonded carbon structures like fullerenes, could arise from highly disordered amorphous precursors. They found that two key factors affected the organising capabilities of *sp*^{2} carbon: (i) the density (thus void space) of the material, and (ii) the geometry of the precursor system.

Focussing first on material density, the materials in our work can be considered low-density bulk carbons and afford a greater void fraction than higher-density carbons e.g. annealed carbons. The simulation study by Powles *et al.* yielded a hypothetical highly curved sp^2 sheet model for low-density bulk carbons which was similar to that put forward by Harris *et al.* to describe the fullerene-like character of non-graphitizing microporous carbons, on the basis of TEM observations (Harris and Tsang, 1997).

Meanwhile, the geometry of the precursor system before pyrolysis is that of a linear polyuronide polymer consisting of two hexuronic acid residues: β-D-mannuronic acid and α-L-guluronic acid. A recent study by Ross *et al.* reported the volatile products released by alginic acid and its calcium and sodium alginate salts during pyrolysis (Ross *et al.*, 2011). The study found that, for alginic acid and calcium alginate, the major volatile component released was furfural, along with smaller quantities of various cyclopentenones. Potentially, the C5 intermediates formed by modification of the hexuronic acid units during the generation of these volatiles may act as the nucleation point and template for the growth of the highly fullerene character observed in our materials.

Further to this, the sp^2 content of the AMCS-W sample was found to be higher than that for the Starbon® A800 sample, with the AMCS-W sample having sp^2 levels that are on a par with those of a standard phenolic resin-derived, non-graphitizing carbon. It is therefore possible that the calcium nanoparticles present throughout these materials may act as nuclei, catalysing the formation of sp^2-hybridised carbon used to grow the fullerene layers observed. The apparently contradictory observation, whereby the AMCS-W sample has a higher sp^2 content than the AMCS-UW sample, could suggest that the large calcium clusters observed in the TEM images of the unwashed material are less effective catalysts for fullerene formation than the more dispersed calcium observed in the washed AMCS sample.

6.4.3 X-ray photoelectron spectroscopy

In order to determine the chemical nature of the calcium present in the alginic acid-derived Starbon® and AMCS materials, samples were analysed by XPS. Figure 6.3 (a) shows the Ca 2*p* signal for the expanded precursor of the alginic acid-derived

Starbon® materials, which is composed of a a pair of spin-orbit split doublets, the 2*p*$_{3/2}$ and 2*p*$_{1/2}$ states, with a 2*p*$_{3/2}$ binding energy of 346.8 eV, indicative of predominantly Ca-OOR interactions.

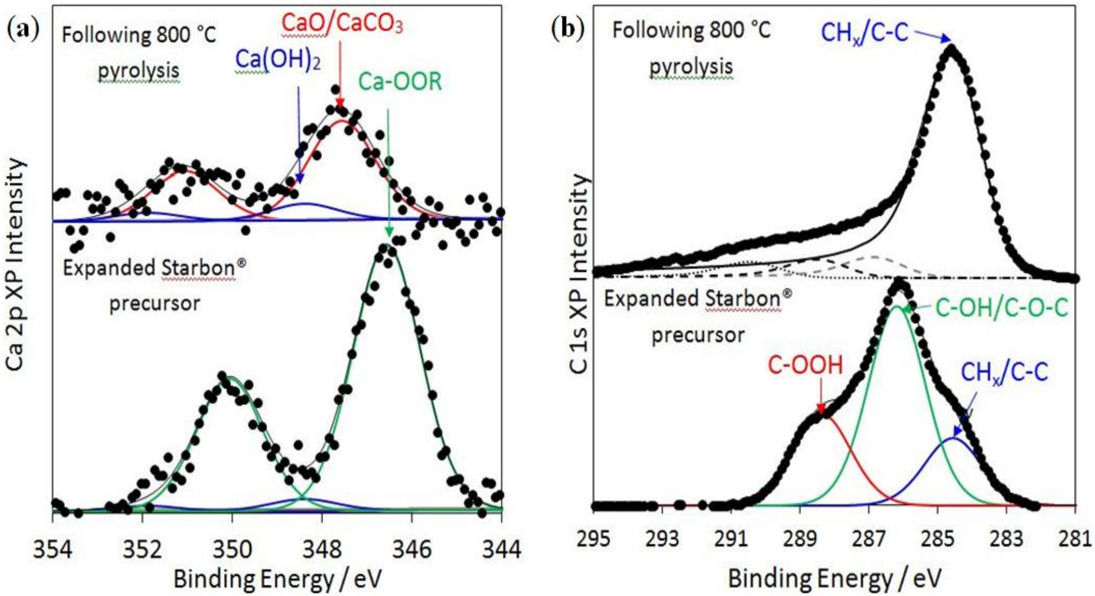

Figure 6.3: XPS analysis of expanded alginic acid-derived Starbon® precursor and pyrolysed to 800 °C (Starbon® A800), in the a) Ca 2*p* and b) C 1*s* binding energy regions

The expansion of alginic acid to a hydrogel is described as an ionotropic gelation process resulting from the binding of Ca^{2+} ions to areas of poly α-L-guluronic acid present in the polysaccharide. This leads to the formation of a secondary structure described by the egg-box model (Grant *et al*., 1973 - Figure 6.4) and these data for the precursor samples are consistent with this model. The source of the calcium in these materials is likely to be primarily that incorporated during alginic acid extraction, during which water-soluble sodium alginate is separated from other polysaccharides present in the algae through gelation with calcium, followed by filtration of the mixture. Following pyrolysis to 800 °C, features attributed to Ca-alginate (Ca-OOR) are lost and new states giving signals at 347.5 and 348.4 eV emerge, attributed to $CaCO_3$/ CaO and $Ca(OH)_2$ respectively.

The changes in the carbon environment following thermal treatment are shown in Figure 6.3 (b), which shows the parent alginate is comprised of three component environments at 284.6 eV (CH_x/C-C), 286.2 eV (COC, C-OH,) and 288.4 eV (COOH), which make up the alginate backbone. The corresponding C 1*s* photoelectron peak of the pyrolysed material shows that pyrolysis results in growth of the main peak at 284.5 eV at the expense of the COOH and COH/C-O-C peaks. The high degree of asymmetry in the new peak is attributed to a graphitic like species, having a characteristic *sp*^{2} environment. Pyrolysis at 1000 °C results in a sharpening of the C 1*s* spectrum and a further decrease in oxygen content, as evidenced by the increased C:O ratio (Table 6.3).

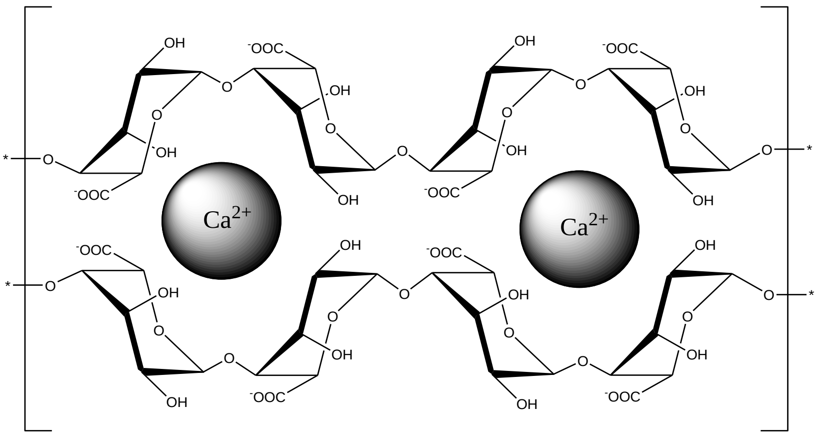

Figure 6.4: Representation of “egg-box” model binding of α-L-guluronic acid blocks to calcium ions in alginic acid

Sample	Elemental atomic percentage / %					C:O ratio
	Na	N	O	Ca	C	
Starbon® precursor	0.2	0.2	46.0	0.4	53.2	1.2
Starbon® A800	4.5	-	15.9	0.2	79.4	5.0
Starbon® A1000	-	0.4	10.5	0.2	88.9	8.5
AMCS-UW precursor	-	-	43.5	4.0	52.5	1.21
AMCS-UW	0.3	-	36.4	9.2	54.1	1.48
AMCS-W precursor	-	-	41.9	1.4	56.7	1.35
AMCS-W	-	-	10.2	2.1	87.7	8.60

Table 6.3: Surface compositions of Starbon® and AMCS samples

Figure 6.5 (a and b) shows the Ca 2*p* and C 1*s* spectra, respectively, for the AMCS-UW precursor and AMCS-UW. In this instance, each of the Ca 2*p* spin orbit split photoelectron lines are composed of a clear doublet, having $2p_{3/2}$ components at

346.8 and 347.5, attributed to Ca-OOR of alginate and CaO/$CaCO_3$ respectively. Following pyrolysis, the CaO/$CaCO_3$ state is retained; however the lower binding energy component is lost. There is an overall shift of the peak envelope to higher binding energy, due to the growth of a new set of doublets, with Ca 2$p_{3/2}$ centred at 348.4 eV which is attributed to $Ca(OH)_2$. Following pyrolysis, growth of the CH_x/C-C component in the C 1*s* spectrum occurs at the expense of the C-OH and COOH features, as the sample carbonizes. In addition, a new state emerges, giving the signal at 290.4 eV, which is attributed to a CO_3 environment, and is consistent with the presence of a large amount of $CaCO_3$ as indicated in the Ca 2*p* spectrum. Powder X-ray diffraction was performed on the AMCS-UW sample in order to determine the $CaCO_3$ phase type (Figure 6.6). Comparison of the sample's diffraction pattern with those for $CaCO_3$ recorded on the FIZ Karlsruhe ICSD suggests that the predominant polymorph is calcite, the pattern strongly correlated to that of Maslen *et al.* (Maslen *et al.*, 1993). The presence of the calcite polymorph is in agreement with Xie et al. who reported that calcite was the predominant polymorph of $CaCO_3$ when alginate beads were prepared with a carbonate mineral bed (Xie *et al.*, 2010). The peaks at $2\theta = 32.2°$, 37.4° and 53.8° could not be assigned although it is believed that they correspond to a minority crystal phase in this sample.

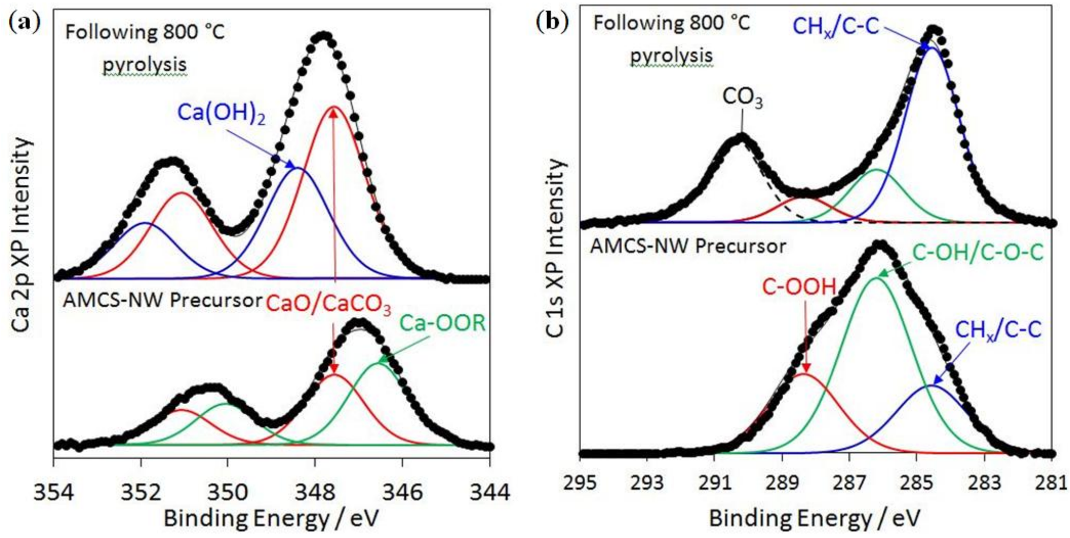

Figure 6.5: XPS analysis of AMCS-UW precursor and AMCS-UW, in the a) Ca 2*p* and b) C 1*s* binding energy regions

The effect of acid washing on pyrolysis was also investigated by XPS (Figure 6.7) which shows that, while a decrease in Ca content is observed (Table 6.3), there is no significant change in the surface carbon functionality (Fig 6.7(b)). Following pyrolysis at 800°C, decomposition of the alginate is observed (as also in Figure 6.4), with the Ca 2*p* exhibiting features for $Ca(OH)_2$ and $CaCO_3$. Inspection of the C 1*s* spectrum now shows a single asymmetric peak for CH_x/C-C similar to that observed for Starbon® A800 and Starbon® A1000. The loss of the peak at 290.4 eV, which was attributed to a carbonate-derived carbon, is consistent with a decrease in $CaCO_3$ in the acid washed sample. The loss of CO_3 is also manifest in the decreased oxygen content in the 800 °C pyrolysed sample (Table 3).

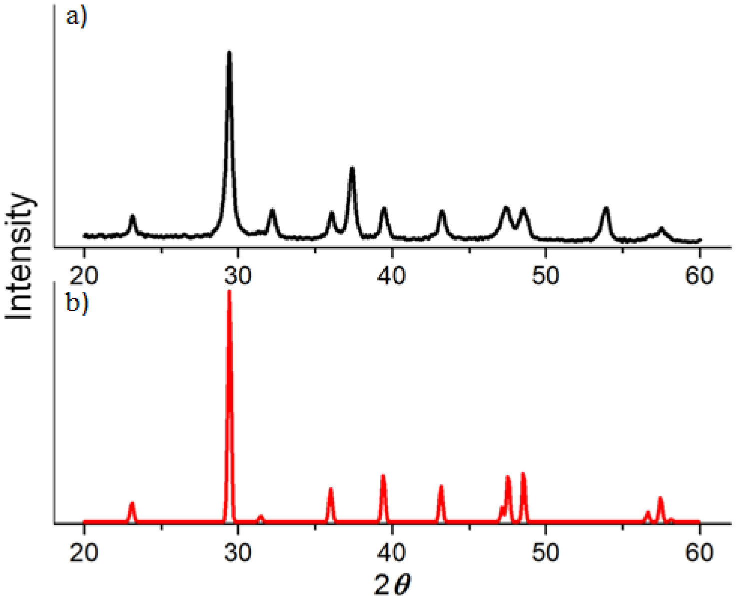

Figure 6.6: Powder XRD patterns for (A) AMCS-UW and (B) $CaCO_3$ polymorph calcite (Maslen, 1993).

Analysis of the sp^2:sp^3 components of the Starbon® and AMCS samples was performed (based on fitted C 1*s* peaks at 284.6 and 286.8 eV respectively) using the procedure described by Díaz *et al.* (Díaz *et al.*, 1996 - Table 6.4). The results are broadly consistent with the deductions from high resolution TEM, that Starbon® A1000 contains a higher degree of sp^2 character than Starbon® A800, and is comparable with the AMCS-W sample. (N.B. The 286.8 eV peak assigned to the sp^3 component overlaps with that for C-OH so any surface oxidation may skew the results.)

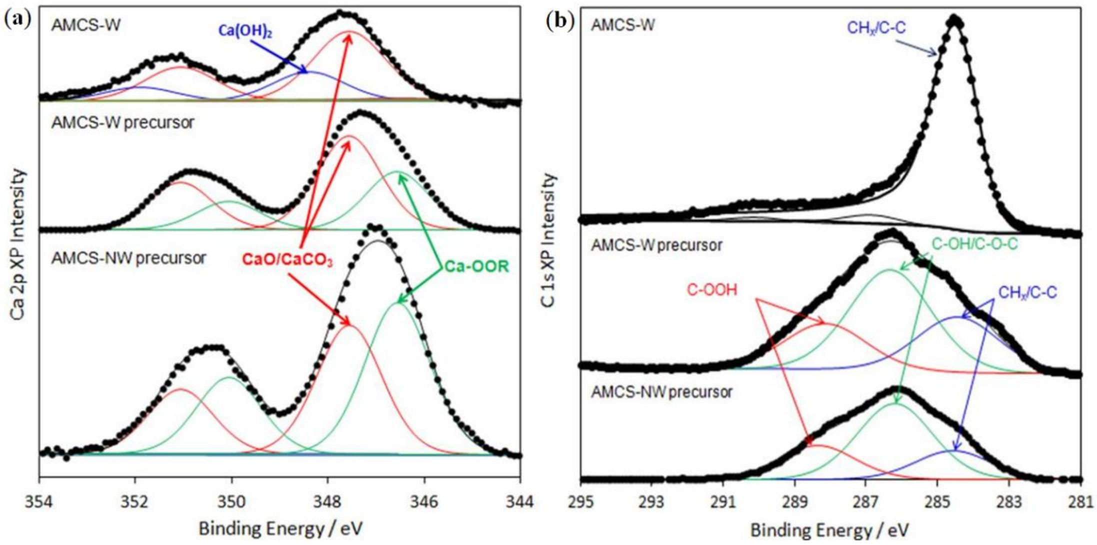

Figure 6.7: XPS analysis of AMCS-W precursor and AMCS-W in the a) Ca 2*p* and b) C 1*s* binding energy regions

Sample	$^{a}sp^{2}:sp^{3}$ ratio
Starbon® A800	11.0
Starbon® A1000	22.7
AMCS-UW	13.0
AMCS-W	18.7

a = based on 284.6 and 286.8 eV components respectively

Table 6.4: $sp^{2}:sp^{3}$ ratio for Starbon® and alginate AMCS samples

6.4.4 Potential mechanism for calcium catalysis

Calcium catalysis of graphitisation processes is discussed widely in the literature, with a number of the articles describing processes whereby catalytic graphitisation of carbonising materials has occurred, albeit at high pressures of 3 kbar, where calcium was added. For example, the acceleration of graphite formation in polyvinyl chloride (PVC) cokes by calcium carbonate (Hirano *et al*., 1979), calcium hydroxide (Noda *et al*., 1969) and calcium oxide (Õya and Õtani, 1979a), was described in the 1970s and products characterised by electron microscopy and X-ray diffraction (XRD). However, more recently, Tsubouchi *et al.* have described the catalysis of turbostratic graphite formation in several coal samples by calcium hydroxide under ambient pressures (Tsubouchi *et al*., 2003).

Two mechanisms of calcium catalysis have been postulated. The first, by Tsubouchi *et al.*, describes a reaction by fine particles of CaO with amorphous carbon present in the forming chars, to produce CO and interstitial calcium carbide/oxide (i.e. $CaO_{\alpha}C_{\beta}$, where α and β are fractional) intermediates (Tsubouchi *et al.*, 2003). The breakdown of this interstitial species then releases carbon in a graphitic form. This mechanism is represented as (Tsubouchi *et al.*, 2003):

$$CaO + C_{(amorphous)} \longrightarrow CaO_{\alpha}C_{\beta} \longrightarrow CaO_{\alpha}C_{\gamma} + C_{x\ (graphitic)}$$

The second mechanism, proposed by Hirano *et al.*, describes an apparently cooperative effect between calcium carbonate and gaseous nitrogen in catalysing carbon graphitisation via a calcium cyanamide intermediate (Hirano *et al.*, 1979):

$$\begin{array}{rcl} CaCO_3 & \longrightarrow & CaO + CO_2 \\ CaO + C_{\ (amorphous)} & \longrightarrow & Ca + CO \\ Ca + 2C_{\ (amorphous)} & \longrightarrow & CaC_2 \\ CaC_2 + N_2 & \longrightarrow & CaCN_2 + C_{\ (graphitic)} \end{array}$$

There is literature precedent suggesting that the carbide intermediate (CaC_2) of the Hirano mechanism is key to the catalytic ability of calcium in the graphitisation process, through the deposition of carbon in the form of acetylene (Õya and Õtani, 1979a; Õya and Õtani, 1979b; Yang *et al.*, 2012). The "graphitic" carbon described in the Hirano (Hirano *et al.*, 1979) paper is likely to be in the form of acetylene and the basis for the fullerene-like structures observed in the alginic acid-derived Starbon® and AMCS materials. Since the carbon materials in the current study were prepared under a nitrogen atmosphere, it would be reasonable to assume that if calcium catalysis occurs, it may predominantly progress by the Hirano mechanism. Alhough no calcium cyanamide ($CaCN_2$) species were detected by XPS, the presence of high levels of calcium carbonate detected in our pyrolysed materials goes some way to supporting this view. In addition, XPS data also suggests the presence of $Ca(OH)_2$ species in both the alginic acid-derived Starbon® and AMCS, with AMCS materials found to have a greater proportion of this calcium species in the pyrolysed sample compared to Starbon®. Õya and Õtani observed $Ca(OH)_2$ during the catalytic graphitisation of a phenol-formaldehyde resin, after the addition of elemental calcium. They concluded that this species was derived from the reaction of CaC_2 with water from the quenching process (Õya and Õtani, 1979b). This could potentially be seen as evidence that a calcium catalysis mechanism for the AMCS materials goes through the same acetylene deposition mechanism as that proposed for other carbon types.

Hirano *et al.* reported that graphitic particles were observed in pyrolysed PV-7 PVC by 1000 °C, although the calcium carbonate infused into their starting material was in the form of “disks 8 mm in diameter and 2.5 mm thick” (Hirano *et al.*, 1979). It is therefore conceivable that the nanoparticulate nature of the calcium species in the alginic acid-derived Starbon® and AMCS materials described here may enhance the catalytic effect still further. An earlier study by Hirano *et al.* reported a positive correlation between the extent of graphite formation and the distribution and concentration of calcium found in several specimens of PVC coke (Hirano *et al.*, 1970). This result by Hirano *et al.* is in agreement with that reported by Õya and Õtani who observed that whilst bulk calcium particles catalysed formation of graphitic carbon, finer particles (homogeneously dispersed throughout the carbon precursor) accelerated the gradual graphitisation of the entire carbon (Õya and Õtani, 1979a). In the case of the unwashed AMCS material, a large proportion of calcium appears to be tied up in large, crystalline structures; the calcium is heterogeneously distributed though the sample, and the concentration of calcium available for catalysis at a particular position is thus lower than that in the washed AMCS material. This could explain why this unwashed AMCS material presented a lower carbon sp^2 content than the washed AMCS sample.

6.5 Discussion and conclusions

Analysis of a commercial PGC material using TEM and core loss EELS indicates that it resembles a typical, high temperature-pyrolysed non-graphitizing carbon derived from phenolic resin. However, analysis of two types of mesoporous carbon derived from the algal polysaccharide alginic acid (Starbon® and AMCS), shows a higher percentage fullerene character than the respective non-graphitizing carbon. In addition, AMCS samples (prepared at 800 °C) had a higher sp^2-content than the alginic acid-derived Starbon® material also pyrolysed to 800 °C. Based on these observations and the results of XPS analysis, a mechanism of calcium catalysis for the formation of fullerene-like carbon has been discussed.

The carbon microstructures of Starbon® and AMCS are considerably different to that of commercial PGC. Both Starbon® and AMCS have extensive curvature due to high-fullerene character whilst the microstructure of PGC predominantly features extended graphitic stacks. The fact that the chromatographic properties of the two biomass-derived carbons are similar to those of PGC suggests that, at the molecular level, the retentive properties of fullerene and turbostratic graphite, for an analyte, are equivalent. In addition, whilst the fullerene stacks of Starbon® and AMCS were limited to 2-3 layers, the graphitic stacks of PGC were 3-6 layers thick which suggests that the stack depth has minimal effect on the retention mechanism in PGC chromatography.

Chapter 7

Concluding remarks and future work

7.1 Concluding remarks

The aims of the work described in this thesis were split into two branches. The primary aim regarded synthesis optimisation of an alginic acid-derived porous carbon material, termed Starbon®, towards its application as a high-performance liquid chromatography (HPLC) stationary phase material. The optimisation aspects reported, driven by the desire to build on the potential of using Starbon® in separation applications, were geared towards enhancing and further understanding the textural, morphological and chemical properties of these materials.

In chapter 4, the effect of pyrolysis rate on the textural properties of Starbon® was investigated using N_2 porosimetry, thermal gravimetry and methylene blue dye adsorption techniques. A trend was established whereby the mesopore structure of the pyrolysed Starbon® materials decreased with increasing rates of pyrolysis. This was deemed to be a result of pressure build-up arising from the rapid generation of volatiles at high pyrolysis rates, as well as the evaporation of residual water present in Starbon® micropores.

In chapter 5, the optimisation of Starbon® particle morphology was attempted using milling, spray-drying and calcium alginate bead techniques. It was ultimately this final approach which generated spherical particle morphology whilst retaining Starbon® pore structure. The novel materials generated, naturally-templated mesoporous carbon alginate beads (AMCS), show good column efficiency results and packing properties similar to the commercial porous carbon column, Hypercarb™.

In chapter 6, carbon hybridisation in pyrolysed Starbon® and AMCS materials was investigated by transmission electron microscopy and X-ray photoelectron spectroscopy techniques. The results were compared against commercial porous graphitic carbon (PGC) material and model non-graphitising carbon data. Both Starbon® and AMCS materials show significantly higher proportions of fullerene character than PGC or model non-graphitising carbons. The generation of C5 intermediates during the pyrolysis of the alginic acid precursor was a mooted reason for this observation. In addition, AMCS materials showed larger relative amounts of

sp^2-hybridised carbon than the corresponding Starbon® material. A mechanism of calcium-catalysed graphitisation was suggested for this difference.

The secondary aim of this thesis was to develop and apply PGC-LC-MS approaches, using a Hypercarb™ PGC column, for the targeted and untargeted analysis of the primary metabolome of several drought-stressed model plant species. The method development aspect was driven by the need to separate and identify polar carbohydrate-based compounds from complex biological extracts. The use of Hypercarb™ was appropriate in his case as its retention mechanism allows for the separation of isomeric species whilst using MS compatible mobile phase systems to enable efficient and robust on-line coupling with ESI-MS.

In chapter 2, a robust PGC-LC-MS method was developed for the targeted analysis of carbohydrates extracted from drought-stressed *Haberlea rhodopensis* leaf blade tissue at various timepoints. In summary, monosaccharide levels decreased during WD; the levels of sucrose, an osmolyte, rose significantly during WD; whilst levels of ROS scavengers, the raffinose family oligosaccharides, were generally maintained during WD. The results were compared to (and found to be in general agreement with) other *H rhodopensis* studies as well as literature describing the effect of abiotic stresses on carbohydrate-based plant metabolites.

In chapter 3, a PGC-LC-MS method was developed for the untargeted analysis of complex leaf blade extracts from drought-stressed, model plant species *Arabidopsis thaliana* and *Thellungiella salsuginea*. The full scan datasets of each plant species were individually statistically analysed using multivariate and univariate methods. Principal components analysis (PCA) of the both plant species datasets showed distinct groupings; separating late stress samples from all others stress states. Further analysis of the early stress states gave some indication that a response to drought stress is initiated earlier in *T salsuginea* than *A thaliana*. Score ranking plots were found to be dominated by the increase in sucrose levels and decrease in citric acid levels for both plant species.

Overall, although the desire to develop Starbon® particles for HPLC applications is yet to be completed, the work in this thesis reports significant leaps towards fulfilling this goal. In addition, the separation of several complex polar compound mixtures, using Hypercarb™, has highlighted the advantages that porous carbon columns can bring to chromatographic analysis as a whole.

7.2 Future work

Although the PGC-LC-MS analysis of *H. rhodopensis* leaf blade tissues was targeted at particular carbohydrate analytes, full-scan data was recorded and so could be further mined by statistical analysis methods, analogous to the work performed in chapter 3. Comparison of this data with that collected for *T salsuginea* could uncover drought-responsive metabolites which are conserved across species of similar stress-resistance but diverse gene pools.

The *A. thaliana* and *T. salsuginea* study concluded with a number of analytes which scored well in the statistical ranking plots isolated for MS^2 and MS^n analysis. Although several analytes were tentatively assigned based on accurate mass and fragment analysis, the assignments would need to be confirmed by injecting authentic standards into the PGC-LC-MS system and comparing retention time and mass spec fragmentation data. In addition, there were several compounds which were not identified. Further work, using available literature and plant metabolite databases to provide potential plant metabolite candidates is required.

With chromatographic performance similar to Starbon® but with an improved packing efficiency, AMCS have shown to be a key step forward in the generation of biomass-derived commercial porous carbon stationary phase. Future work with regards to these materials will centre on the optimisation of particle size from the current mean value of ca. 23 μm to the 5-10 μm particle size range of commercial porous graphitic carbon particles. One potential route to a reduced particle size could be via the use of structure-directing additives. Wohlgemuth *et al*. reported how the addition of L-cysteine or S-(2-thienyl)-L-cysteine into a glucose solution and heating by hydrothermal carbonization (HTC) yielded sulphur-doped porous carbon microspheres (Wohlgemuth *et al*., 2012). This study was based on earlier work by

Choi *et al*., who used different amino acids to generate a range of heteroatom-doped carbons. By changing the amino acid used, the heteroatom concentration could be controlled (Choi *et al*., 2011).

An experiment based on the work by Wohlgemuth *et al*. has been attempted in order to determine whether the use of structure-directing additives could be applied to the development of porous carbon stationary phase. In an effort to simplify the process the 16 h HTC method used by Wohlgemuth *et al*. was replaced by a 30 min microwave treatment albeit at the same reaction temperature (130 °C). In addition, the cysteine additive was replaced by nicotinic acid, determined by Choi *et al*. to give the lowest heteroatom doping concentration in the final carbon material. The experiment was performed in both a glucose solution and later an alginic acid solution. Images of the resulting dried product are shown in Figure 7.1.

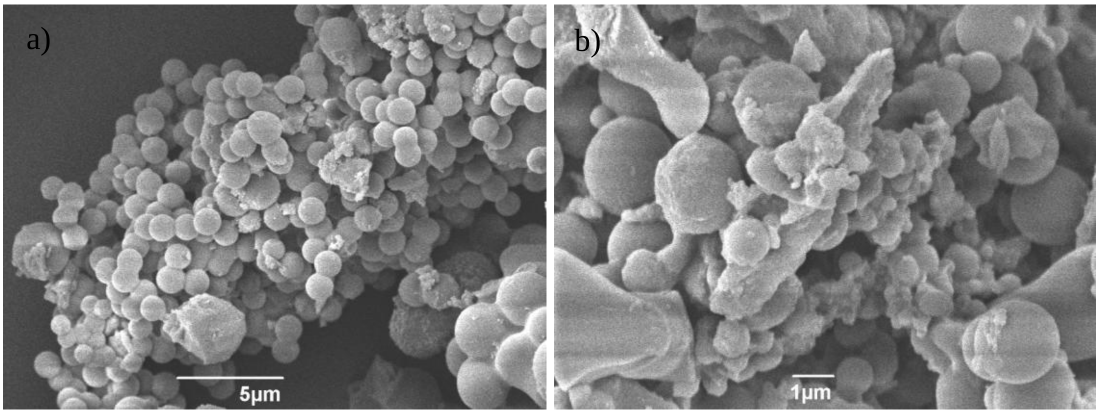

Figure 7.1: SEM images of solid product after microwave teatment of a) glucose with nicotinic acid and b) alginic acid and nicotinic acid.

The solid generated by microwave treatment of the glucose solution with nicotinic acid (Figure 7.1a) appears identical to the product reported by Wohlgemuth *et al*. using the HTC treatment and cysteine additive (Wohlgemuth *et al*., 2012). The solid obtained using an alginic acid solution, whilst not as consistent as the glucose-derived material does exhibit some microsphere formation (Figure 7.1b). The results of this experiment could therefore provide one potential avenue of investigation towards particle size optimisation.

Appendix 1

List of abbreviations

°C	degrees centigrade
Å	angstrom
AC	activated carbons
AMCS	calcium alginate-derived mesoporous carbon spheres
ATP	adenosine triphosphate
ATR	attenuated total reflectance
a_z	Mathieu working point at the end-cap electrode
BET	Brunauer Emmett Teller
BJH	Barrett Joyner Halenda
BM	ball-milled
cDNA	chromosomal deoxyribose nucleic acid
CID	collision induced dissociation
cm^{-1}	wavenumber
CMK	Carbon Materials from Korea
CNT	carbon nanotubes
CRM	charged residue model
CVD	chemical vapour deposition
dc	direct current
DM	dry mass
DNA	deoxyribose nucleic acid
dTG	differential thermal gravimetry
EC	European Commission
EDX	energy dispersive X-ray analysis
EELS	electron energy loss spectroscopy
ESI	electrospray ionisation
eV	electronvolts
FA	formic acid
FM	fresh mass
Fru	fructose
FT-ICR	Fourier-transform ion cyclotron resonance
FT-IR	Fourier-transform infrared spectroscopy
FWHM	full width half maximum
g	gram

g	gravity
G	α-1,4-linked L-guluronic acid
GC	gas chromatography
Glc	glucose
GPa	gigapascal
GTCB	graphitized thermal carbon black
h	hour
H	theoretical plate height
HCl	hydrochloric acid
HILIC	hydrophilic interaction liquid chromatography
HM	hand-milled
HPAEC	high performance anion exchange chromatography
HPLC	high performance liquid chromatography
HTC	hydrothermal carbonization
IEM	ion evaporation model
IUPAC	International Union of Pure and Applied Chemistry
K	degrees Kelvin
kDa	kilodalton
keV	kiloelectronvolts
k_p	pyrolysis heating rate
kV	kilovolts
L	litre
LC	liquid chromatography
LC-MS	liquid chromatography-mass spectrometry
LI	liquid impregnation
m	metre
M	β-1,4-linked D-mannuronic acid / Molar
m/z	mass-to-charge ratio
Mb	megabases
mbar	millibar
MCM	Mobil Composition of Matter
Meso/Macro	percentage mesoporosity and macroporosity
mg	milligram

Mic.	percentage microporosity
min	minute
mL	millilitre
mm	millimetre
MPC	mean particle circularity
MPD	mean particle diameter
MRI	magnetic resonance imaging
mRNA	micro ribose nucleic acid
MS	mass spectrometry
MS/MS	tandem mass spectrometry
MS^2	tandem mass spectrometry
mtorr	millitorr
nm	nanometre
NMR	nuclear magnetic resonance
NP-LC	normal phase liquid chromatography
oaTOF	orthogonal acceleration time-of-flight
OMC	ordered mesoporous carbons
P/P_o	relative pressure
P4VP	poly(4-vinylpyridine)
PAD	pulsed ampometric detection
PC	principal component
PCA	principal components analysis
PD	pore diameter
P*e*	Peclet number
PEO	poly (ethylene oxide)
PGA	propylene glycol alginate
PGC	porous graphitic carbon
PLS-DA	partial least squares discriminant analysis
ppm	parts per million
PPO	poly (propylene oxide)
PREG	polar retention effect on graphite
PS	polystyrene
PSD	particle size distribution

PVC	polyvinyl chloride
PV_{des}	desorption pore volume
Q	quadrupole mass analyser
QC	quality control
QIT	quadrupole ion trap mass analyser
QQQ	triple-stage quadrupole mass analyser
Q-TOF	quadrupole time-of-flight mass analyser
q_z	Mathieu working point at the ring electrode
R^2	correlation coefficient
rf	radio frequency
RFOs	raffinose-family oligosaccharides
RGD	arginine-glycine-aspartic acid
ROS	reactive oxygen species
RP-LC	reversed-phase liquid chromatography
rpm	revolutions per minute
RSD	relative standard deviation
RWC	relative water content
s	second
S_{BET}	surface area determined by Brunauer Emmett Teller equation
$scCO_2$	supercritical carbon dioxide
SD	standard deviation / spray-dried
SE_{D-R}	Dubinin-Radushkevich surface energy
SEM	scanning electron microscopy
SORI-CID	sustained off-resonance irradiation collision-induced dissociation
Suc	sucrose
t	time
TEM	transmission electron microscope
TG	thermal gravimetry
TG-IR	thermal gravimetry-infrared spectroscopy
TM	turgid mass
TOF	time-of-flight
t_R	retention time
U	dc voltage / dc trapping voltage

UC	unknown compound
UHR	ultrahigh resolution
UM	un-milled
UV	ultra-violet
UW	unwashed
V	rf amplitude / fundamental rf
V	volt
v/v	volume-per-volume
W	washed
w/w	weight-per-weight
WD	water deficit
XPS	X-ray photoelectron spectroscopy
XRD	X-ray diffraction
XRF	X-ray fluorescence spectrometry
ZIC-HILIC	HILIC column with sulfoalkylbetaine zwitterion functionality
µL	microlitre
µm	micrometre
µM	micromolar
µmol	micromole

References

Alekseyev N. I. & Dyuzhev G. A. 2003. Fullerene formation in an arc discharge. *Carbon*, 41, 1343-1348

Alpert A. J. 1990. Hydrophilic-interaction chromatography for the separation of peptides nucleic acids and other polar compounds. *J. Chromatogr.*, 499, 177-196

Alpert A. J., Shukla M., Shukla A. K., Zieske L. R., Yuen S. W., Ferguson M. A. J., Mehlert A., Pauly M. & Orlando R. 1994. Hydrophilic-interaction chromatography of complex carbohydrates. *J. Chromatogr. A*, 676, 191-202

Al-Shehbaz I. A., O'Kane Jr. S. L. & Price R. A. 1999. Generic placement of species excluded from *Arabidopsis* (Brassicacae). *Novon*, 9, 296-307

Amtmann A., Bohnert H. J. & Bressan R. A. 2005. Abiotic stress and plant genome evolution. Search for new models. *Plant Physiol.*, 138, 127-130

Amtmann A. 2009. Learning from evolution: Thellungiella generates new knowledge on essential and critical components of abiotic stress tolerance in plants. *Mol. Plant*, 2, 3-12

Antonio C., Larson T., Gilday A., Graham I., Bergström E. & Thomas-Oates J. 2007. Quantification of sugars and sugar phosphates in *Arabidopsis thaliana* tissues using porous graphitic carbon liquid chromatography-electrospray ionization mass spectrometry. *J. Chromatogr. A*, 1172, 170-178

Antonio C., Pinheiro C., Chaves M. M., Ricardo C. P., Ortuño M. F. & Thomas-Oates J. 2008a. Analysis of carbohydrates in Lupinus albus stems on imposition of water deficit, using porous graphitic carbon liquid chromatography-electrospray ionization mass spectrometry. *J. Chromatogr. A*, 1187, 111-118

Antonio C., Larson T., Gilday A., Graham I., Bergström E. & Thomas-Oates J. 2008 b. Hydrophilic interaction chromatography/electrospray mass spectrometry analysis of carbohydrate-related metabolites from *Arabidopsis thaliana* leaf tissue. *Rapid Commun. Mass. Spectrom.*, 22, 1399-1407

Armstrong D. W. & Jin H. L. 1989. Evaluation of the liquid chromatographic separation of monosaccharides, disaccharides, trisaccharides, tetrasacharides, deoxysaccharides and sugar alcohols with stable cyclodextrin bonded phase columns. *J. Chromatogr*., 462, 219-232

Augst A. D., Kong H. J. & Mooney D. J. 2006. Alginate hydrogels as biomaterials. *Macromol. Biosci*., 6, 623-633

Avonce N., Leyman B., Mascorro-Gallardo J. O., Van Dijck P., Thevelein J. M. and Iturriaga G. 2004. The Arabidopsis trehalose-6-P synthase AtTPS1 gene is a regulator of glucose, abscisic acid, and stress signaling. *Plant Physiol*., 136, 3649-3659

Balogh M. P. 2004. Debating resolution and mass accuracy in mass spectrometry. *Spectroscopy*, 19, 34-40

Barrett E. P., Joyner L. G. & Halenda P. P. 1951. The determination of pore volume and area distributions in porous substances. I. Computations from nitrogen isotherms. *J. Am. Chem. Soc*., 73, 373-380

Bartels D. & Sunkar R. 2005. Drought and Salt Tolerance in Plants. *Crit. Rev. Plant Sci*., 24, 23-58

Batson P. E. 1993. Carbon 1*s* near-edge-absorption fine structure in graphite. *Phys. Rev. B*, 48, 2608-2610

Becalski A., Lau B. P. -Y., Lewis D. & Seaman S. W. 2003. Acrylamide in foods: Occurrence, sources, and modeling. *J. Agric. Food Chem*., 51, 802-808

Bent A. F. 2000. Arabidopsis in planta transformation. Uses, mechanisms, and prospects for transformation of other species. *Plant Physiol*., 124, 1540-1547

Bixler H. J. & Porse H. 2011. A decade of change in the seaweed hydrocolloids industry. *J. Appl. Phycol*., 23, 321-335

Blake W. J., Kærn M., Cantor C. R. & Collins J. J. 2003. Noise in eukaryotic gene expression. *Nature*, 422, 633-637

Bosi S., Da Ros T., Spalluto G. & Prato M. 2003. Fullerene derivatives: an attractive tool for biological applications. *Eur. J. Med. Chem.*, 38, 913-923

Bovenkerk H. P., Bundy F. P., Hall H. T., Strong H. M. & Wentorf R. H. 1959. Preparation of diamond. *Nature*, 184, 1094-1098

Breitling R., Pitt A. R. & Barrett M. P. 2006. Precision mapping of the metabolome. *Trends Biotech.*, 24, 543-548

Bressan R. A., Zhang C., Zhang H., Hasegawa P. M., Bohnert H. J. & Zhu J. -K. 2001. Learning from the Arabidopsis experience. The next gene search paradigm. *Plant Physiol.*, 127, 1354-1360

Bruinsma P. J., Kim A. Y., Liu J. & Baskaran S. Mesoporous silica synthesized by solvent evaporation: Spun fibres and spray-dried hollow spheres. *Chem. Mater.*, 9, 2507-2512

Brunauer S., Emmett P. H. & Teller E. 1938. Adsorption of gases in multimolecular layers. *J. Am. Chem. Soc.*, 60, 309-319

Budarin V., Clark J. H., Deswarte F. E. I., Hardy J. J. E., Hunt A. J. & Kerton F. M. 2005. Delicious not siliceous: expanded carbohydrates as renewable separation media for column chromatography. *Chem. Commun.*, 2903-2905

Budarin V., Clark J. H., Hardy J. J. E., Luque R., Milkowski K., Tavener S. J. & Wilson A. J. 2006. Starbons: New starch-derived mesoporous carbonaceous materials with tunable properties. *Angew. Chem.*, 118, 3866-3870

Bulut E. & Sanli O.2013. Delivery of Alzheimer's drug donepezil hydrochloride from ionically crosslinked alginate microspheres prepared by water-in-oil emulsion technique: Optimization of release conditions. *Asian J. Chem.*, 25, 3993-4000

Buszewski B., Michel M., Cudziło S. & Chyłek Z. 2009. High performance liquid chromatography of 1,1-diamino-2,2-dinitroethene and some intermediate products of its synthesis. *J. Hazard Mater*., 164, 1051-1058

Caffrey M., Fonseca V. & Leopold A. C. 1988. Lipid-sugar interactions: Relevance to anhydrous biology. *Plant Physiol.*, 86, 754-758

Casson D. & Emery A. N. 1987. On the elimination of artefactual effects in assessing the structure of calcium alginate cell immobilization gels. *Enzyme Microb. Technol*., 9, 102-106

Chambers S. D. & Lucy C. A. 2007. Surfactant coated graphitic carbon based stationary phases for anion-exchange chromatography. *J. Chromatogr. A*, 1176, 178-184

Chaves M. M. & Oliveira M. M. 2004. Mechanisms underlying plant resilience to water deficits: prospects for water-saving agriculture. *J. Exp. Bot*. 55, 2365-2384

Che G., Lakshmi B. B., Fisher E. R. & Martin C. R. 1998. Carbon nanotubule membranes for electrochemical energy storage and production. *Nature*, 393, 346-349

Chen Y., Fitz Gerald J., Chadderton L. T. & Chaffron L. 1999. Nanoporous carbon produced by ball milling. *Appl. Phys. Lett*., 74, 2782-2784

Choi C. H., Park S. H. & Woo S. I. 2011. Heteroatom doped carbons prepared by the pyrolysis of bio-derived amino acids as highly active catalysts for oxygen electro-reduction reactions. *Green Chem*., 13, 406-412

Ciccioli P., Tappa R., Di Corcia A. & Liberti A. 1981. Graphitized carbon black columns for high-performance liquid chromatography. *J. Chromatogr*. 206, 35-42

Clark J. H., Budarin V., Dugmore T., Luque R., Macquarrie D. J. & Strelko V. 2008. Catalytic performance of carbonaceous materials in the esterification of succinic acid. *Catal. Commun*., 9, 1709-1714

Coleman J. N., Khan U. & Gun'ko Y. K. 2006. Mechanical reinforcement of polymers using carbon nanotubes. *Adv. Mater*., 18, 689-706

Colin H. & Guiochon G. 1976. Development and use of carbon adsorbents in high-performance liquid-solid chromatography I. Carbon-coated silica particles. *J. Chromatogr*., 126, 43-62

Colin H. & Guiochon G. 1977. Development and use of carbon adsorbents in high-performance liquid-solid chromatography II. Reproducibility of carbon adsorbents and the influence of graphitization on their performance. *J. Chromatogr*., 137, 19-33

Costello M. C., Tossell D. A., Reece D. M., Brierley C. J. & Savage J. A. 1994. Diamond protective coatings for optical components. *Diam. Relat. Mater*., 3, 1137-1141

Cubbon S., Bradbury T., Wilson J. & Thomas-Oates J. 2007. Hydrophilic interaction chromatography for mass spectrometric metabonomic studies of urine. *Anal. Chem*., 79, 8911-8918

Cubbon S., Antonio C., Wilson J. & Thomas-Oates J. 2010. Metabolomic applications of HILIC-LC-MS. *Mass Spectrom. Rev*., 29, 671-684

Dąbrowski A., Podkościelny P., Hubicki Z. & Barczak M. 2005. Adsorption of phenolic compounds by activated carbon - a critical review. *Chemosphere,* 58, 1049-1070

Daniels H., Brown A., Scott A., Nichells T., Rand B. & Brydson R. 2003. Experimental and theoretical evidence for the magic angle in transmission electron energy loss spectroscopy. *Ultramicroscopy*, 96, 523-534

Daniels H., Brydson R., Rand B. & Brown A. 2007. Investigating carbonization and graphitization using electron energy loss spectroscopy (EELS) in the transmission electron microscope (TEM). *Philos. Mag.*, 87, 4073-4092

de Boer J. H. & Zwikker C. 1929. Absorption as a consequence of polarisation. The absorption isotherm. *Zeitschr. physik. Chem.*, 3, 407-418

de Sousa Abreu R., Penalva L. O., Marcotte E. M. & Vogel C. 2009. Global signatures of protein and mRNA expression levels. *Mol. BioSyst.*, 5, 1512-1526

Díaz J., Paolicelli G., Ferrer S. & Comin F. 1996. Separation of the sp^3 and sp^2 components in the C*1s* photoemission spectra of amorphous carbon films. *Phys. Rev. B*, 54, 8064-8069

Dienwiebel M., Verhoeven G. S., Pradeep N., Frenken J. W. M., Heimberg J. A. & Zandbergen H. W. 2004. Superlubricity of graphite. *Phys. Rev. Lett.*, 92, 126101

Disma F., Aymard L., Dupont L. & Tarascon J. -M. 1996. Effect of mechanical grinding on the lithium intercalation process in graphites and soft carbons. *J. Electrochem. Soc.*, 143, 3959-3972

Djilianov D., Ivanov S., Moyankova D., Miteva L., Kirova E., Alexieva V., Joudi M., Peshev D. & Van den Ende W. 2011. Sugar ratios, glutathione redox status and phenols in the resurrection species *Haberlea rhodopensis* and the closely related non-resurrection species *Chirita eberhardtii*. *Plant Biology*, 13, 767-776

Doi S., Clark J. H., Macquarrie D. J. & Milkowski K. 2002. New materials based on renewable resources: chemically modified expanded corn starches as catalysts for liquid phase organic reactions. *Chem. Commun.*, 22, 2632-2633

Dole M., Mack L. L., Hines R. L., Mobley R. C., Ferguson L. D. & Alice M. B. 1968. Molecular beams of macroions. *J. Chem. Phys*., 49, 2240-2249

Draget K. I., Smidsrød O. & Skjåk-Bræk G. 2005. in *Polysaccharides and Polyamides in the Food Industry: Properties, Production, and Patents*. eds: A. Steinbüchel, S. K. Ree, Wiley-VCH, Weinheim, Germany, 1-30

Dunn W. B., Broadhurst D. I., Atherton H. J., Goodacre R. & Griffin J. L. 2011. Systems level studies of mammalian metabolomes: the roles of mass spectrometry and nuclear magnetic resonance spectroscopy. *Chem. Soc. Rev*., 40, 387-426

Dunn W. B., Wilson I. D., Nicholls A. W. & Broadhurst D. 2012. The importance of experimental design and QC samples in large-scale and MS-driven untargeted metabolomic studies of humans. Bioanalyis, 4, 2249-2264

Dupas S. Guenu S., Pichon V., Monteil A., Welté B. & Hennion M. -C. 1996. Long-term monitoring of pesticides and polar transformation products in ground water using automated on-line trace-enrichment and liquid chromatography with diode array detection. *Intern. J. Environ. Anal. Chem*., 65, 53-68

Durham D. K. & Hurley T. R. 2007. Effect of sub-2-micron particle size on peak efficiency, capacity, and resolution in preparative liquid chromatography. *J. Liq. Chromatogr. R. T*., 30, 1895-1901

Elversson J. & Millqvist-Fureby A. 2005. Particle size and density in spray drying - Effects of carbohydrate properties. *J. Pharm. Sci*., 94, 2049-2060

Everett D. H. 1972. Manual of symbols and terminology for physicochemical quantities and units, Appendix II: Definitions, terminology and symbols in colloid and surface chemistry. *Pure Appl. Chem*., 31, 578-638

Eversole W. G. 1962. Synthesis of diamond. *US Patent*, 3030188

Falcao E. H. L. & Wudl F. 2007. Carbon allotropes: beyond graphite and diamond. *J. Chem. Technol. Biotechnol*., 82, 524-531

Farrant J. M., Brandt W. & Lindsey G. G. 2007. An overview of mechanisms of desiccation tolerance in selected angiosperm resurrection plants. *Plant Stress*, 1, 72-84

Farrant J. M., Pammenter N. W., Berjak P. & Walters C. 1997. Subcellular organization and metabolic activity during the development of seeds that attain different levels of desiccation tolerance. *Seed Sci. Res*., 7, 135-144

Fatouros P. P., Corwin F. D., Chen Z. -J., Broaddus W. C., Tatum J. L., Kettenmann B., Ge Z., Gibson H. W., Russ J. L., Leonard A. P., Duchamp J. C. & Dorn H. C. 2006. In vitro and in vivo imaging studies of a new endohedral metallofullerene nanoparticle. *Radiology*, 240, 756-764

Fenn J. B., Mann M., Meng C. K., Wong S. F. & Whitehouse C. M. 1989. Electrospray ionization for mass spectrometry of large biomolecules. *Science*, 246, 64-71

Fenn J. B. 1993. Ion formation from charged droplets: Roles of geometry, energy, and time. *J. Am. Soc. Mass Spectrom*., 4, 524-535

Fenoradosoa T. A., Ali G., Delattre C., Laroche C., Petit E., Wadouachi A. & Michaud P. 2010. Extraction and characterization of an alginate from the brown seaweed *Sargassum turbinarioides* Grunow. *J. Appl. Phycol*., 22, 131-137

Feurle J., Jomaa H., Wilhelm M., Gutsche B. & Herderich M. 1998. Analysis of phosphorylated carbohydrates by high-performance liquid chromatography-electrospray ionization tandem mass spectrometry utilising a β-cyclodextrin bonded stationary phase. *J. Chromatogr. A*, 803, 111-119

Flandrois S. & Simon B. 1999. Carbon materials for lithium-ion rechargeable batteries. *Carbon*, 37, 165-180

Foley H. C. 1995. Carbogenic molecular sieves: synthesis, properties and applications. *Microporous Mater.*, 4, 407-433

Franklin R. E. 1951. Crystallite growth in graphitizing and non-graphitizing carbons. *Proc. R. Soc.*, A209, 196-218

Freitas M. M. A. & Figueiredo J. L. 2001. Preparation of carbon molecular sieves for gas separations by modification of the pore sizes of activated carbons. *Fuel,* 80, 1-6

Gaffney T. R. 1996. Porous solids for air separation. *Curr. Opin. Solid St. M.,* 1, 69-75

Gechev T. S., Benina M., Obata T., Tohge T.,Sujeeth N., Minkov N., Hille J., Temanni M. –R., Marriott A. S., Bergström E., Thomas-Oates J., Antonio C., Mueller-Roeber B., Schippers J. H. M., Fernie A. R. & Toneva V. 2013. Molecular mechanisms of desiccation tolerance in the resurrection glacial relic *Haberlea rhodopensis*. *Cell .Mol. Life Sci.,* 70, 689-709

Geim A. K. 2009. Graphene: Status and prospects. *Science*, 324, 1530-1534

Gennaro L. A., Harvey D. J. & Vouros P. 2003. Reversed-phase ion-pairing liquid chromatography / ion trap mass spectrometry for the analysis of negatively charged, derivatized glycans. *Rapid Commun. Mass Spectrom*., 17, 1528-1534

Ghasempour H. R., Gaff D. F., Williams R. P. W. & Gianello R. D. 1998. Contents of sugars in leaves of drying desiccation tolerant flowering plants, particularly grasses. *Plant Growth Regul.*, 24, 185-191

Gilbert M. T., Knox J. H. & Kaur B. 1982. Porous glassy carbon, a new columns packing material for gas chromatography and high-performance liquid chromatography. *Chromatographia*, 16, 138-146

Glenn G. M. & Irving D. W. 1995. Starch-based microcellular foams. *Cereal Chem*., 72, 155-161

Glenn G. M. & Stern D. J. 1999. Starch-based microcellular foams. *US Patent*, 5958589

Gómez-Ordóñez E. & Rupérez P. 2011. FTIR-ATR spectroscopy as a tool for polysaccharide identification in edible brown and red seaweeds. *Food Hydrocolloid*., 25, 1514-1520

Grant G. T., Morris E. R., Rees D. A., Smith P. J. C. & Thom D. 1973. Biological interactions between polysaccharides and divalent cations: The egg-box model. *FEBS Lett*., 32, 195-198

Gregg S. J. & Sing K. S. W. 1982. *Adsorption, surface area and porosity, 2nd Edition*. Academic Press, San Diego, USA, 111-190

Grimmer J. F., Gunnlaugsson C. B., Alsberg E., Murphy H. S., Kong H. J., Mooney D. J. & Weatherly R. A. 2004. Tracheal reconstruction using tissue-engineered cartilage. *Arch. Otolaryngol. Head Neck Surg*., 130, 1191-1196

Gritti F., Farkas T., Heng J. & Guiochon G. 2011. On the relationship between band broadening and the particle-size distribution of the packing material in liquid chromatography: Theory and practice. *J. Chromatogr. A*, 1218, 8209-8221

Gritti F. & Guiochon G. 2012. Mass transfer kinetics, band broadening and column efficiency. *J. Chromatogr. A*, 122, 2-40

Guignard C., Jouve L., Bogéat-Triboulot M. B., Dreyer E., Hausman J. –F. & Hoffmann L. 2005. Analysis of carbohydrates in plants by high-performance anion-exchange chromatography coupled with electrospray mass spectrometry. *J. Chromatogr. A*, 1085, 137-142

Gundersen J. L. 2001. Separation of isomers of nonylphenol and select nonylphenol polyethoxylates by high-performance liquid chromatography on a graphitic carbon column. *J. Chromatogr. A*, 914, 161-166

Guo Y. & Conrad H. E. 1988. Analysis of oligosaccharides from heparin by reversed-phase ion-pairing high-performance liquid chromatography. *Anal. Biochem.*, 168, 54-62

Haerle R., Riedo E., Pasquarello A. & Baldereschi A. 2001. sp^2/sp^3 hybridization ratio in amorphous carbon from C 1*s* core-level shifts: X-ray photoelectron spectroscopy and first-principles calculation. *Phys. Rev. B*, 65, 045101

Harnisch J. A. & Porter M. D. 2001. Electrochemically modulated liquid chromatography: an electrochemical strategy for manipulating chromatographic retention. *Analyst*, 126, 1841-1849

Harnisch J. A., Gazda D. B., Anderegg J. W. & Porter M. D. 2001. Chemical modification of carbonaceous stationary phases by the reduction of diazonium salts. *Anal. Chem.*, 73, 3954-3959

Harris P. J. F. & Tsang S. C. 1997. High-resolution electron microscopy studies of non-graphitizing carbons. *Phil. Mag. A.*, 76, 667-677

Harris P. J. F., Burian A. & Duber S. 2000. High resolution electron microscopy of a microporous carbon. *Philos. Mag. Lett.*, 80, 381-386

Harris P. J. F. 2005. New perspectives on the structure of graphitic carbons. *Crit. Rev. Solid State*, 30, 235-253

Hemström P. & Irgum K. 2006. Hydrophilic interaction chromatography. *J. Sep. Sci.*, 29, 1784-1821

Henrard L., Stephan O. & Colliex C. 1999. Electron energy loss study of plasmon excitations in curved carbon network. *Synthetic Met*., 103, 2502-2503

Hirano M. & Shinjo K. 1990. Atomistic locking and friction. *Phys Rev. B*, 41, 11837-11851

Hirano S., Inagaki M. & Saito H. 1970. Effect of coexisting minerals on the graphitization of carbon under pressure. V. Distribution of calcium and graphitic components in heat-treated carbon specimens. *Bull. Chem. Soc. Jpn*., 43, 2624-2625

Hirano S., Inagaki M. & Saito H. 1979. Cooperative accelerating effect of calcium carbonate and gaseous nitrogen on graphitization of carbon. *Carbon*, 17, 395-398

Hoekstra F. A., Golovina E. A. & Buitink J. 2001. Mechanisms of plant desiccation tolerance. *Trends Plant Sci.*, 6, 431-438

Horikawa T., Hayashi J. & Muroyama K. 2004. Size control and characterization of spherical carbon aerogel particles from resorcinol–formaldehyde resin. *Carbon*, 42, 169-175

Hsieh C. –T. & Teng H. 2000. Influence of mesopore volume and adsorbate size on adsorption capacities of activated carbons in aqueous solutions. *Carbon*, 38, 863-869

Huang R. Y. M., Pal R. & Moon G. Y. 1999. Characteristics of sodium alginate membranes for the pervaporation dehydration of ethanol-water and isopropanol-water mixtures. *J. Membrane Sci*., 160, 101-113

Ide M., Wallaert E., Van Driessche I., Lynen F., Sandra P. & Van Der Voort P. 2011. Spherical mesoporous silica particles by spray drying: Doubling the retention factor of HPLC columns. *Micropor. Mesopor. Mat*., 142, 282-291

Iijima S. 1991. Helical microtubules of graphitic carbon. *Nature*, 354, 56-58

Ikegami T., Tomomatsu K., Takubo H., Horie K. & Tanaka N. 2008. Separation efficiencies in hydrophilic interaction chromatography. *J. Chromatogr. A*, 1184, 474-503

Inan G., Zhang Q., Li P., Wang Z., Cao Z., Zhang H., Zhang C., Quist T. M., Goodwin S. M., Zhu J., Shi H., Damsz B., Charbaji T., Gong Q., Ma S., Fredricksen M., Galbraith D. W., Jenks M. A., Rhodes D., Hasegawa P. M., Bohnert H. J., Joly R. J., Bressan R. A. & Zhu J. -K. 2004. Salt cress. A halophyte and cryophyte Arabidopsis relative model system and its applicability molecular genetic analyses of growth and development of extremophiles. *Plant Physiol*., 135, 1718-1737

International Rice Genome Sequencing Project. 2005. The map-based sequence of the rice genome. *Nature*, 436, 793-800

Iribarne J. V. & Thomson B. A. 1976. On the evaporation of small ions from charged droplets. *J. Chem. Phys*., 64, 2287-2294

Jensen A. W., Wilson S. R. & Schuster D. I. 1996. Biological applications of fullerenes. *Bioorgan. Med. Chem*., 4, 767-779

Jha A., Banerjee D. & Chattopadhyay K. K. 2011. Improved field emission from amorphous carbon nanotubes by surface functionalization with stearic acid. *Carbon*, 49, 1272-1278

Job N., Théry A., Pirard R., Marien J., Kocon L., Rouzaud J. –N., Béguin F. & Pirard J. –P. 2005. Carbon aerogels, cryogels and xerogels: Influence of the drying method on the textural properties of porous carbon materials. *Carbon*, 43, 2481-2494

Jonscher K. R. & Yates J. R. 1997. The quadrupole ion trap mass spectrometer - a small solution to a big challenge. *Anal. Biochem*., 244, 1-15

Jupp B. P. & Drew E. A. 1974. Studies on the growth of *Laminaria hyperborea* (Gunn.) Fosl. I. Biomass and productivity. *J. Exp. Mar. Biol. Ecol*., 15, 185-196

Kain J. M. 1977. The biology of *Laminaria hyperborea*. X. The effect of depth on some populations. *J. Mar. Biol. Ass. U.K.*, 57, 587-607

Kamo M., Sato Y., Matsumoto S. & Setaka N. 1983. Diamond synthesis from gas phase in microwave plasma. *J. Cryst. Growth*, 62, 642-644

Karamanos N. K., Vanky P., Tzanakakis G. N., Tsegenidis T. & Hjerpe A. 1997. Ion-pair high-performance liquid chromatography for determining disaccharide composition in heparin and heparin sulphate. *J. Chromatogr. A*, 765, 169-179

Kauss H. Thomson K. S., Tetour M. & Jeblick W. 1978. Proteolytic activation of a galactosyl transferase involved in osmotic regulation. *Plant Physiol*., 61, 35-37

Kelly M. S. & Dworjanyn S. 2008. The potential of marine biomass for anaerobic biogas production. *The Crown Estate*

Keun H. C., Ebbels T. M. D., Antti H., Bollard M. E., Beckonert O., Holmes E., Lindon J. C. & Nicholson J. K. 2003. Improved analysis of multivariate data by variable stability scaling: application to NMR-based metabolic profiling. *Anal. Chim. Acta*, 490, 265-276

Kim Y.S., Liu J., Han X. J., Pervin A. & Linhardt R. J. 1995. Analysis of fluorescently labeled sugars by reversed-phase ion-pairing high-performance liquid-chromatography. *J. Chromatogr. Sci*., 33, 162-167

Kind T. & Fiehn O. 2010. Advances in structure elucidation of small molecules using mass spectrometry. *Bioanal. Rev*., 2, 23-60

Kirkland J. J. & DeStefano J. J. 2006. The art and science of forming packed analytical high-performance liquid chromatography columns. *J. Chromatogr. A*, 1126, 50-57

Knox J. H. & Gilbert M. T. 1979. Preparation of porous carbon. *US Patent*, 4263268

Knox J. H., Kaur B. & Millward G.R. 1986. Structure and performance of porous graphitic carbon in liquid chromatography. *J. Chromatogr. A*, 352, 3-25

Knox J. H. & Ross P. 1997. *Advances in Chromatography, Vol. 37*. eds: Brown P. R. & Grushka E., Marcel Dekker, New York, USA, 73-119

Koizumi, K. 1996. High-performance liquid chromatographic separation of carbohydrates on graphitized carbon columns. *J. Chromatogr. A,* 720, 119-126

Krasensky J., and Jonak C. 2012. Drought, salt, and temperature stress-induced metabolic rearrangements and regulatory networks. *J. Exp. Bot*., 63, 1593-1608

Kříž J., Adamcová E., Knox J. H. & Hora J. 1994. Characterization of adsorbents by high-performance liquid chromatography using aromatic hydrocarbons. Porous graphite and its comparison with silica gel, alumina, octadecylsilica and phenylsilica. *J. Chromatogr. A*., 663, 151-161

Kroto H. W., Heath J. R., O'Brien S. C., Curl R. F. & Smalley R. E. 1985. C_{60}: Buckminsterfullerene. *Nature*, 318, 162-163

Kyotani T. 2000. Control of pore structure in carbon. *Carbon*, 38, 269-286

Lee J., Yoon S., Oh S. M., Shin C. -H. & Hyeon T. 2000. Development of a new mesoporous carbon using an HMS aluminosilicate template. *Adv. Mater*., 12, 359-362

Lee W. S. & Yu J. 2005. Comparative study of thermally conductive fillers in underfill for the electronic components. *Diam. Relat. Mater*., 14, 1647-1653

Lee Y. P., Babakov A., de Boer B., Zuther E. & Hincha D. K. 2012. Comparison of freezing tolerance, compatible solutes and polyamines in geographically diverse collections of *Thellungiella sp*. and *Arabidopsis thaliana* accessions. *BMC Plant Biol*., 12, 131

Li Z. & Dai S. 2005. Surface functionalization and pore size manipulation for carbons of ordered structure. *Chem. Mater*., 17, 1717-1721

Liang C., Hong K., Guiochon G. A., Mays J. W. & Dai S. 2004. Synthesis of a large-scale highly ordered porous carbon film by self-assembly of block copolymers. *Angew. Chem. Int. Ed*., 43, 5785-5789

Liang C., Li Z. & Dai S. 2008. Mesoporous carbon materials: Synthesis and modification. *Angew. Chem. Int. Ed*., 47, 3696-3717

Lind A., von Hohenesche C. D., Smått J. -H., Lindén M. & Unger K. K. 2003. Spherical silica agglomerates possessing hierarchical porosity prepared by spray drying of MCM-41 and MCM-48 nanospheres. *Micropor. Mesopor. Mat*., 66, 219-227

Liu B., Jia D., Zhou Y., Feng H. & Meng Q. 2007. Low temperature synthesis of amorphous carbon nanotubes in air. *Carbon*, 45, 1696-1716

Liu Z. M., Becker T. & Neufeld R. J. 2005. Spherical alginate granules formulated for quick-release active subtilisin. *Biotechnol. Prog*., 21, 568-574

Lottes F., Arlt W., Minceva M. & Stenby E. H. 2009. Hydrodynamic impact of particle shape in slurry packed liquid chromatography columns. *J. Chromatogr. A*, 1216, 5687-5695

Lowell S. & Shields J. E. 1991. *Powder surface area and porosity*. Chapman and Hall, London, UK, 200-230

Lu A. -H., Li W. -C., Schmidt W. & Schüth F. 2005. Template synthesis of large pore ordered mesoporous carbon. *Micropor. Mesopor. Mat*., 80, 117-128

Lugan R., Niogret M. –F., Leport L., Gue´gan J. –P., Larher F. R., Savouré A., Kopka J. and Bouchereau A. 2010. Metabolome and water homeostasis analysis of

Thellungiella salsuginea suggests that dehydration tolerance is a key response to osmotic stress in this halophyte. *Plant J.*, 64, 215-229

Luque R., Budarin V., Clark J. H., Shuttleworth P. & White R. J. 2011. Starbon® acids in alkylation and acetylation reactions: Effect of the Brönsted-Lewis acidity. *Catal. Commun.*, 12, 1471-1476

Mackenzie K., Battke J. & Kopinke F. -D. 2005. Catalytic effects of activated carbon on hydrolysis reactions of chlorinated organic compounds. Part 1. γ-Hexachlorocyclohexane. *Catal. Today*, 102-103, 148-153

Maier T., Güell M. & Serrano L. 2009. Correlation of mRNA and protein in complex biological samples. *FEBS Lett.*, 583, 3966-3973

March R. E. 1997. An introduction to quadrupole ion trap mass spectrometry. *J. Mass Spectrom.*, 32, 351-369

March R. E. 2000. *Quadrupole ion trap mass spectrometer* in *Encyclopedia of analytical chemistry*. ed R. A. Meyers, J. Wiley & Sons Ltd., Chichester, UK, 7-11

Maslen E. N., Streltsov V. A. & Streltsova N. R. 1993. X-ray study of the electron density in calcite, $CaCO_3$. *Acta Crystallogr. B*, 49, 636-641

Matsumoto S., Sato Y., Tsutsumi M. & Setaka N. 1982. Growth of diamond particles from methane-hydrogen gas. *J. Mater. Sci.*, 17, 3106-3112

Mauko L., Lacher N. A., Pelzing M., Nordbog A., Haddad P. R. & Hilder E. F. 2012. Comparison of ZIC-HILIC and graphitized carbon-based analytical approaches combined with exoglycosidase digestions for analysis of glycans from monoclonal antibodies. *J. Chromatogr. B*, 911, 93-104

May P. W. 2000. Diamond thin films: a 21st-century material. *Phil. Trans. R. Soc. Lond. A*, 358, 473-495

McBain J. W. 1935. An explanation of hysteresis in the hydration and dehydration of gels. *J. Am. Chem. Soc*., 57, 699-700

McEnaney B. 1988. Adsorption and structure in microporous carbons. *Carbon*, 26, 267-274

Meinke D. W., Cherry J. M., Dean C., Rounsley S. D. & Koornneef M. 1998. *Arabidopsis thaliana*: A model plant for genome analysis. *Science*, 282, 662-682

Meng Y., Gu D., Zhang F., Shi Y., Cheng L., Feng D., Wu Z., Chen Z., Wan Y., Stein A. & Zhao D. 2006. A family of highly ordered mesoporous polymer resin and carbon structures from organic-organic self-assembly. *Chem. Mater*., 18, 4447-4464

METLIN Metabolite Database, Version 1.1. Scripps Centre for Metabolomics, 2010. c2010 [updated 10th September 2012, cited March 2013]. Available from: http://metlin.scripps.edu/

Michopoulos F., Lai L., Gika H., Theodoridis G. & Wilson I. 2009. UPLC-MS-based analysis of human plasma for metabonomics using solvent precipitation or solid phase extraction. *J. Prot. Res*., 8, 2114-2121

Moreno A. H., Arenillas A., Calvo E. G., Bermúdez J. M. & Menéndez J. A. 2013. Carbonisation of resorcinol–formaldehyde organic xerogels: Effect of temperature, particle size and heating rate on the porosity of carbon xerogels. *J. Anal. Appl. Pyrol.*, 100, 111-116

Morris E. R., Rees D. A. & Thom D. 1978. Chiroptical and stoichiometric evidence of a specific primary dimerisation process in alginate gelation. *Carbohyd. Res*., 66, 145-154

Müller J., Sprenger N., Bortlik K., Boller T. & Wiemken A. 1997. Desiccation increases sucrose levels in *Ramonda* and *Haberlea*, two genera of resurrection plants in the Gesneriaceae. *Physiol. Plantarum*, 100, 153-158

Nishizawa A., Yabuta Y. & Shigeoka S. 2008. Galactinol and raffinose constitute a novel function to protect plants from oxidative damage. *Plant Physiol*., 147, 1251-1263

NIST X-ray Photoelectron Spectroscopy Database, Version 4.1. Gaithersburg, 2012: National Institute of Standards and Technology. c2000 [updated 15th September 2012, cited June 2013]. Available from: http://srdata.nist.gov/xps/

Noda T., Inagaki M., Hirano S. & Saito H. 1969. Effect of coexisting minerals on graphitization of carbon under pressure. III. Accelerating effect of calcium hydroxide. *Bull. Chem. Soc. Jpn.*, 42, 1738-1740

Novoselov K. S., Geim A. K., Morozov S. V., Jiang D., Zhang Y., Dubonos S. V., Grigorieva I. V. & Firsov A. A. 2004. Electric field effect in atomically thin carbon films. *Science*, 306, 666-669

Õya A. & Õtani S. 1977. Effects of particle size of calcium and calcium compounds on catalytic graphitization of phenolic resin carbon. *Carbon*, 17, 125-129

Pang Q., Chen S., Dai S., Chen Y., Wang Y. & Yan X. 2010. Comparative proteomics of salt tolerance in Arabidopsis thaliana and Thellungiella halophila. *J. Proteome Res*., 9, 2584-2599

Papageorgiou S. K., Kouvelos E. P., Favvas E. P., Sapalidis A. A., Romanos G. E. & Katsaros F. K. 2010. Metal-carboxylate interactions in metal-alginate complexes studied with FT-IR spectroscopy. *Carbohyd. Res*., 345, 469-473

Papworth A. J., Kiely C. J., Burden A. P., Silva S. R. P. & Amaratunga G. A. J. 2000. Electron-energy-loss spectroscopy characterization of the sp^2 bonding fraction within carbon thin films. *Phys. Rev. B*, 62, 12628-12631

Parker H. L., Hunt A. J., Budarin V. L., Shuttleworth P. S., Miller K. L. & Clark J. H. 2012. The importance of being porous: polysaccharide-derived mesoporous materials for use in dye adsorption. *RSC Advances*, 2, 8992-8997

Parker H. L., Hunt A. J., Budarin V. L., Shuttleworth P. S., Miller K. L. & Clark J. H. 2012. The importance of being porous: polysaccharide-derived mesoporous materials for use in dye adsorption. *RSC Advances*, 2, 8992-8997

Patti G. J. 2011. Separation strategies for untargeted metabolomics. *J. Sep. Sci.*, 34, 3460-3469

Paul W. & Steinwedel H. 1953. Ein neues massenspektrometer ohne magnetfeld. *Z. Naturfors. Sect. A-J. Phys. Sci.*, 8, 448-450
Perlin A. S. 1952. Thermal decarboxylation of uronic acids. *Can. J. Chem.*, 30, 278-290

Peters S., Mundree S. G., Thomson J. A., Farrant J. M. and Keller F. 2007. Protection mechanisms in the resurrection plant *Xerophyta viscosa* (Baker): both sucrose and raffinose family oligosaccharides (RFOs) accumulate in leaves in response to water deficit. *J. Exp. Bot.*, 58, 1947-1956

Pichon V., Chen L., Guenu S. & Hennion M. -C. 1995. Comparison of sorbents for the solid-phase extraction of the highly polar degradation products of atrazine (including ammeline, ammelide and cyanuric acid). *J. Chromatogr. A*, 711, 257-267

Pinheiro C., António C., Ortuño M. F., Dobrev P. I., Hartung W., Thomas-Oates J., Pinto Ricardo C., Vanková R., Chaves M. M. & Wilson J. C. 2011. Initial water deficit effects on *Lupinus albus* photosynthetic performance, carbon metabolism, and hormonal imbalance: metabolic reorganization prior to early stress responses. *J. Exp. Bot.*, 62, 4965-4974

Powles R. C., Marks N. A. & Lau D. W. M. 2009. Self-assembly of sp^2-bonded carbon nanostructures from amorphous precursors. *Phys. Rev. B*, 79, 075430

Prato M. 1997. [60] Fullerene chemistry for materials science applications. *J. Mater. Chem.*, 7, 1097-1109

PRIMe Database, Version 1.1. RIKEN PSC, 2011: RIKEN Plant Science Center. c2011 [updated 10th August 2012, cited March 2013]. Available from: http://prime.psc.riken.jp/lcms/AtMetExpress/

Quignard F., Valentin R. & Di Renzo F. 2008. Aerogel materials from marine polysaccharides. *New J. Chem.*, 32, 1300-1310

Rigby S. P. & Fletcher R. S. 2004. Experimental evidence for pore blocking as the mechanism for nitrogen sorption hysteresis in a mesoporous material. *J. Phys. Chem. B*, 108, 4690-4695

Robertson J. 1991. Hard amorphous (diamond-like) carbons. *Prog. Solid St. Chem.*, 21, 199-333

Robinson S., Bergström E., Seymour M. & Thomas-Oates J. 2007. Screening of underivatized oligosaccharides extracted from the stems of *Triticum aestivum* using porous graphitized carbon liquid chromatography-mass spectrometry. *Anal. Chem.*, 79, 2437-2445

Robitzer M., David L., Rochas C., Di Renzo F. & Quignard F. 2008. Supercritically-dried alginate aerogels retain the fibrillar structure of the hydrogels. *Macromol. Symp.*, 273, 80-84

Robitzer M., Tourrette A., Horga R., Valentin R., Boissière M., Devoisselle J. M., Di Renzo F. & Quignard F. 2011a. Nitrogen sorption as a tool for the characterisation of polysaccharide aerogels. *Carbohyd. Polym.*, 85, 44-53

Robitzer M., Di Renzo F. & Quignard F. 2011b. Natural materials with high surface area. Physisorption methods for the characterization of the texture and surface of polysaccharide aerogels. *Micropor. Mesopor. Mat.*, 140, 9-16

Rosén J & Hellenäs K. -E. 2002. Analysis of acrylamide in cooked foods by liquid chromatography tandem mass spectrometry. *Analyst*, 127, 880-882

Ross A. B., Hall C., Anastasakis A., Westwood A., Jones J. M. & Crewe R. J. 2011. Influence of cation on the pyrolysis and oxidation of alginates. *J. Anal. Appl. Pyrol*., 91, 344-351

Rouquérol J., Avnir D., Fairbridge C. W., Everett D. H., Haynes J. H., Pernicone N., Ramsay J. D. F., Sing K. S. W. & Unger K. K. 1994. Recommendations for the characterization of porous solids. *Pure and Appl. Chem*., 66, 1739-1758

Ryoo R., Joo S. H. & Jun S. 1999. Synthesis of highly ordered carbon molecular sieves via template-mediated structural transformation. *J. Phys. Chem. B*, 103, 7743-7746

Ryoo R., Joo S. H., Kruk M. & Jaroniec M. 2001. Ordered mesoporous carbons. *Adv. Mater*., 13, 677-681

Saito Y., Matsuda S. & Nogita S. 1986. Synthesis of diamond by decomposition of methane in microwave plasma. *J. Mater. Sci. Lett*., 5, 565-568

Scharrenberger C. 1990. Characterization and compartmentation, in green leaves, of hexokinases with different specificities for glucose, fructose, and mannose and for nucleoside triphosphates. *Planta*, 181, 249-255

Schiller M., von der Heydt H., März F.& Schmidt P. C. 2002. Quantification of sugars and organic acids in hygroscopic pharmaceutical herbal dry extracts. *J. Chromatogr. A*, 2002, 968, 101-111

Schumacher D. & Kroh L. W. 1995. A rapid method for separation of anomeric saccharides using a cyclodextrin bonded phase and for investigation of mutarotation. *Food Chem*., 54, 353-356

Seki M., Kamei A., Yamaguchi-Shinozaki K.& Shinozaki K. 2003. Regulatory metabolic networks in drought stress responses. *Curr. Opin. Biotech.*, 2003, 14, 194-199

Sing K. S. W., Everett D. H., Haul R. A. W., Moscou L., Pierotti R. A., Rouquérol J. & Siemieniewka T. 1985. Reporting physisorption data for gas/solid systems. *Pure & Appl. Chem.*, 57, 603-619

Sircar S., Golden T. C. & Rao M. B. 1996. Activated carbon for gas separation and storage. *Carbon*, 34, 1-12

Soares J. P., Santos J. E., Chierice G. O. & Cavalheiro E. T. G. 2004. Thermal behaviour of alginic acid and its sodium salt. *Ecl. Quim., São Paulo*, 29, 53-56
Stafford G. C., Kelley P. E., Syka J. E. P., Reynolds W. E. & Todd J. F. J. 1984. Recent improvements in and analytical applications of advanced ion trap technology. *Int. J. Mass Spectrom.*, 60, 85-98

Stefanov K., Markovska Y., Kimenov G. & Popov S. 1992. Lipid and sterol changes in leaves of *Haberlea rhodopensis* and *Ramonda serbica* at transition from biosis into anabiosis and vice versa caused by water stress. *Phytochemistry*, 31, 2309-2314

Steiner A. B. & McNeely W. H. 1950. High-stability glycol alginates and their manufacture. *US Patent*, 2494911

Stöber W., Fink A. & Bohn E. 1968. Controlled growth of monodisperse silica spheres in the micron size range. *J. Colloid Interf. Sci.*, 26, 62-69

Stroop C. J. M., Bush C. A., Marple R. L. & LaCourse W. R. 2002. Carbohydrate analysis of bacterial polysaccharides by high-pH anion-exchange chromatography and online polarimetric determination of absolute configuration. *Anal. Biochem.*, 303, 176-185

Suganuma S., Nakajima K., Kitano M., Kato H., Tamura A., Kondo H., Yanagawa S., Hayashi S. & Hara M. 2011. SO_3H-bearing mesoporous carbon with highly selective catalysis. *Micropor. Mesopor. Mat.*, 143, 443-450

Tamon H., Ishizaka H., Yamamoto T. & Suzuki T. 2000. Influence of freeze-drying conditions on the mesoporosity of organic gels as carbon precursors. *Carbon*, 38, 1099-1105

Te Wierik G. H. P., Bergsma J., Arends-Scholte A. W., Boersma T., Eissens A. C. & Lerk C. F. 1996. A new generation of starch products as excipient in pharmaceutical tablets. I. Preparation and binding properties of high surface area potato starch products. *Int. J. Pharm.*, 134, 27-36

The Arabidopsis Genome Initiative. 2000. Analysis of the genome sequence of the flowering plant *Arabidopsis thaliana*. *Nature*, 408, 796-815

The Tomato Genome Consortium. 2012. The tomato genome sequence provides insights into fleshy fruit evolution. *Nature*, 485, 635-641

Thomson W. 1871. LX. On the equilibrium of vapour at a curved surface of liquid. *Philos. Mag. Series 4*, 42, 448-452

Tolstikov V. V. & Fiehn O. 2002. Analysis of highly polar compounds of plant origin: Combination of hydrophilic interaction chromatography and electrospray ion trap mass spectrometry. *Anal. Biochem.*, 301, 298-307

Tønnesen H. H. & Karlsen J. 2002. Alginate in drug delivery solutions. *Drug Dev. Ind. Pharm.*, 28, 621-630

Tsapis N., Bennett D., Jackson B., Weitz D. A. & Edwards D. A. 2002. Trojan particles: Large porous carriers of nanoparticles for drug delivery. *PNAS*, 99, 12001-12005

Tseng C. K. 2001. Algal biotechnology industries and research activities in China. *J. Appl. Phycol.*, 13, 375-380

Tsubouchi N., Xu C. & Ohtsuka Y. 2003. Carbon crystallization during high-temperature pyrolysis of coals and the enhancement by calcium. *Energ. Fuel.*, 17, 1119-1125

Unger K. K., Skudas R. & Schulte M. M. 2008. Particle packed columns and monolithic columns in high-performance liquid chromatography-comparison and critical appraisal. *J. Chromatogr. A*, 1184, 393-415

Urano K., Maruyama K., Ogata Y., Morishita Y., Takeda M., Sakurai N., Suzuki H., Saito K., Shibata D., Kobayashi M., Yamaguchi-Shinozaki K. and Shinozaki K. 2009. Characterization of the ABA-regulated global responses to dehydration in Arabidopsis by metabolomics. *Plant J.*, 57, 1065-1078

van Deemter J. J., Zuiderweg F. J. & Klinkenberg A. 1956. Longitudinal diffusion and resistance to mass transfer as causes of nonideality in chromatography. *Chem. Engng. Sci.*, 5, 271-289

Vehring R., Foss W. R. & Lechuga-Ballesteros D. 2007. Particle formation in spray drying. *Aerosol Sci.*, 38, 728-746

Verzele M., Dewaele C. & Duquet D. 1987. Observations and ideas on slurry packing of liquid chromatography columns. *J. Chromatogr.*, 391, 111-118

Viant M. R. & Sommer U. 2013. Mass spectrometry based environmental metabolomics: a primer and review. *Metabolomics*, 9, S144-S158

Vogel C. & Marcotte E. M. 2012. Insights into the regulation of protein abundance from proteomic and transcriptomic analyses. *Nat. Rev. Genet.*, 13, 227-232

Wan Q. -H., Nicholas Shaw P., Davies M. C. & Barrett D. A. 1997. Role of alkyl and aryl substituents in chiral ligand exchange chromatography of amino acids. Study using porous graphitic carbon coated with N-substituted-L-proline selectors. *J. Chromatogr. A*, 786, 249-257

Warren B. E. 1941. X-ray diffraction in random layer lattices. Phys. Rev., 59, 693-698

White R. J. 2008. 'Porous polysaccharide derived materials'. PhD thesis, University of York, York, UK

White R. J., Budarin V. L. & Clark J. H. 2008. Tuneable mesoporous materials from α-D-polysaccharides. *ChemSusChem*, 1, 408-411

White R. J., Budarin V. L. & Clark J. H. 2009. Pectin-derived porous materials. *Chem. Eur. J.*, 16, 1326-1335

White R. J., Antonio C., Budarin V. L., Bergström E., Thomas-Oates J. & Clark J. H. 2010. Polysaccharide-derived carbons for polar analyte separations. *Adv. Funct. Mater*., 20, 1834-1841

Whittaker A., Martinelli T., Farrant J. M., Bochicchio A. and Vazzana C. 2007. Sucrose phosphate synthase activity and the co-ordination of carbon partitioning during sucrose and amino acid accumulation in desiccation-tolerant leaf material of the C_4 resurrection plant *Sporobolus stapfianus* during dehydration. *J. Exp. Bot.*, 58, 3775-3787

Winograd N. & Gaarenstroom S. W. 1980. in *Physical Methods in Modern Chemical Analysis, Vol. 2*. ed: T. Kuwana, Academic Press, New York, USA, Ch. 2, 115-169

Wohlgemuth S. -A., Vilela F., Titirici M. -M. & Antonietti M. 2012. A one-pot hydrothermal synthesis of tunable dual heteroatom-doped carbon microspheres. *Green Chem*., 14, 741-749

Yamashita M. & Fenn J. B. 1984. Electrospray ion source. Another variation on the free-jet theme. *J. Phys. Chem*., 88, 4451-4459

Yang Z. & Mokoya R. 2008. Probing the effect of the carbonisation process on the textural properties and morphology of mesoporous carbons. *Micropor. Mesopor. Mat.*, 113, 378-384

Yaroshevsky A.A. 2006. Abundances of chemical elements in the Earth's crust. *Geochem. Int+*, 44, 48-55

Zhang S. Q., Wang J., Shen J., Deng Z. S., Lai Z. Q., Zhou B., Attia S. M. & Chen L. Y. 1999. The investigation of the adsorption character of carbon aerogels. *Nanostruct. Mater.*, 11, 375-381

Zhang Z., Brydson R., Aslam Z., Reddy S., Brown A., Westwood A. & Rand B. 2011. Investigating the structure of non-graphitising carbons using electron energy loss spectroscopy in the transmission electron microscope. *Carbon*, 49, 5049-5063.

Zhao D., Huo Q., Feng J., Chmelka B. F. & Stucky G. D. 1998. Nonionic triblock and star diblock copolymer and oligomeric surfactant syntheses of highly ordered, hydrothermally stable, mesoporous silica structures. *J. Am. Chem. Soc*., 120, 6024-6036

Zheng L., Zhou Q., Deng X., Sun D., Yuan M., Yu G. & Cao Y. 2003. Synthesis of C60 derivatives for polymer photovoltaic cell. *Synthetic Met*., 135-136, 827-828

Zhu J. -K. 2001. Plant salt tolerance. *Trends Plant Sci*., 6, 61-71